Measurement Of Event Shape Variables In Deep Inelastic Scattering

Robert George Waugh

Department of Physics & Astronomy
University of Glasgow
Glasgow

Thesis submitted for the degree of
Doctor of Philosophy

January 1999

Preface

The theory of Quantum ChromoDynamics (QCD) has been developed to calculate the strong interactions of coloured objects, such as quarks and gluons, at short distances. The force mediator for the strong interaction, one of the 4 fundamental forces, is the gluon itself. The resulting non-Abelian nature of the theory increases its complexity in comparison to the well tested theory of Quantum Electrodynamics (QED), where the force mediator is the uncharged photon. One of the open questions in modern high energy physics concerns the transition of parton dynamics at short distances, or hard scales, to the long distance, or soft scale, hadron dynamics. The theory of QCD deals with the interactions of partons but cannot be extended to the soft limit where the strong coupling constant, α_s, becomes large and perturbative expansion is no longer possible. Presently, the gap between the partonic and hadronic world is bridged by phenomenological models motivated by experimental observation and theoretical considerations. A new model based on infra-red safe factorially divergent event shape variables may link the two worlds and develop our understanding of the transition region.

Historically event shape variables have been studied, along with jet rates, in $e^+e^- \rightarrow q\bar{q}$ events to extract a value for the strong coupling constant α_s. Only recently, with the large amount of data being collected by electron proton colliding experiments, have these studies been possible using deep inelastic scattering data. These studies have previously used Monte Carlo (MC) event generators to correct the observed data back to parton level distributions. From these parton level distributions a value of α_s can be extracted. This has lead to measurements being dependent on the event generator used and thus large systematic uncertainties dominate.

The lack of a firm understanding of the parton to hadron transition has been a clear handicap in the study of event shape variables. Recent theoretical work has approached this problem with the use of an effective strong coupling, α_{eff}, interceding at small scales, usually around 2 GeV. This approach results in the mean event shape variables being described by the sum of a next to leading contribution and a (relatively) simple power correction contribution of the form $1/Q$. This phenomenological concept of a power correction introduces a variable to be measured from experiment, this variable is $\overline{\alpha_0}$.

The measurement of the event shape variables thrust, T_z, jet broadening, B_c, invariant jet mass, ρ_E, and C parameter, C_E, are presented over the kinematic range of $0.0006 \leq x \leq 0.8$ and $3.75 \leq \langle Q \rangle \leq 144$ GeV^2. Both differential and mean distributions are shown for each variable with power corrected next to leading order predictions fitted to the mean values to determine a value for α_s and a new phenomenological parameter $\overline{\alpha_0}$.

Acknowledgements

I would firstly like to thank my parents and family for all the moral and financial support they have given me during my whole time at university, I now promise to get a “proper” job.

I thank my supervisor, Tony Doyle, who has been a constant source of help and motivation, thanks to him I now understand far more about physics than I ever thought I would. In the end pushing me to finish my thesis quickly was the right thing to do, take note future students!

I would like to thank David Saxon for offering me a position as a post-graduate student in the ZEUS group and PPARC for funding me most generously throughout my three years. The members of the ZEUS collaboration have been of great help and I will count my time in Hamburg as one of the happiest of my life. I would like to specifically mention Nick Brook, Laurel Sinclair and Jane Bromley who all helped me in more ways than I can remember.

The Bleicherstrasse Theatrical Workshop (members past and present) deserve a big thank you; without the escape of the two plays I doubt my sanity would have held. The time spent rehearsing or just plain lazing around taught me that there is little more to happiness other than a few good friends.

Others I wish to thank are too many to mention, but I’ll have a go. Thanks to Matt, Graham, Martin, Shane and Michael for being friends longer

than I can remember; Paul, Asia and William for showing me how happy families live; Sarah for being there (unfortunately I was here); Eram and Andy who are always interested in a frolic at the weekend; Neil, Gavin and Sung Won for carrying on the great traditions of Glasgow students; Paul and Anna for rescuing the Bleicherstrasse theatre, go Dutch on the repairs; the ZEUS UK corridor for showing me that I really wasn't that terrible a drunk (relatively); and to Susan Ketels for being the most helpful person in the world.

A little bit of truth makes the lie a whole lot more believable.

Contents

Preface i

Acknowledgements iii

1 The HERA machine and ZEUS detector **1**

1.1 The HERA Machine 1

1.2 The ZEUS Detector 6

1.3 Inner Tracking Detector 10

1.3.1 The Central Tracking Detector 11

1.3.2 The Forward And Rear Tracking Detector 16

1.3.3 The Small Angle Rear Tracking Detector 17

1.4 Calorimetry at ZEUS 17

1.4.1 The Depleted Uranium Calorimeter 18

1.4.2 The Hadron Electron Separator 21

1.4.3 The Backing Calorimeter 21

1.5 The Muon Detectors 22

1.6 The Luminosity Monitors 22

1.7 The ZEUS Trigger 23

1.7.1 Track Reconstruction 24

2 Theory **25**

2.1 Kinematics Of Deep Inelastic Scattering 26

2.2 Cross Sections And The Parton Model 30

2.3 QCD Improved Parton Model 32

2.4 The Strong Coupling Constant (α_s) 34

2.5 Next to Leading Order Monte Carlos 36

2.6 The Breit Frame 37

2.7 Event Shape Variables 41

2.8 Power Corrections 45

2.8.1 Milan Factor 46

3 Data Analysis **49**

3.1 Kinematic Reconstruction 49

3.1.1 The Electron Method 50

3.1.2 The Jacquet-Blondel Method 51

3.1.3 The Double Angle Method 51

3.2 Electron Finding 52

3.3 Data Analysis 53

3.3.1 Data Selection 53

3.3.2 Track Selection 56

3.4 Boosting To The Breit Frame 58

3.5 Current Region Energy Cut 59

4 Monte Carlo Simulation **63**

4.1 Introduction 63

4.2 The ARIADNE Event Generator 65

4.2.1 The JETSET Event Generator 71

4.3 The HERWIG Event Generator 71

4.4 The ZEUS Detector Simulation 72
4.5 Tuning An Event Generator 73
    4.5.1 Sensitivity Plots 75
    4.5.2 Results Of Tuning ARIADNE 76

5 Monte Carlo Studies **83**
5.1 Reproduction of Kinematics 84
5.2 Resolution Of Observables 86
5.3 Efficiencies And Purities Of Event Shape Variables 92
5.4 Correction Factors 101
5.5 Monte Carlo Description of Thrust 101

6 NLO Event Shapes **109**
6.1 Input variables for DISENT 110
6.2 NLO Energy Cut 110
6.3 Mean And Differential NLO Distributions 111
6.4 NLO Mean Event Shape Fits 113

7 Results **121**
7.1 Differential and Mean Distributions 121
7.2 Systematic Studies Of Data Analysis 122
    7.2.1 Event Reconstruction and Selection Systematics 128
    7.2.2 Data Correction Systematics 129
    7.2.3 Track Reconstruction And Selection Systematics 130
7.3 Systematic Distributions 131
7.4 Combined Results 137

8 Power Correction fits **139**
8.1 Power Fit Results 139

9 Conclusion And Further Work 149

List of Figures

1.1 HERA injection system. 3

1.2 Delivered luminosity from the HERA machine for each year. . 5

1.3 The $(r - z)$ cross section of the ZEUS Detector. 8

1.4 The $(r - \phi)$ cross section of the ZEUS Detector. 9

1.5 Wire layout in a single octant of the Central Tracking Detector. Alternating layers of sense and field wires are indicated by the dots. The larger dots are the sense wires. 12

1.6 (a) The Local Run Control main window, (b) The Local Run Control expert panel. 15

1.7 A single module of the Forward Calorimeter. 20

2.1 Schematic representation of (a) Neutral Current and (b) Charged Current Deep Inelastic Scattering of an electron off a proton, forming a hadronic final state X. 27

2.2 The kinematic phase space covered by the ZEUS and H1 experiments with previous fixed target experiments shown for comparison. 29

2.3 The Feynman diagram representation of deep inelastic scattering in the Quark Parton Model. 31

2.4 Recent results for the structure function $F_2(x, Q^2)$ as a function of Q^2 in bins of x from ZEUS 1994 and 1995 data sets. . . 33

2.5 Feynman diagrams representing additional deep inelastic scattering processes for the improved Quark Parton Model. The diagram on the left is a final state QCD Compton event and the diagram on the right is a BGF event. 35

2.6 Naïve quark parton model of a DIS event in the laboratory and Breit frame. 38

2.7 A comparison between $e^+e^- \rightarrow q\bar{q}$ events the current region of the Breit frame for DIS events. 40

2.8 Feynman diagrams of leading order DIS processes in the Breit frame. (a) final state QCDC, (b) initial state QCDC with soft gluon emission, (c) initial state QCDC with collinear gluon emission, and (d) BGF process. 42

2.9 Diagrammatical representation of the event shape variables T_z, B_c, ρ_E and C_E for various two particle (shown as a dashed line) configurations. 44

3.1 Ratio of reconstructed mean thrust ($\langle T_z \rangle$) for a specific energy cut divided by the mean thrust for no energy cut as a function of the percentage energy cut. 61

4.1 Representation of the three phases of Monte Carlo deep inelastic scattering simulation. 65

4.2 Feynman diagrams for $qq \longrightarrow qqg$ 67

4.3 Feynman diagrams for $qg \longrightarrow qgg$ 67

4.4 Feynman diagrams for $gg \longrightarrow ggg$ 67

4.5 Available phase space for gluon emission from the CDM . . . 69

4.6 Phase space suppression from proton remnant in the CDM . . 70

4.7 Sensitivity plot for an Energy Energy Correlation at low x. . . 76

4.8 Variation of $f\left(\chi^2\right)$ as a function of the tuned parameters PARA(10), PARA(15) and PARA(27). 79

4.9 Data (points), default MC (line) and tuned MC (dashed) plots of $\ln\left(1/x_p\right)$ for bins 2 (a) and 3 (b), E_T as a function of η (c) and the Seagull plot (d). 80

5.1 Q^2_{DA} distributions for 1995 data (as points), ARIADNE (solid line) and HERWIG (dashed line) using 1995 detector simulation. Part (a) is low and part (b) high Q^2 sample. 84

5.2 x_{DA} distributions for 1995 data (as points), ARIADNE (solid line) and HERWIG (dashed line) using 1995 detector simulation. Part (a) is low and part (b) high Q^2 sample. 85

5.3 Q^2_{DA} (a) and x_{DA} (b) distribution for reconstructed 1996 and 1997 data (as points), ARIADNE (solid line) and HERWIG (dashed line) using 1996 detector simulation. 86

5.4 Distribution of $(Q^2_{DA} - Q^2_{\mathrm{true}})/Q^2_{DA}$ with the RMS value of the distribution shown for each (x, Q^2) interval. The Monte Carlo generator used was ARIADNE with the 1995 detector simulation. 88

5.5 Distribution of $(Q^2_{DA} - Q^2_{\mathrm{true}})/Q^2_{DA}$ with the RMS value of the distribution shown for each (x, Q^2) interval. The Monte Carlo generator used was ARIADNE with the 1995 detector simulation. 89

5.6 Distribution of $(x_{DA} - x_{\mathrm{true}})/x_{DA}$ with the RMS value of the distribution shown for each (x, Q^2) interval. The Monte Carlo generator used was ARIADNE with the 1995 detector simulation. 90

5.7 Distribution of $(x_{DA} - x_{\text{true}})/x_{DA}$ with the RMS value of the distribution shown for each (x, Q^2) interval. The Monte Carlo generator used was ARIADNE with the 1996 detector simulation. 91

5.8 Distribution of $(T_z(\text{rec}) - T_z(\text{true})/T_z(\text{rec})$ with the RMS value of the distribution shown for each (x, Q^2) interval. The Monte Carlo generator used was ARIADNE with the 1995 detector simulation. 94

5.9 Distribution of $(T_z(\text{rec}) - T_z(\text{true})/T_z(\text{rec})$ with the RMS value of the distribution shown for each (x, Q^2) interval. The Monte Carlo generator used was ARIADNE with the 1996 detector simulation. 95

5.10 Efficiency of thrust distribution. The Monte Carlo generator used was ARIADNE with the 1995 detector simulation. 97

5.11 Efficiency of thrust distribution. The Monte Carlo generator used was ARIADNE with the 1996 and 1997 detector simulation. 98

5.12 Purity of thrust distribution. The Monte Carlo generator used was ARIADNE with the 1995 detector simulation. 99

5.13 Purity of thrust distribution. The Monte Carlo generator used was ARIADNE with the 1996 1997 detector simulation. 100

5.14 Correction factors for thrust shown with the RMS value of the distribution. The Monte Carlo generator used was ARIADNE with the 1995 detector simulation. 102

5.15 Correction Factors for thrust shown with the RMS value of the distribution. The Monte Carlo generator used was ARIADNE with the 1996 and 1997 detector simulation. 103

5.16 Reconstructed differential distribution of thrust for 1995 data (points) and the Monte Carlo event generator ARIADNE (solid line) and HERWIG (dashed line) using the 1995 detector simulation. 104

5.17 Reconstructed differential distribution of thrust for combined 1996 and 1997 data (points) and the Monte Carlo event generators ARIADNE (solid line) and HERWIG (dashed line) using the 1996 detector simulation. 105

5.18 Reconstructed mean event shapes for 1995 data and the Monte Carlo event generator ARIADNE and HERWIG using the 1995 detector simulation. 106

5.19 Reconstructed mean event shape as a function of mean Q for combined 1996 and 1997 data and the Monte Carlo event generator ARIADNE and HERWIG using the 1996 detector simulation. 107

6.1 NLO prediction for mean thrust ($\langle T_z \rangle$) for kinematic bin 1 as a function of the energy requirement cut. 112

6.2 Next-to-leading order differential distribution of thrust (T_z) using the CTEQ 4 A3 PDF set ($\Lambda_{QCD}^{[4]} = 296$ MeV). 114

6.3 Next-to-leading order mean thrust (T_z) as a function of mean Q using the CTEQ 4 A3 PDF set ($\Lambda_{QCD}^{[4]} = 296$ MeV). 115

6.4 Linear fit to $\langle 1 - T_z \rangle$ and $\langle \rho_E \rangle$ in bin 7, from the DISENT NLO Monte Carlo generator, for 5 different parton density function with differing $\Lambda_{QCD}^{[4]}$. 116

7.1 Corrected thrust distribution for 1995 data. 123

7.2 Corrected thrust distribution for combined 1996 and 1997 data.124

7.3 Corrected 1995 and 1996-97 mean thrust ($\langle T_Z \rangle$) distributions as a function of mean Q shown with the ARIADNE hadron level results. 125

7.4 Corrected thrust distribution for 1995 data shown as a function of Q^2. The highest x range points have variable sized x intervals. 126

7.5 Ratio of 1995 and 1996+97 corrected thrust distribution, as a function of thrust, for the 11 overlapping kinematic bins. . . . 127

7.6 Corrected thrust distribution for 1995 data with systematic errors included. The inner error bars are statistical only with the outer as systematic and statistical combined in quadrature. 132

7.7 Corrected jet broadening distribution for 1995 data with systematic errors included. The inner error bars are statistical only with the outer as systematic and statistical combined in quadrature. 133

7.8 Corrected jet mass distribution for 1995 data with systematic errors included. The inner error bars are statistical only with the outer as systematic and statistical combined in quadrature. 134

7.9 Corrected C parameter distribution for 1995 data with systematic errors included. The inner error bars are statistical only with the outer as systematic and statistical combined in quadrature. 135

7.10 Corrected mean thrust distribution for 1995 data with systematic errors included. The inner error bars are statistical only with the outer as systematic and statistical combined in quadrature. 136

7.11 Corrected mean thrust distribution for 1996-97 data with systematic errors included. The inner error bars are statistical only with the outer as systematic and statistical combined in quadrature. 138

8.1 Fitted values of $\alpha_s(M_Z)$ and $\overline{\alpha_0}(2\text{ GeV})$ for each of the event shapes shown with the H1 results and the world average and theoretical prediction. 145

8.2 Mean event shape distributions (points) with the power corrected NLO prediction (lines) using the fitted values of $\Lambda^{[4]}_{\overline{\rm MS}}$ and $\overline{\alpha_0}$ shown in Tables 8.1 to 8.4. 146

List of Tables

1.1 Table of delivered and useful luminosity for years 1992-1997. . 4

1.2 Review of parameters for the Central Tracking Chamber. . . . 13

2.1 Table of variable dependent normalisation factors (a_F) and logarithmic power factor (p) for the power corrections to next to leading order predictions. 47

3.1 Table of nominal kinematic ranges to be used in the analysis of event shape variables and the corresponding number of selected events for each year's data. 57

4.1 Table showing Monte Carlo events generated to correct the 1995 and 1996 data samples. 74

4.2 Table of sensitive distributions to be included in $f\left(\chi^2\right)$. 77

4.3 Table of tuned parameters for DIS with ARIADNE 78

5.1 Table of event shape variable bin sizes. 93

6.1 Table of fitted coefficients to the NLO thrust (T_z) predictions from the DISENT Monte Carlo. 117

6.2 Table of fitted coefficients to the NLO jet broadening (B_c) predictions from the DISENT Monte Carlo. 118

6.3 Table of fitted coefficients to the NLO jet mass (ρ_E) predictions from the DISENT Monte Carlo. 119

6.4 Table of fitted coefficients to the NLO C parameter (C_E) predictions from the DISENT Monte Carlo. 120

8.1 Fitted values of $\overline{\alpha_0}$ and $\Lambda^{[4]}_{\overline{\mathrm{MS}}}$ for the combined 1995-1997 mean T_z distribution. 140

8.2 Fitted values of $\overline{\alpha_0}$ and $\Lambda^{[4]}_{\overline{\mathrm{MS}}}$ for the combined 1995-1997 mean B_c distribution with no $\log(Q/Q_0)$ term. 141

8.3 Fitted values of $\overline{\alpha_0}$ and $\Lambda^{[4]}_{\overline{\mathrm{MS}}}$ for the combined 1995-1997 mean ρ_E distribution. 141

8.4 Fitted values of $\overline{\alpha_0}$ and $\Lambda^{[4]}_{\overline{\mathrm{MS}}}$ for the combined 1995-1997 mean C_E distribution. 142

8.5 Fitted values of $\overline{\alpha_0}$ and $\Lambda^{[4]}_{\overline{\mathrm{MS}}}$ for the combined 1995-97 mean event shapes using the statistical and systematic errors combined in quadrature. 147

Chapter 1

The HERA machine and ZEUS detector

In this chapter an introduction to the HERA machine and the ZEUS detector is presented. Particular emphasis is paid to the ZEUS detector components central to the data analysis included in this thesis; these include the central tracking detector and depleted uranium sampling calorimeter. An outline of the ZEUS trigger system, relevant to the analysis presented, is given. Salient information regarding the track finding algorithm is also described.

Work completed by the author relating to a graphical user interface for the central tracking detector is presented. This interface is in regular use while the ZEUS detector is collecting data and forms the initial steps of a detector wide software development programme.

1.1 The HERA Machine

The Hadron Elektron Ring Anlage (HERA) is the first and, at present, only electron-proton colliding beam machine in the world. The machine consists of two independent 6336 m storage rings containing counter rotating beams of protons and electrons (or positrons). The electron[1] storage ring operates at a nominal energy of 27.5 GeV[2] whilst the proton ring has a nominal energy of 820 GeV[3]. The HERA project [1] was authorised in April 1984 and the first delivered luminosity was in the summer of 1992.

The HERA injection system utilises the linear accelerators (linacs) and accumulator rings of previous DESY experiments. A schematic of the HERA injection system and the main ring is shown in Figure 1.1. The system starts with a linac injecting 500 MeV electrons into the first storage ring (PIA) where they are stored in a single bunch until the current reaches 60 mA. The bunch is then transfered to the DESY II synchrotron and accelerated to ∼7 GeV before transfer to the PETRA II ring. This procedure is repeated at a rate of 12.5 Hz until 70 such bunches have accumulated 28.8 m apart in the PETRA II ring. These bunches are then accelerated to 14 GeV and injected into the HERA electron ring. This injection process is repeated twice until the HERA ring contains 210 electron bunches.

The procedure for the proton beam is somewhat similar. Firstly negatively charged hydrogen ions are injected into a 50 MeV linac. The H^- ions are stripped of their two electrons while entering the DESY III synchrotron and, as with the electrons, captured into a single bunch. The protons are then accelerated to 7.5 GeV and transfered to the PETRA II ring. When 70 such bunches have been collected they are accelerated to 40 GeV and injected into the proton ring of HERA. This is, as before, repeated twice to fill the HERA proton ring with 210 bunches of protons. Both the electron and proton rings have up to 220 buckets for particles bunches but only around

---

[1] hereafter electron is used to describe either an electron or positron.

[2] Here and throughout this thesis the natural units of $c = \hbar = 1$ are adopted.

[3] presently a higher proton energy of 920 GeV is being used.

Figure 1.1: HERA injection system.

200 are used. The empty and non-paired buckets are used to study beam induced and general backgrounds to a given event sample.

When the particle bunches of protons and electrons have been successfully stored in HERA they are accelerated up to the nominal energies. At these energies the bunch crossing time is 96 ns, which exerts tight requirement on any detector design so as to observe collisions resulting from these particles. An array of super conducting magnets produce the 4.68 Tesla (T) field required to store the 820 GeV protons. The 27.5 GeV electrons require only a field of 0.168 T which can be produced by conventional magnets.

In the left diagram of Figure 1.1 the four halls containing the experiments utilising HERA are shown. The ZEUS [2] and H1 [3, 4] experiments are situated in the South and North halls respectively. Both of these experiments are electron-proton beam collision experiments. The HERMES [5, 6] experiment, situated in the East hall, uses the polarised electron beam to collide with a fixed target to measure the spin structure of the proton and neutron. The West hall contains the HERA-B [7] experiment which uses the proton

Year	Delivered Luminosity	Useful Luminosity	e^-/e^+ Energy
1992	26.3 nb^{-1}	26.3 nb^{-1}	e^- 26.7 GeV
1993	1.09 pb^{-1}	0.54 pb^{-1}	e^- 26.7 GeV
Total	1.12 pb^{-1}	0.57 pb^{-1}	e^- 26.7 GeV
1994	1.08 pb^{-1}	0.28 pb^{-1}	e^- 27.2 GeV
Total	1.08 pb^{-1}	0.28 pb^{-1}	e^- 27.5 GeV
1994	5.11 pb^{-1}	3.02 pb^{-1}	e^+ 27.5 GeV
1995	12.30 pb^{-1}	6.66 pb^{-1}	e^+ 27.5 GeV
1996	17.16 pb^{-1}	10.71 pb^{-1}	e^+ 27.5 GeV
1997	36.35 pb^{-1}	26.55 pb^{-1}	e^+ 27.5 GeV
Total	70.92 pb^{-1}	46.94 pb^{-1}	e^+ 27.5 GeV

Table 1.1: Table of delivered and useful luminosity for years 1992-1997.

beam to collide with a fixed target and investigate CP violation in beauty events.

The delivered luminosity from the HERA machine, luminosity collected by the ZEUS detector and electron energy are shown in Table 1.1; throughout this time the proton energy was 820 GeV. A plot of the integrated luminosities, delivered by the HERA machine, for each year of running is shown in Figure 1.2. Since the HERA machine has been active both the delivered and useful integrated luminosities per year have increased more than by three orders of magnitude. This has allowed precision tests and measurements of QCD including the definition of proton structure, the heavy flavour content of the proton and studies of diffractive physics.

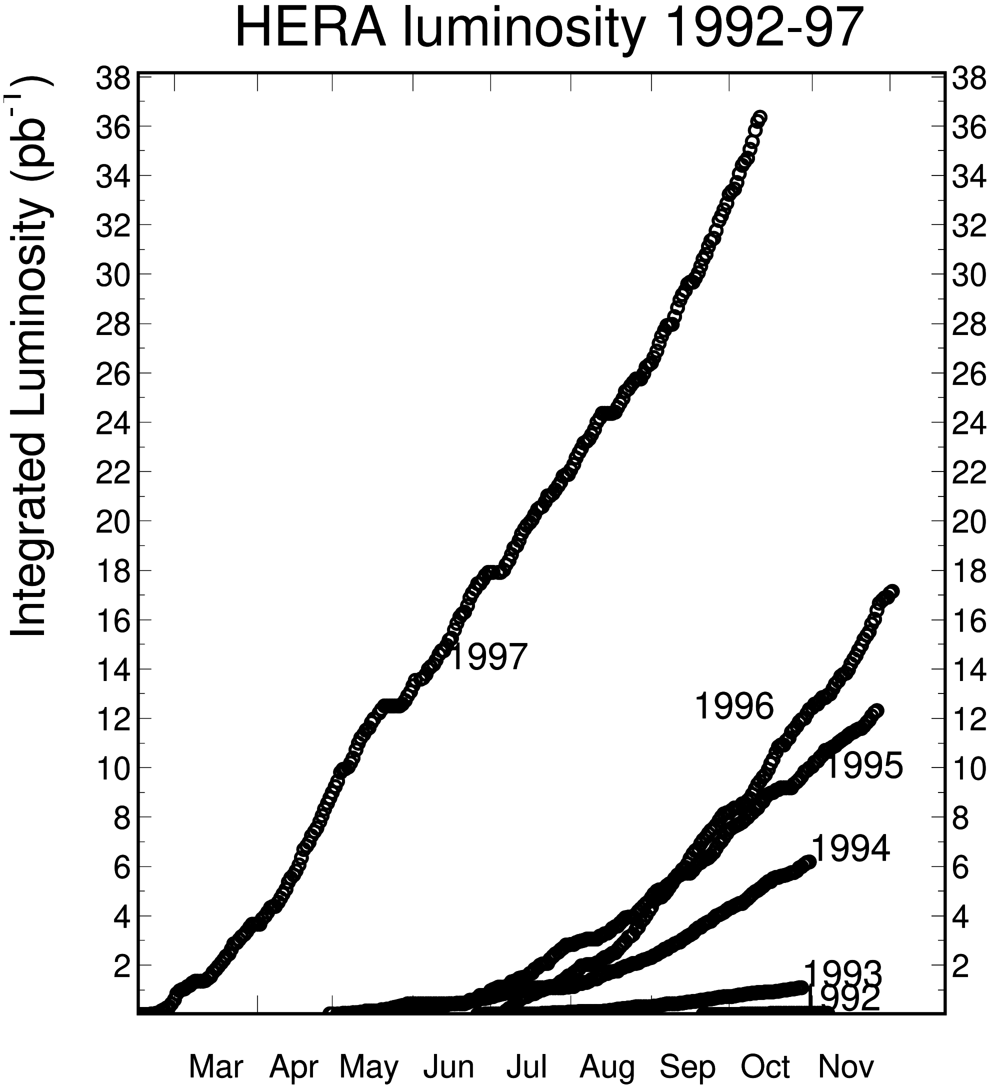

Figure 1.2: Delivered luminosity from the HERA machine for each year.

1.2 The ZEUS Detector

The ZEUS detector was designed as a multipurpose detector for physics analyses. The design is optimised to measure the characteristic event topologies prevalent in electron proton collisions. The longitudinal and transverse cross section of the ZEUS detector are shown in Figures 1.3 and 1.4 respectively. The major components have been labelled on the diagram with their acronyms.

The ZEUS coordinate system aligns the positive z-axis with the incoming proton direction, also called the forward direction. The positive x-axis points toward the centre of the HERA ring, while the positive y-axis points upwards. The origin is defined by the nominal interaction point and completes the right-handed coordinate system.

The most obvious feature of the ZEUS detector is the asymmetric design. This asymmetry compensates for the boost of the centre-of-mass system of the colliding particles in the forward direction. This also accounts for a higher density of high momentum particles in the forward region in comparison to the rear. For this reason the forward region has additional instrumentation.

A full description of the detector is beyond the scope of this thesis. An abridged description of the detector components relevant to this work, such as the tracking detectors and calorimetry, will be presented and further details can be sought elsewhere [2].

Moving outward from the nominal interaction point one first encounters the Vertex Detector (VXD)[4] and then the Central Tracking Detector (CTD), which comprise the main components of charged particle detection. In addition to these two components there is a Forward Tracking Detector (FDET), situated forward and backward of the CTD, which complements the charged

---

[4] present during the 1995 data taking period only.

particle detection. The FDET consists of 4 planar drift chambers each of which have a pair of Transition Radiation Detectors (TRDs) sandwiched between them. These components make up the inner tracking detector (see section 1.3). However, after the initial running period of ZEUS an additional tracking detector, the Small Angle Rear Tracking detector (SRTD), was installed to improve low angle measurements of the scattered electron.

Surrounding the inner tracking detector is a thin superconducting solenoid which produced a field of 1.43 T. This enables an accurate momentum measurement of particles detected by the inner tracking detector. The effect of this field on the HERA beams is corrected by a high field superconducting compensating solenoid located in the rear area of the return yoke. Surrounding the central solenoid is an almost hermetic[5] depleted uranium-scintillator sampling calorimeter. The calorimeter is geometrically divided into 3 parts, each covering a different area of the interaction. The first part is the Forward Calorimeter (FCAL) encompassing the range $2.2^\circ \leq \theta \leq 39.9^\circ$ where θ is the polar angle. The Barrel Calorimeter (BCAL) encompasses the region $36.7^\circ \leq \theta \leq 129.1^\circ$ producing some overlap with the FCAL and also with the Rear Calorimeter which encompasses the region $128.1^\circ \leq \theta \leq 176.5$. Each part of the calorimeter is segmented into electromagnetic and hadronic sections.

Between the calorimeter and the inner tracker is the presampler (PRES) which consists of a Forward, Barrel and Rear section, labelled FPRES, BPRES and RPRES. The PRES was in the process of being installed during the period in which the data presented in this thesis was taken, thus it was not used in this analysis. Its purpose is to investigate the loss of energy, due to dead material, in jets measured by the calorimeter and it usefulness to

---

[5] a pair of 20cm × 20cm gaps accommodate the beam pipe.

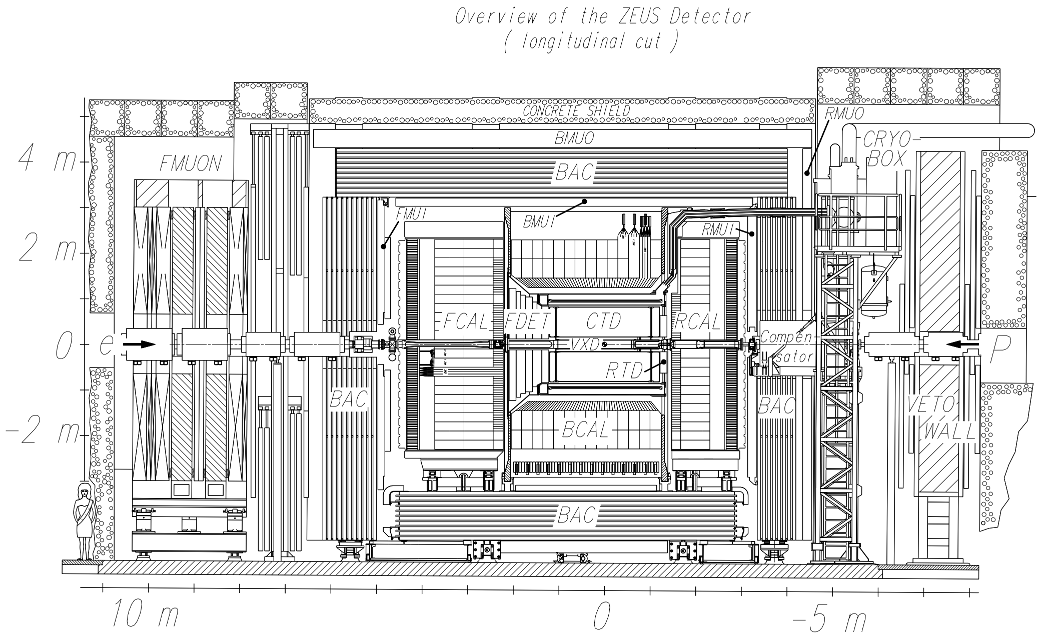

Figure 1.3: The $(r - z)$ cross section of the ZEUS Detector.

further work based on this analysis is discussed briefly in the conclusions.

A further layer beyond the depleted uranium calorimeter is the Backing Calorimeter (BAC). This acts as not only as further calorimetry for leaking activity from the DU calorimeter but also as a muon tagger and the return yoke for the tracking magnet.

Finally, on the outer layer of the detector and on the inside of the BAC are the Forward, Barrel and Rear Muon (FMUON/BMUON/RMUON) detectors. There are no specific muon chambers located under the detector so the BAC has to be relied upon in this region. The measurement of luminosity is performed with a downstream detector (LUMI) measuring the Bethe-Heitler process. Also a veto wall is situated upstream with respect to the proton direction and is used to eliminate proton induced beam gas events arriving at the detector.

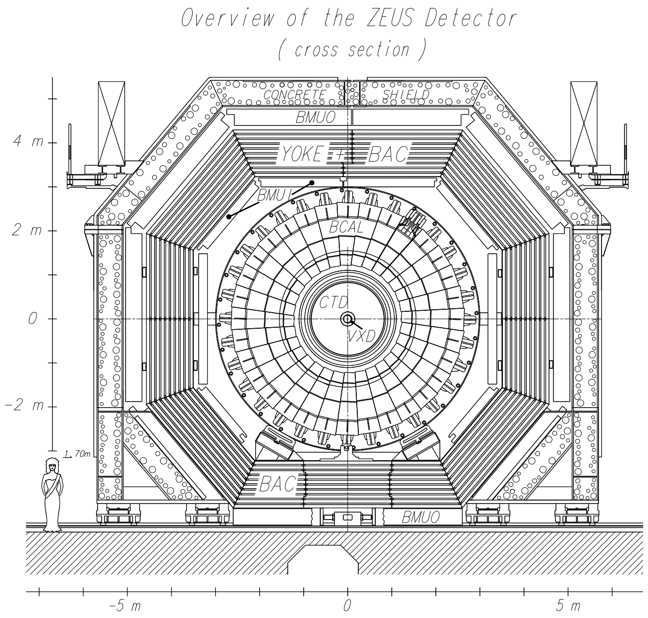

Figure 1.4: The $(r - \phi)$ cross section of the ZEUS Detector.

1.3 Inner Tracking Detector

The detection of charged particles in the ZEUS detector is achieved using the inner tracking detector. The angular coverage encompasses the range $7.5^\circ \leq \theta \leq 170^\circ$. The inner tracking detector is a combination of a number of components which include the VXD, CTD, FTD and RTD. The inner tracking detector was designed with adherence to several objectives:

- separation and reconstruction of charged and neutral current events over a wide range of Q^2;
- reconstruction of the final state hadrons and leptons with momentum resolution $\sigma(p_\perp)/p_\perp$ better than 0.003 $p_\perp$ on high momentum tracks over a wide angular range;
- electron tagging with dE/dx and the TRD, as well as by comparison to calorimeter cells;
- suppression of muons from hadron decay in flight, for example $\pi^\pm \rightarrow \mu^\pm \overset{(-)}{\nu}_\mu$ or $K^\pm \rightarrow \mu^\pm \overset{(-)}{\nu}_\mu$;
- reconstruction of tracks close to the production vertex, particularly in studies of dynamics in heavy flavour production due to their short decay paths; and,
- event triggering using production vertex information, particularly of importance in charged current and fast muon triggers.

To distinguish tracks very close to the interaction point, and thus perform studies on short lived particles, the VXD was developed. In addition to this the VXD was designed to give improved momentum and angular resolution on charged tracks. The VXD was only used for the 1995 data taking period, it was removed during the following shutdown. However, development of a silicon micro vertex detector [8] is underway and will be installed during the 1999-2000 shutdown period, which is before a high luminosity running period. This new detector is hoped to give an intrinsic hit resolution $\sim$20 μm and allow precision studies of charm physics in electron-proton collisions.

1.3.1 The Central Tracking Detector

For this work all the charged particle detection, over a wide range in θ, was carried out using the CTD. The CTD consists of a cylindrical wire chamber utilising nine SuperLayers (SLs), each with eight sense wire layers. The length of the CTD is 241 cm with inner and outer radii of 16.2 cm and 85 cm respectively, the active volume is somewhat smaller than this giving an angular coverage of $15^\circ \leq \theta \leq 164^\circ$.

Of the nine superlayers, five have sense wires parallel to the chamber axis ($\theta = 0^\circ$) and four have small stereo angles ($\theta = \pm 5^\circ$). A diagram of the wire layout at an end plate, for one octant of the CTD, is shown in figure 1.5. A review of CTD sense wire parameters can be found in table 1.3.1. Due to the inclusion of the small stereo angle the z measurement using the stereo wires has a resolution of 1.0 to 1.4 mm. In addition to this method of z position measurement the non-stereo wires are connected to z-by-timing systems which calculate the position from differences in charge arrival time. The resolution in z position from this method is around 3-4 cm. The innermost sense layer gives a polar angle (θ) resolution down to 200 mrad, which can then be used for linking tracks to the FDET.

As mentioned before the solenoid operates with a relatively high magnetic field of 1.43 T, which provides good resolution on the momentum measurement of charges particles. The sense wire planes are tilted at 45° to the

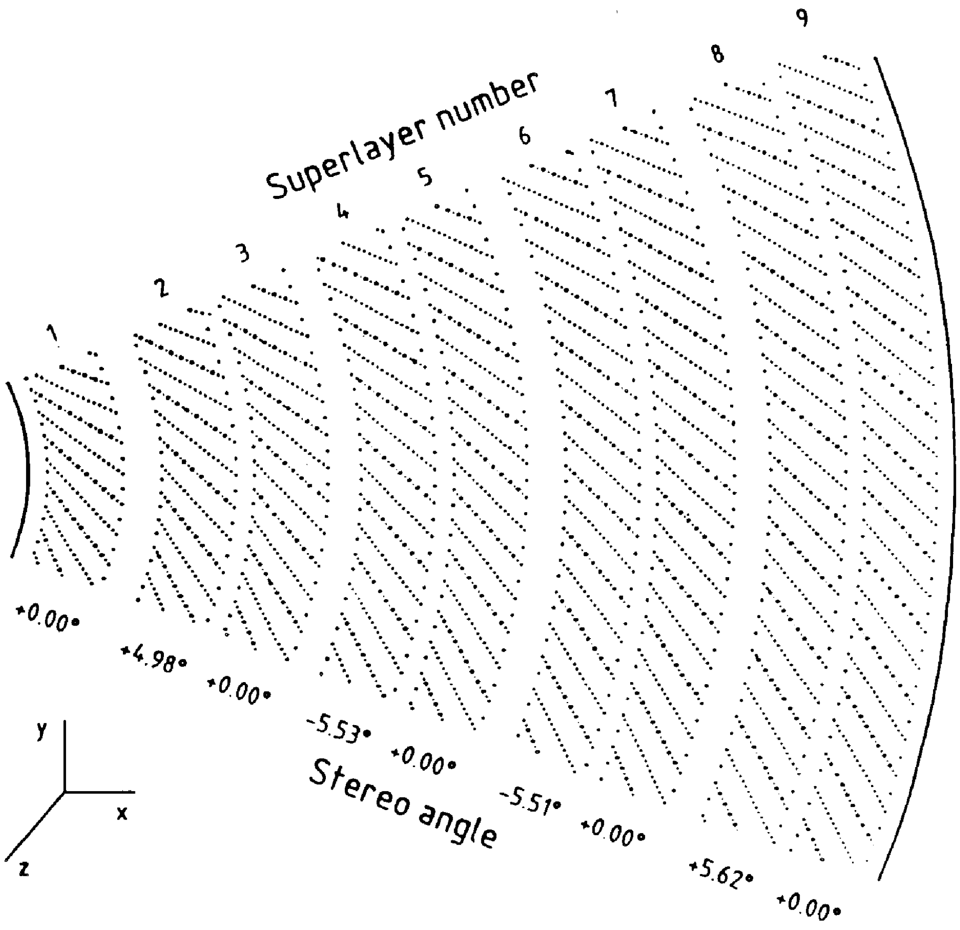

Figure 1.5: Wire layout in a single octant of the Central Tracking Detector. Alternating layers of sense and field wires are indicated by the dots. The larger dots are the sense wires.

SL	Number Of Cells	Stereo Angle (°) mean	min	max	Centre Radius Of Cell (cm)	Θ Range (°)
1	32	0			20.97	11.3-168.2
2	40	4.98	4.64	5.32	27.23	14.5-164.8
3	48	0			35.00	18.4-160.7
4	56	-5.31	-5.06	-5.55	41.30	21.5-157.3
5	64	0			48.73	24.9-154.0
6	72	-5.51	-5.31	-5.69	55.52	27.9-151.0
7	80	0			62.74	30.9-147.9
8	88	5.62	5.46	5.77	69.46	33.5-145.2
9	96	0			76.54	36.1-142.6

Table 1.2: Review of parameters for the Central Tracking Chamber.

radial direction which produces field lines perpendicular to high momentum particles originating from the interaction point, thus providing optimum resolution and reducing left-right ambiguity. This arrangement of wires produces a maximum drift length of approximately 2.5 cm which requires a gas with a fast drift velocity of 50 μm/ns. The CTD uses a 90/8/2 argon/carbon dioxide/ethane gas mixture. The inclination of the sense wire cells also ensures that a charged particle always crosses several planes and guarantees at least one drift time less than 96 ns to separate events from neighbouring bunch crossings.

The CTD Local Run Control System

When an interesting event occurs during a collision the data from the CTD is piped to a transputer network. The network uses various algorithms to determine if the data is useful (see section 1.7). The decision-making process needs to be in synchronisation with all other ZEUS detector components. A logical condition of all these decisions is evaluated and the data kept or discarded. This synchronisation is performed by the trigger system using a global detector clock.

With so many components active during data taking, monitoring their status and controlling their actions is imperative. The system which monitors and controls the status of all detector components is the ZEUS Run Control (RC). The ZEUS RC has the ability to turn on, turn off, set up and activate all detector components. The ZEUS RC interface is a window-based program that has various buttons to perform various actions, such as starting or stopping the detector taking data, by the transmission of command protocols through a network system [9].

In addition to the basic ZEUS RC control some components, such as the CTD, need to perform individual test and calibration procedures. This is most easily achieved by another RC interface specific to the component and using the same networked command protocols. The new interface designed for the CTD is called the Local Run Control (LRC).

It is designed with the same layout as the ZEUS RC interface, using a similar window-based program containing the main buttons (SETUP, ACTIVATE and END). In addition to the basic commands present in the ZEUS RC others were added. These included a button to perform a calibration of the CTD and another to stop the ZEUS RC from controlling the CTD. A picture of the main window can be see in figure 1.6(a). The CTD has three states, common to all detector components, which are *Idle*, *Ready* and *Active*. These states can be seen, represented by ellipses, in the main window. One can deduce that the CTD is in the *Ready* state from the highlighted nature

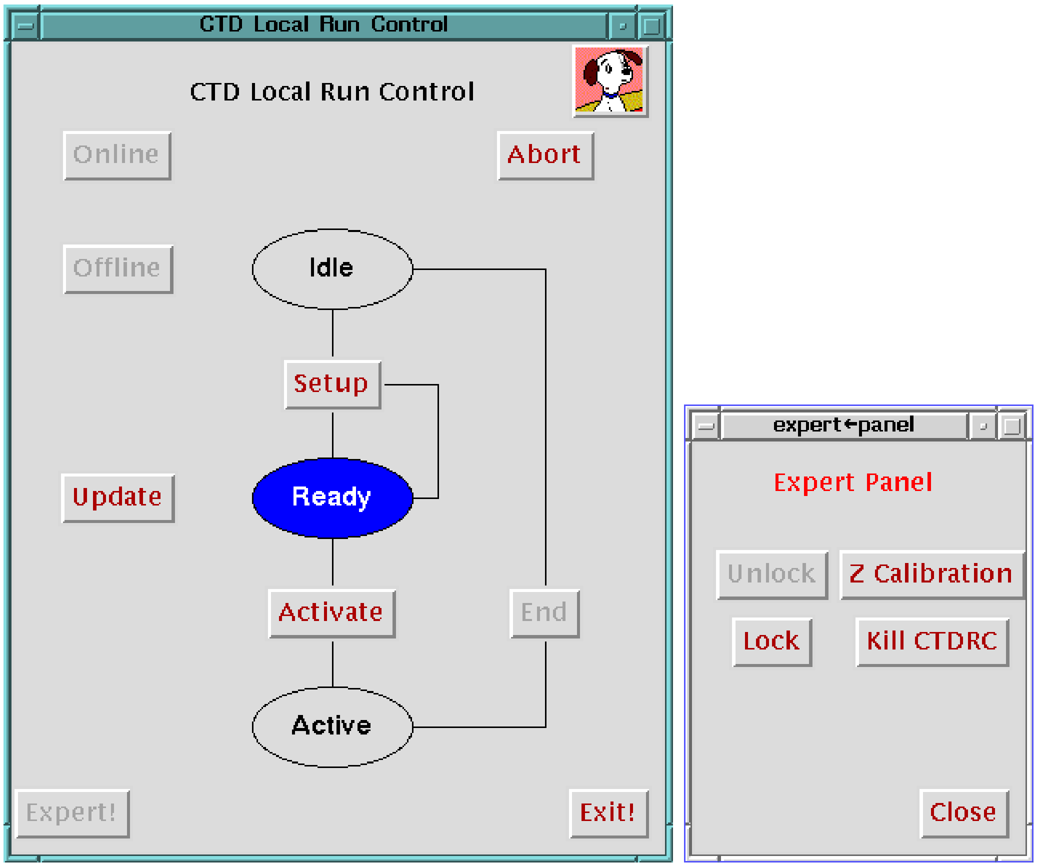

Figure 1.6: (a) The Local Run Control main window, (b) The Local Run Control expert panel.

of the relevant ellipse.

In figure 1.6(a) the three main buttons, SETUP, ACTIVATE and END, can be clearly seen. A difference between the END button and the other two can also be seen; the END button is not highlighted to the same extent. This is due to the internal logic of the object orientated code which disables this button. The code for the interface was written in the Tcl-Tk [10] language, with additional language constructs for the network message protocol added via the C language [11].

The Tcl-Tk language allows the definition of all objects, such as the buttons, and how they react to certain stimuli. As can be concluded from figure 1.6(a) the CTD is in the *Ready* state. The fact that the CTD is in this state informs the LRC that it can instigate two actions, either another setup or activation. In the present state the code's logic disables, temporarily, the END button. If the CTD were in the *Active* state then only the END button would be highlighted, and the other two disabled. The code's logic defines all relevant situations and the required button configuration.

Another button visible in figure 1.6(a) is the EXPERT button. This button is disabled unless the CTD is in the *Idle* state. When activated the expert panel appears. The expert panel can be seen in figure 1.6(b). This panel contains CTD specific actions useful to a CTD expert. It is such a simple design that an inexperienced operator will be able to follow simple instruction if no expert is available. This is the essence of the design philosophy. Further information about the central tracking detector's local run control was presented in an internal ZEUS note [12].

1.3.2 The Forward And Rear Tracking Detector

The Forward Tracking Detectors (FTDs) consist of three planar drift chambers covering the angular region $7.5^\circ \leq \theta \leq 28^\circ$. The Rear Tracking Detector (RTD) is of similar design and covers the angular region $160^\circ \leq \theta \leq 170^\circ$. The final component is the Transition Radiation Detector (TRD) comprised of four chambers, each equipped with 70 mm thick radiation material, and one plane of cathode and anode readout wires. The FDET was installed to improve the angular coverage of the CTD in the small and large polar angle region, where the CTD's wire orientation becomes unfavourable. With the inclusion of these two detector components the angular coverage of the inner tracking system increases to $7.5^\circ \leq \theta \leq 170^\circ$; a single straight track crosses 54 wires at 7.5°, 72 at 90° and 18 at 170°.

1.3.3 The Small Angle Rear Tracking Detector

During 1995 a proposal was submitted relating to the construction and installation of a new tracking component which would improve the detection of scattered electrons occurring from low x and moderate Q^2 events (see section 2.1). In these events the electron is scattered by and loses energy to the large amount of dead material near the beampipe and in front of the depleted uranium calorimeter. An enhancement in the measurement of angle and the evaluation of an energy correction for the dead material would improve the kinematic reconstruction and allow precision measurements.

The analysis presented in this thesis only incorporated the SRTD at low Q^2 (from 10-20 GeV^2 or so), the suppression of upstream proton interactions is relevant only as a background. The SRTD has a position resolution in x and y of $\simeq 0.4$ cm while the timing resolution is < 0.75 ns. The energy loss function is parameterised as $E_{lost} = 0.08 + 0.02 E_{SRTD}$, where E_{lost} and E_{SRTD} are given in GeV.

1.4 Calorimetry at ZEUS

The objective of the calorimetry at ZEUS is to measure high multiplicity and high density jets, detect neutral particles, distinguish between hadrons and leptons and provide a high degree of energy resolution for both hadrons and electrons. All these have been achieved with the combination of the Depleted Uranium (DU) Calorimeter, Hadron Electron Separator (HES) and the Backing Calorimeter (BAC). Another useful aspect of the calorimetry is the increased precision on the measurement of high momentum particles, where the tracking detectors fail due to the small curvature of particles in the field. In addition, in the study of charged current interactions the presence of a neutrino can only be inferred by missing energy, thus requiring a hermetic detector that can detect both charged and neutral particles.

1.4.1 The Depleted Uranium Calorimeter

The depleted uranium calorimeter was designed with this caveat in mind "... the measurement of jets as key to the study of physics at HERA". This ordered the priorities of the DU calorimeter as follows:

- full solid angle coverage,
- jet energy resolution of $\sigma\left(E\right)/E = 35\%/\sqrt{E} \oplus 2\%$,
- electron energy resolution of $\sigma\left(E\right)/E = 18\%/\sqrt{E} \oplus 1\%$,
- angular resolution of jets better than 10 mrads, and
- hadron electron separation for isolated electrons and electrons in jets.

It is a sampling calorimeter which completely surrounds the solenoid and inner tracking detector. The solid angle coverage is 99.8% in the forward and 99.5% in the rear hemisphere. The calorimeter is divided into 3 regions to cover the forward, barrel and rear directions. Each section is subdivided longitudinally into two parts; the inner part functions as the electron calorimeter with a depth of $\sim 25X_0$ ($\sim 1\lambda$) and the outer part functions as a hadronic calorimeter which varies in depth from 6λ, in the forward region, down to 3λ, in the rear. A single FCAL module is shown in figure 1.7. As can be seen from the figure both the electromagnetic and hadronic sections are constructed from a sandwich of depleted uranium tiles wrapped in a stainless steel foil, each of thickness 3.3 mm, and a plastic scintillator plate wrapped in reflective paper, each of thickness 2.6mm. Each sampling layer is coupled, via two wavelength shifters, to a pair of PhotoMultiplier Tubes (PMTs). The signal measured by the PMT is proportional to the energy sampled by that layer. The total number of PMTs is 11,836.

Each sampling layer of DU and plastic scintillator has been optimised to be 1 X_0 thick, and to give equal response to electrons and hadrons ($e/h \sim 1$), that is to self-compensate for the energy loss due to binding energy. When a hadron enters a calorimeter some of its energy is used in the breakup of heavy nuclei in the form of binding energy. However, with depleted uranium the lost energy can be recouped by self-compensation.

A fraction of the hadrons energy is used in the production of spallation neutrons, these neutrons then scatter elastically with the free hydrogen atoms in the plastic scintillator. These elastic scatters produce ionisation from the hydrogen nuclei which can be detected by the PMTs. The DU tiles and scintillator have been optimised to produce the same amount of energy from this process as that lost from binding energy, this is self-compensation. The resulting energy resolutions, evaluated from test beam studies, for hadrons and electrons are (sampling $\oplus$ systematic):

$$\frac{\sigma(E)}{E} = \frac{0.35}{\sqrt{E}} \oplus 0.02 \tag{1.1}$$

and

$$\frac{\sigma(E)}{E} = \frac{0.17}{\sqrt{E}} \oplus 0.01 \tag{1.2}$$

respectively, where E is in GeV. This shows a slightly improved electron energy resolution over the design specifications. The angular resolution for jets is better than 10 mrads. The time resolution for energy deposits is around 1 ns, which should be compared with the much longer bunch crossing time of 96 ns.

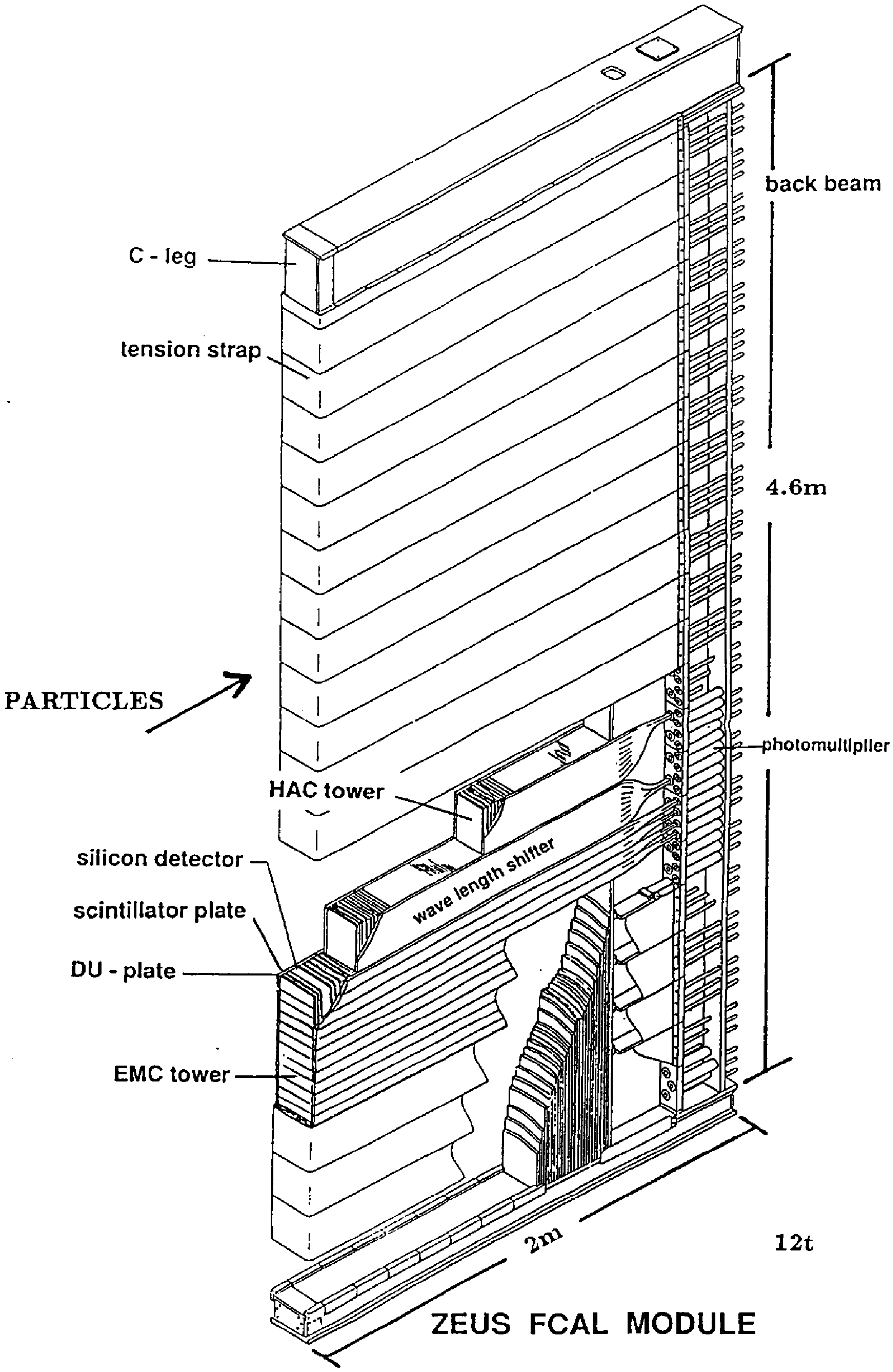

Figure 1.7: A single module of the Forward Calorimeter.

1.4.2 The Hadron Electron Separator

The interaction length of a hadron shower is 20 times that of an electron shower. This results in electron showers starting earlier and being narrower than the, comparatively wide, hadron showers. The inclusion of the Hadron Electron Separator (HES) was intended to exploit this difference. Gaps are provided between the 4th and 7th sampling layers of the FCAL and after the 4th sampling layer in the BCAL and RCAL to include the HES.

The HES consists of 10406 silicon diode detectors (3cm × 3cm) in the rear calorimeter, RHES, and 5216 in the forward calorimeter, FHES. Pairs of silicon diodes are mounted, with pre-amplifiers, on ceramic cards. The high degree of position resolution offered by the HES improves the segmentation of the calorimeter by an order of magnitude. The installation of the HES was completed this year and was not used in the analysis presented in this thesis.

1.4.3 The Backing Calorimeter

The iron yoke that provides the return path for the magnetic solenoid is also instrumented to perform detection of muons traversing the barrel (see section 1.5) and to measure any hadronic leakage from the depleted uranium calorimeter. The construction is an array of 7.3 cm thick iron plates with 3.7 cm aluminium proportional tubes (7-8 tubes per module). The energy resolution for the BAC is:

$$\frac{\sigma(E)}{E} \sim \frac{1.1}{\sqrt{E}} \tag{1.3}$$

with a spatial resolution of the order of 1 mm for muons.

1.5 The Muon Detectors

Muon identification is carried out not only by the BAC but also by an array of dedicated muon chambers. Muon detection is of great importance in the study of heavy flavour and exotic processes but also in the reduction of background from beam gas, cosmic and halo muon production. Each of the muon detectors (FMUON, BMUON and RMUON) have inner and outer instrumentation sandwiching the magnetised iron toroid of the return yoke (the BAC). Measurement of the incoming and outgoing trajectories will give an estimate of momentum.

The FMUON consists of four planes of instrumentation, two inside and two outside the toroid. These planes are composed of both drift chambers and Limited Streamer Tubes (LSTs), providing polar coordinate measurements. The BMUON and RMUON detectors are of similar construction with the BMUON having two double layers and the RMUON a single double layer of LST inside and outside the iron toroid.

1.6 The Luminosity Monitors

The luminosity is monitored through measurements of the bremsstrahlung process [13] which can be calculated using the Bethe-Heitler equation [14]. It is based on the detection in coincidence of the final state electron and photon which are emitted at very small angles with respect to the initial electron direction. The Luminosity monitor (LUMI) consists of the photon detector close to the proton beam pipe at a distance of 104 to 107 m and an electron detector near the “electron” beam at a distance of 35 m. The “electron” beam magnets act as a spectrometer for electrons with energy less than the beam energy and deflect them out of the beam pipe to be detected.

1.7 The ZEUS Trigger

The trigger deployed on the ZEUS detector is a three level system. The First Level Trigger (FLT), must reduce the data flow rate, from around 10 kHz, to the more manageable rate of 1 kHz for the Second Level Trigger (SLT). To achieve this, in the time it has available, the FLT uses crude but effective algorithms which are designed to eliminate the high backgrounds from "non-physics" events. These backgrounds include beam gas, beam halo and cosmic muon interactions. These can be excluded by timing requirements taken, primarily, from the calorimeter.

The SLT has more time to process data from the detector components and can thus apply more sophisticated algorithms to the fully digitised data. The SLT looks at various parameters such as an electron or photon tagged in the LUMI system and beam gas rejection from track vertex fitting using the CTD. In addition to the background vetoing the SLT also performs a simple event classification for use at the Third Level Trigger (TLT). The classification of events as deep inelastic scattering can be determined by such things as electromagnetic deposits (for neutral current) or missing energy (for charged current). This process reduces the rate further to around 100 Hz.

Once an event has passed the SLT the digitised data is sent to the Event Builder (EB). The EB performs full reconstruction of the digitised data. This event record is then passed to the TLT.

At the TLT the whole event record is analysed by a reduced version of the off-line analysis routines. This performs final reduction of background from sparks in the calorimeter PMTs, more accurate timing requirements and a full rejection of cosmic or halo muons. The remaining events are then classified into "types", such as deep inelastic scattering, heavy flavour and photoproduction, the output rate at this point is around 10 Hz which is slow enough to be passed to the storage facility and written to disk.

1.7.1 Track Reconstruction

A standard track fitting package, called VCTRAK [15], is used to assign hits found using the CTD to vertex and non-vertex originating trajectories and then extrapolate them into the other components of the inner tracker. This package can be used in full inner tracker or CTD only mode. For the analysis presented in this thesis the CTD only mode is used.

The track fitting algorithm starts with a “seed”; where a “seed” is defined as three CTD axial wire hits, or if used in full inner tracker mode as a single track segment in the RTD plus a single CTD axial hit or as a single hit in the SRTD plus a SL1 axial hit. This initial “seed” is then extrapolated inwards collecting additional hits. As this occurs the trajectory parameters are tightened with the inclusion of each new hit, some of which are stereo hits which combine to give 3D information.

The tracks found from this iteration process are then used as the basis for a five parameter helix fit. During this procedure some acquired hits can be swapped or dropped to improve the fit. The final set of trajectories are used as input to a vertex fitting procedure. This may produce tracks which will not be classed as vertex originating and are not included in the vertex track set.

From this procedure two tracking sets are produced which are used in the analysis presented in this thesis. The set of vertex fitted tracks is used as the default method. However, the set which includes all tracks is also used as a systematic check. This is presented and discussed later.

Chapter 2

Theory

The kinematics of deep inelastic lepton nucleon scattering and the Lorentz invariant variables used to describe such events are introduced in this chapter. The idea of the Quark Parton Model is discussed and some predictions and limitations of such a model presented. Cross sections for deep inelastic scattering are shown which result from the premise of a partonic structure of the proton.

The introduction of the strong force mediator, along with the strong coupling constant α_s, will subsequently be required which then forms the QCD improved Quark Parton Model.

The naïve Quark Parton Model is used to introduce the Breit frame and the benefits of such a frame for deep inelastic *ep* scattering analyses are outlined. The effect on this simple model of the inclusion of higher order QCD terms is presented.

The event shape variables presented in this thesis are defined and interpreted in term of QCD calculations.

The final section deals with power corrections to the next to leading order predictions and their theoretical basis. A number of functional forms for the power corrections are described which will be used later in the fitting of data and extraction of the phenomenological parameter $\overline{\alpha_0}$ and the strong coupling constant α_s.

2.1 Kinematics Of Deep Inelastic Scattering

Deep inelastic scattering, at the simplest level, consists of an incoming lepton interacting with a nucleon via the exchange of an electroweak current in the form of an intermediate vector boson. The momentum exchange is enough for the nucleon to break up into a hadronic system, denoted as X. Two processes can be distinguished, neutral and charged current deep inelastic scattering. In neutral current deep inelastic scattering the exchanged boson is either a virtual photon (γ^*) or Z^0 boson and the process can be expressed as:

$$e^{\pm}p \longrightarrow e^{\pm}X \tag{2.1}$$

In the case of charged current deep inelastic scattering the force mediating boson is either a virtual W^+ or W^-, depending on the electroweak charge and flavour of the lepton and quark, and the proton can be expressed as:

$$e^{\pm}p \longrightarrow \overset{(-)}{\nu}_e\, X \tag{2.2}$$

The two different classes of deep inelastic scattering are represented in figure 2.1. Both interactions have a final state hadronic system, X, but are distinguished by the presence or absence of a detected final state lepton.

The initial and final state electron (or neutrino) can be defined with four momentum $\mathbf{k_i} = (\vec{k_i}, E_e)$ and $\mathbf{k_f} = (\vec{k_f}, E'_e)$ respectively and the incoming proton is defined with four momentum $\mathbf{p_i} = (\vec{p_i}, E_p)$. Ignoring particle masses, which is a valid approximation at HERA energies, the total centre

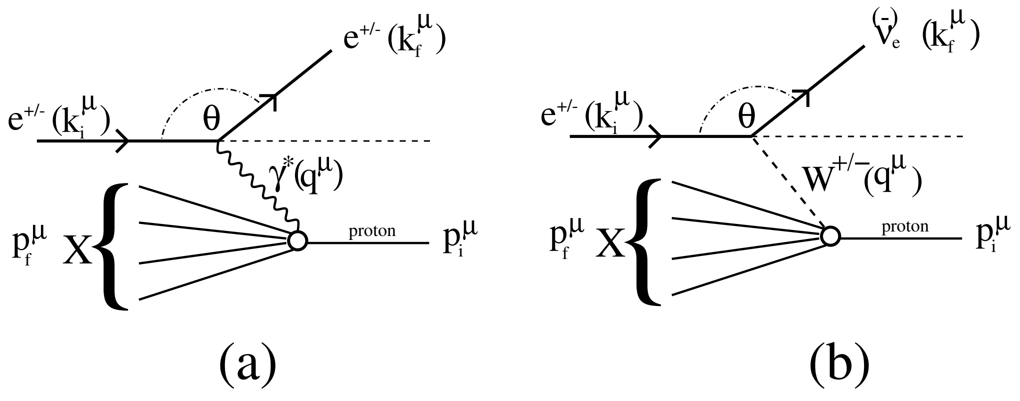

Figure 2.1: Schematic representation of (a) Neutral Current and (b) Charged Current Deep Inelastic Scattering of an electron off a proton, forming a hadronic final state X.

of mass energy, $\sqrt{s}$, is given by:

$$s = (\mathbf{k_i} + \mathbf{p_i})^2 \simeq 4E_eE_p \tag{2.3}$$

Thus, with the nominal electron and proton beam energies the centre of mass energy is 300 GeV. During and after the 1998 run period HERA will operate with an increased proton energy of 920 GeV, this 12% increase in proton energy will give a 6% increase in the centre of mass energy to 318 GeV.

From the incoming and outgoing electron's four momenta we can calculate the four momentum of the exchanged vector boson, denoted by $\mathbf{q}^\mu$. We can also define the momentum transfer from the electron to the proton constituent as the negative square of the exchanged boson's four momentum.

$$Q^2 = -\mathbf{q}^2 = -(\mathbf{k_i} - \mathbf{k_f})^2 \tag{2.4}$$

The value of Q^2 can be between 0 and s and is a measure of the distance scale with which the virtual boson is probing the proton. If the value of Q^2 is greater than zero then the exchanged photon can have both transverse and longitudinal polarisation. Other Lorentz invariant variables which describe the kinematics of deep inelastic scattering are defined by:

$$x = \frac{Q^2}{2\mathbf{p_i}.\mathbf{q}} \tag{2.5}$$

$$y = \frac{\mathbf{p_i}.\mathbf{q}}{\mathbf{p_i}.\mathbf{k_i}} \tag{2.6}$$

$$W^2 = (\mathbf{p_i} + \mathbf{q})^2 = Q^2\left(\frac{1-x}{x}\right) \tag{2.7}$$

The variable x, the Bjorken scaling variable, can be considered as the fraction of the proton's momentum carried by the probed constituent (see section 2.2). The variable y can be considered as the fractional energy lost by the electron, in the proton rest frame. The variable W^2 is the invariant mass squared of the hadronic final state system X.

The classification of an event as "inelastic" is taken when the value of W is greater than the mass of the proton (i.e. the proton has broken up into a hadron system of greater invariant mass). An event can be classified as "deep" when the value of Q^2 is larger than the mass of the proton.

For a given centre of mass energy only two Lorentz scalar variables are needed, usually x and Q^2, to fully define the kinematics of the interaction. A useful relation between the kinematic variables, again neglecting masses, is given by:

$$Q^2 = sxy \tag{2.8}$$

The experiments at HERA cover a hitherto uninvestigated region of x and Q^2. A diagram of the phase space covered by the two experiments ZEUS and H1, along with previous fixed target experiments, is shown in figure 2.2.

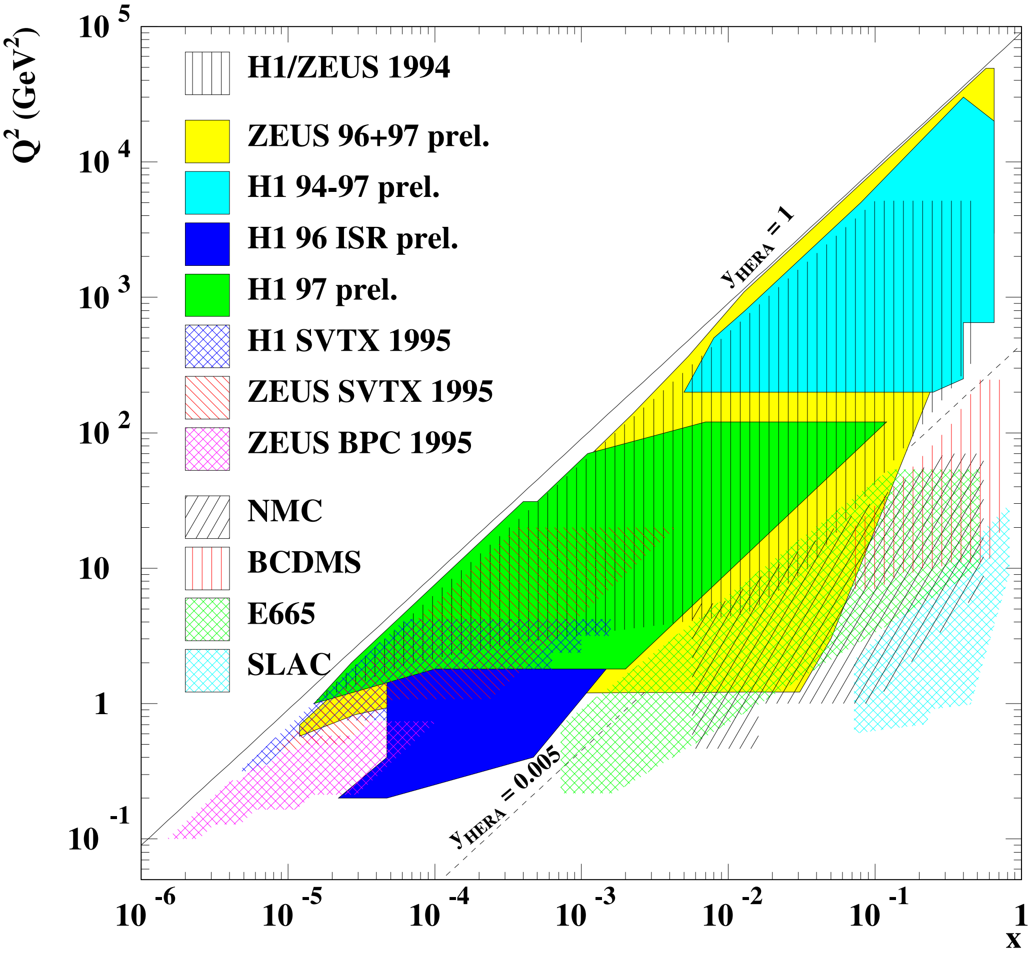

Figure 2.2: The kinematic phase space covered by the ZEUS and H1 experiments with previous fixed target experiments shown for comparison.

2.2 Cross Sections And The Parton Model

It is possible to calculate a cross section for such DIS events using electroweak theory, depending on the value of Q^2 or the importance of the electroweak interference terms.

One can parameterise the coupling of the lepton to the intermediate vector boson with a symmetric leptonic tensor, $L_{\mu\nu}$. At the other vertex we define $W^{\mu\nu}$ which incorporates the underlying partonic dynamics. Thus, our cross section can be written in terms of these tensors.

$$\sigma \sim L_{\mu\nu} W^{\mu\nu} \tag{2.9}$$

This cross section reduces, via symmetry and conservation laws, to a simpler form. It has also become more fashionable to perform a change of variables from the hadronic tensor components, W_i, to the more elegant structure functions F_i which can be related to parton densities more easily. Thus, the electroweak cross section for deep inelastic scattering can be written:

$$\begin{aligned}\frac{d^2\sigma^{e^\pm p}}{dQ^2dx} = \frac{4\pi\alpha^2}{xQ^4}\Bigg[&\frac{y^2}{2}F_1(x,Q^2) + (1-y)F_2(x,Q^2) \\ &\mp (y - \frac{y^2}{2})xF_3(x,Q^2)\Bigg]\end{aligned} \tag{2.10}$$

where $F_1(x,Q^2)$ is the structure function which relates to the exchange of both transversely polarised photons, $F_2(x,Q^2)$ relates to the exchange of transversely and longitudinally polarised photons and $F_3(x,Q^2)$ relates to the parity violating term. As noted before this final term only becomes important when $Q^2 \simeq M_{Z^0}^2$. If we define a longitudinal structure function, $F_L(x,Q^2)$, as $F_2(x,Q^2) - 2xF_1(x,Q^2)$ then 2.10 simplifies further to :

$$\begin{aligned}\frac{d^2\sigma^{e^\pm p}}{dQ^2dx} = \frac{2\pi\alpha^2}{xQ^4}\big[&(1+(1-y)^2)F_2(x,Q^2) - y^2F_L(x,Q^2) \\ &\mp (1-(1-y)^2)xF_3(x,Q^2)\big]\end{aligned} \tag{2.11}$$

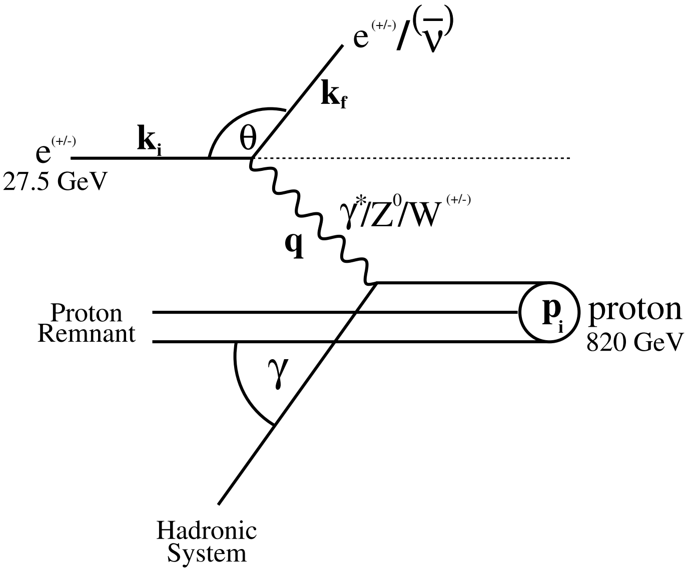

Figure 2.3: The Feynman diagram representation of deep inelastic scattering in the Quark Parton Model.

The quark parton model (or simply "parton model") proposed that the proton was a collection of non-interacting partons, at that time thought to be three valence quarks surrounded by a sea of quark anti-quark pairs. Deep inelastic scattering now becomes elastic scattering of leptons off these quarks, shown in figure 2.3. Thus, the structure functions can be considered as charged momentum distributions of the protons partonic structure, summed over all quarks flavours i, as defined in equations 2.12 and 2.13.

$$F_2(x, Q^2) = x \sum_i e_i^2 (q(x, Q^2) + \bar{q}(x, Q^2)) \tag{2.12}$$

$$xF_3(x, Q^2) = x \sum_i e_i^2 (q(x, Q^2) - \bar{q}(x, Q^2)) \tag{2.13}$$

Measurements of the structure function of protons show that the momentum sum over all x did not equal 1. Thus, there must be some other partons making up the proton which do not interact with the photon. This discrepancy was resolved by the postulation of a charge neutral spin 1 boson called the gluon. The gluon would be the force mediator for the strong force and a new "colour" charge was proposed for quarks and gluons. Direct evidence for gluons was found at DESY [17] in the form of three jet events in e^+e^- annihilation. The idea of this "improved" parton model was a proton consisting of 3 valence quarks with a sea of gluons and $q\bar{q}$ pairs.

The quarks were considered as "free" because if the proton was travelling with sufficient momentum then the interactions between quarks would be time dilated. Thus, the time period of the scatter would be less than that of any quark (anti-)quark interaction. A recent result [18] for the structure function $F_2(x, Q^2)$ is shown in figures 2.4 as a function of Q^2 for different x ranges.

2.3 QCD Improved Parton Model

In the improved parton model the proton still consisted of three valence quarks but was surrounded by a sea of gluons. These gluons can split into $q\bar{q}$ pairs, producing the sea quarks, or, because they also carried the colour charge, could split into gluon pairs.

With the inclusion of an additional colour vertex the calculable contributions for DIS, corresponding to a leading order cross section shown in figure 2.5, includes the QCD Compton (QCDC) and Boson Gluon Fusion (BGF) diagrams.

The QCD Compton event consists of the quark emitting a gluon, either before or after the photon vertex. The differential cross section with respect to the square of the transverse momentum, $p_\perp^2$, of the gluon emission contains

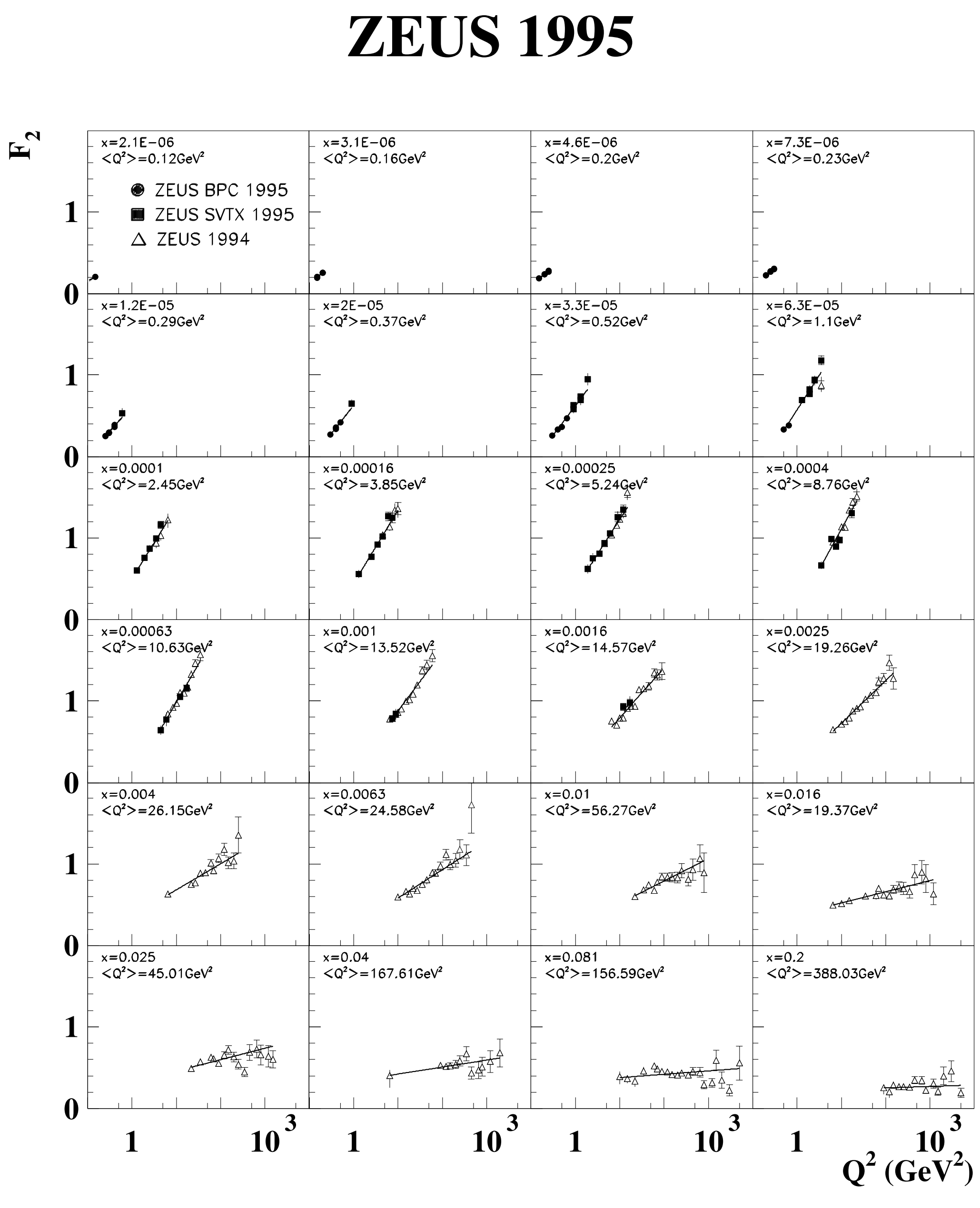

Figure 2.4: Recent results for the structure function $F_2(x, Q^2)$ as a function of Q^2 in bins of x from ZEUS 1994 and 1995 data sets.

a propagator term of the form:

$$\frac{d\sigma}{dp_{\perp}^{2}} \propto \frac{1}{p_{\perp}^{2}} P_{\mathrm{qg}} \tag{2.14}$$

where:

$$P_{\mathrm{qg}}(x) = \frac{4}{3}\frac{1+x^{2}}{1-x} \tag{2.15}$$

where x is the momentum fraction of the quark after emitting the gluon. This cross section diverges when $x = 1$ which corresponds to the emission of a soft gluon. There is also a divergence when $p_{\perp}^{2} = 0$ which corresponds to the emission of a collinear gluon. Both of these divergences come from the fact that when the invariant mass of the quark-gluon system is less than ~ 1 GeV perturbative methods are no longer applicable. Thus, these divergences all occur in the non-perturbative regime where confinement effects must be considered.

The Boson Gluon Fusion process consists of a gluon interacting with the photon via a quark or anti-quark mediator. The propagator term in the cross section, with respect to $p_{\perp}^{2}$, is given by:

$$\frac{d\sigma}{dp_{\perp}^{2}} \propto \frac{1}{p_{\perp}^{2}} P_{\mathrm{qq}} \tag{2.16}$$

where:

$$P_{\mathrm{qq}}(x) = \frac{1}{2}\left(x^{2} + (1-x)^{2}\right) \tag{2.17}$$

Here again the cross section diverges when $p_{\perp}^{2} = 0$ for similar reasons to those described above.

2.4 The Strong Coupling Constant (α_s)

As with electroweak interactions there is a coupling parameter associated with the interaction of coloured objects. This coupling strength is given the

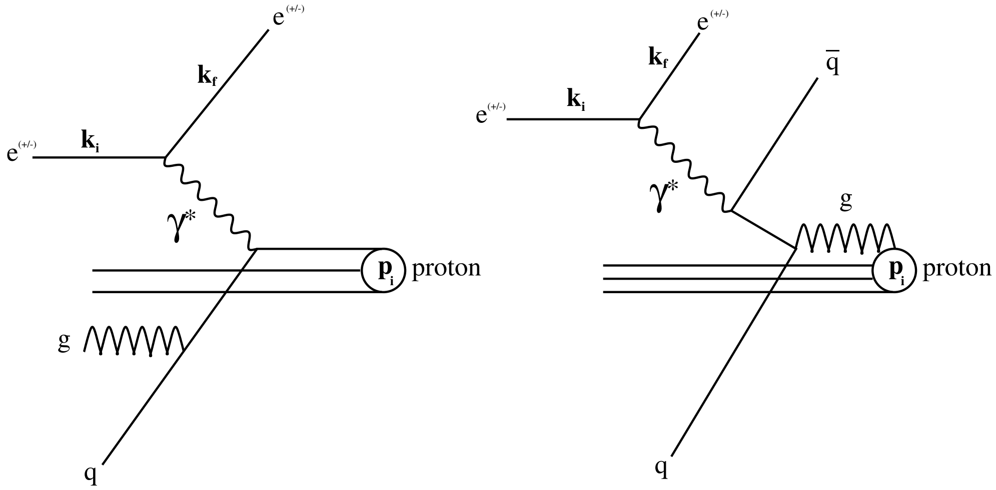

Figure 2.5: Feynman diagrams representing additional deep inelastic scattering processes for the improved Quark Parton Model. The diagram on the left is a final state QCD Compton event and the diagram on the right is a BGF event.

name α_s and, as with electroweak interactions, varies logarithmically with the energy scale of the interaction. Perturbative QCD predicts the variation of the strong coupling constant with energy; the absolute value has to be determined from experiment. At leading order the strong coupling constant is given by equation:

$$\alpha_s(Q^2) = \frac{12\pi}{(33 - 2N_f)\ln\left(Q^2/\Lambda^2\right)} \tag{2.18}$$

This includes corrections to the strong coupling constant from gluon self interactions and the production of $q\bar{q}$ pairs, which produce screening. Here N_f is the number of quark flavours and Λ is a free parameter, describing where perturbative predictions are no longer valid. Λ is determined from experiment and gives a measurement of the strong coupling constant at a given scale. The next to leading order definition for the strong coupling constant is given by:

$$\alpha_s(Q^2) = \frac{12\pi}{(33-2N_f)\ln(Q^2/\Lambda^2)}\left[1-\frac{(918-114N_f)\ln(\ln(Q^2/\Lambda^2))}{(33-2N_f)^2\ln(Q^2/\Lambda^2)}\right] \tag{2.19}$$

However, here the value of Λ is renormalisation scheme dependent. By convention a Modified Minimum Subtraction, or $\overline{MS}$, scheme is used and is the default scheme used in this work. This scheme dependence relates to how the non-logarithmic, finite, contributions to the matrix element are treated. The reader is referred to [29] for a more complete description.

As the value of α_s varies with scale it is convenient to quote the value at a specific scale, where perturbation theory is valid. For this reason the value $\alpha_s(M_Z)$ is usually quoted, with the world average being $\alpha_s(M_Z) = 0.118 \pm 0.003$ [30]. Also, the parameter Λ is often quoted along with the specific scheme used and number of active quark flavours (e.g. $\Lambda^{[4]}_{\overline{MS}}$).

2.5 Next to Leading Order Monte Carlos

In addition to the leading order corrections shown in figure 2.5 it is possible to include more vertices (or higher orders) in the calculation of cross sections. Presently DIS is calculated to Next to Leading Order (NLO) accuracy for final state observables. The inclusion of these higher orders causes further problems with divergences from collinear gluon emission and other processes. There are a number of ways of overcoming these divergence problems; one can either use phase space slicing [19, 20] or the subtraction method [21, 22, 23, 24, 25, 26] in the numeric calculation of cross sections.

To evaluate cross sections for any event observables at next to leading order accuracy Monte Carlo integration methods can be used. In the case of this analysis the NLO Monte Carlo program DISENT [27] was used. This is based on the Catani-Seymour algorithm for NLO corrections to event observables in DIS [24, 25] using the subtraction method. The program generates a number of “points” in phase space for which it calculates the contributions from leading and next-to-leading order corrections. These contributions are in the form of a partonic final state from which a user specific routine determines the particular observable in which one is interested.

It is advisable to create a large number ($\sim$ 1-10 millions) of “points” to ensure sufficiently large statistical which will give the observables numerical stability. The relevant kinematic range needs to be defined and, in addition to this, a parameterisation of the partonic structure of the proton provided. A parameterisation of the proton can be chosen from the PDFLIB [28] user routines.

2.6 The Breit Frame

The analysis of DIS is problematic in many ways, one area is finding an appropriate frame in which to perform measurements. The problem lies in the separation of the proton remnant from the hadronic final state produced by the struck quark. These two regions can be defined as the target region (proton remnant) and the current region (struck quark). The frame in which there is maximum separation, in both space and momentum, of the target and current regions is the Breit frame or “brick wall” frame.

The Breit frame is defined as that frame in which the momentum transfer from the lepton to the struck quark ($\mathbf{q}^\mu$) has only a z component (i.e. $\mathbf{q} = (0, 0, 0, Q)$). In the framework of the parton model, DIS in the Breit frame consists of the struck quark arriving and leaving with momentum $Q/2$ and $-Q/2$ respectively, all of which is in the z component of the four vector. This

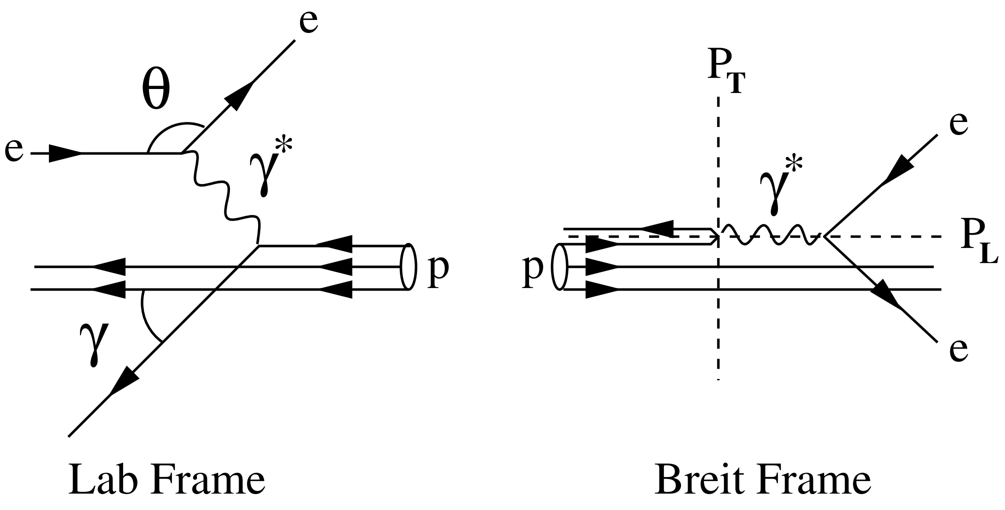

Figure 2.6: Naïve quark parton model of a DIS event in the laboratory and Breit frame.

is illustrated in Figure 2.6 which shows the laboratory and Breit frame for the same DIS event in the framework of the parton model.

It can be thought of as the incoming quark hitting a brick wall and rebounding with the same momentum. This frame is particularly useful in comparing DIS results to those of e^+e^- annihilation. The right hand hemisphere is, in the parton model, equivalent to a single hemisphere of the final state $e^+e^- \longrightarrow q\bar{q}$ at the centre of mass energy Q, so comparisons between the two results can be usefully considered.

A diagram showing the similarity between DIS in the current region of the Breit frame and e^+e^- annihilation is shown in figure 2.7. Part (a) is a space time diagram of an electron-positron annihilation event, on the left, and a DIS event in the Breit frame, on the right. One can see that the photon in the e^+e^- event is time like, which is in contrast to the DIS Breit Frame case where it is space like. This space like property in DIS can be used to define an event axis which is absent in e^+e^- events. In part (b) these events are mapped into a momentum frame. It is here that one can see the similarity between the two classes of events, both events have an outgoing quark (or anti-quark). In part (c) a diagram of available momentum space is given for each type of event. From this it can be concluded that for an e^+e^- with centre of mass energy s the equivalent DIS event would have a value of $Q/2$ equal to this.

A Lorentz boost is required to move to the Breit frame, the velocity of which is given by:

$$\vec{\beta} = \frac{\vec{q} + 2x\vec{p_i}}{q_0 + 2xp_0} \tag{2.20}$$

where $\mathbf{p} = (E_p, \vec{p})$ and $\mathbf{q} = (q_0, \vec{q})$ are the laboritory four momenta of the proton and photon respectively. The event is then rotated such that the photon aligns along the z axis and the electron is in the xz plane.

It is important to remember that when including higher orders (see section 2.5) the picture of DIS in the Breit frame becomes more complicated than the parton model description shown in figure 2.6. The inclusion of the final state QCDC process is equivalent to $e^+e^- \to q\bar{q}g$, shown in part (a) of Figure 2.8. This equivalence breaks down when considering initial state QCDC and BGF processes because the e^+e^- initial state partons are not coloured.

In both QCDC and BGF the final event topology depends on the fractional momentum taken away by the emitted parton(s) and the square of the transverse momentum of the partonic final state, as discussed in Section 2.3. The singularities discussed in the previous section occur when the fractional momentum of the emitted parton is zero (soft emission) or when the square of the transverse momentum if zero (collinear emission).

Part (a) of Figure 2.8 shows the final state QCDC process which will be driven by soft and collinear parts of the cross section. In parts (b) and (c)

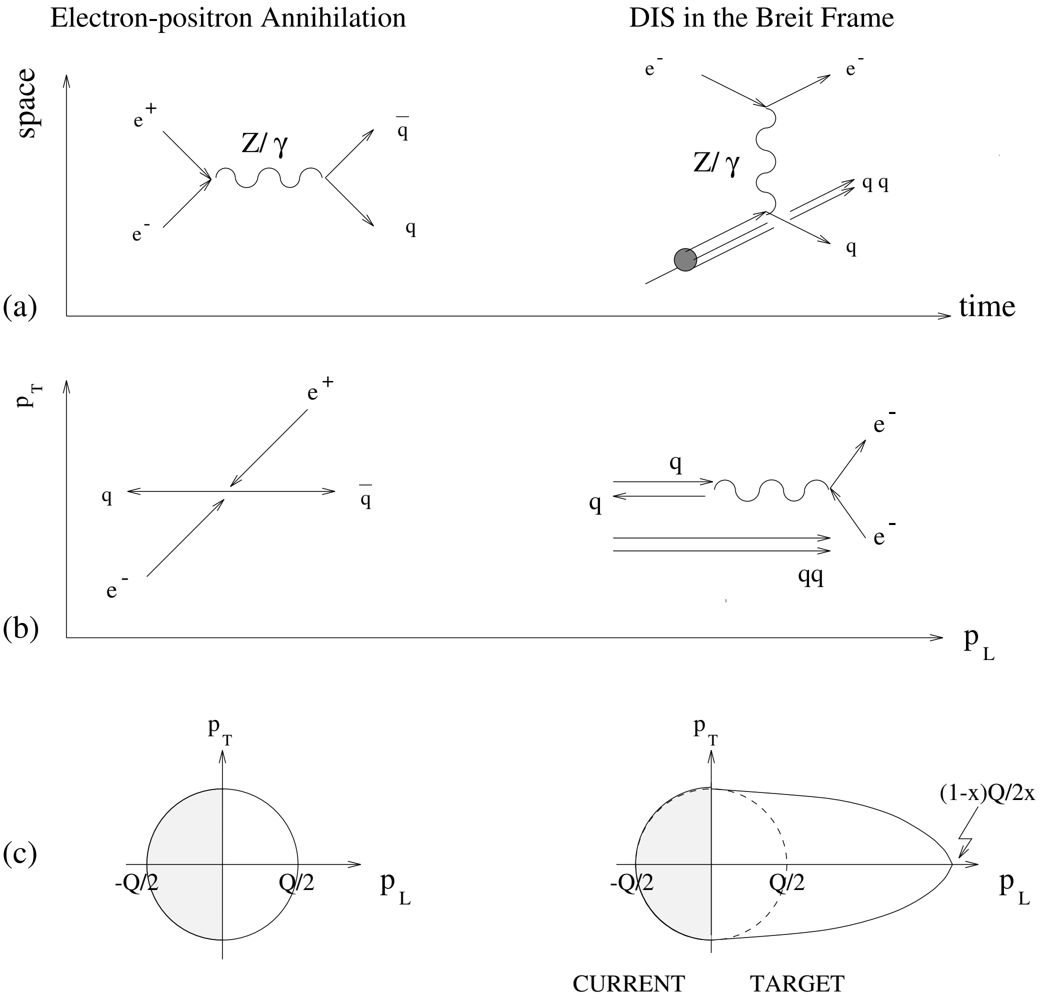

Figure 2.7: A comparison between $e^+e^- \rightarrow q\bar{q}$ events the current region of the Breit frame for DIS events.

of Figure 2.8 the soft and collinear cases of initial state QCDC are shown. In the soft case the gluon is preferentially emitted into the current region. However, for collinear emission the gluon is preferentially emitted into the target region. In part (d) of Figure 2.8 the BGF process has both partons being preferentially emitted into the target region due to the collinear divergence dominating the cross section. The BGF process is the most important difference between DIS and $e^+e^- \to q\bar{q}$.

2.7 Event Shape Variables

The analysis of event shape variables is a complementary method in determining the strong coupling constant, α_s, to that from jet rates [31]. The event shape measurements have been dependent on the hadronisation model used to correct the data back to the parton level. The correction was usually carried out using a Monte Carlo event generator which included it's own model dependent hadronisation correction (see section 4.2 and 4.3). This introduces systematic uncertainty into the evaluation of α_s.

Earlier measurements have analysed $e^+e^- \longrightarrow q\bar{q}$ annihilation events. These measurements have a number of disadvantages over those made using deep inelastic scattering. Firstly in e^+e^- annihilation the virtual photon is time-like and thus has no defined natural space-like axis, so one has to be found using iterative methods. This is in contrast to the space-like virtual photons of deep inelastic scattering which defines the event axis completely. Also the e^+e^- experiments can only gather data at or around a single centre of mass energy [32, 33]. However, with deep inelastic scattering the value of Q can range from zero to 150 GeV which is important when studying the event shapes dependence on centre of mass energy.

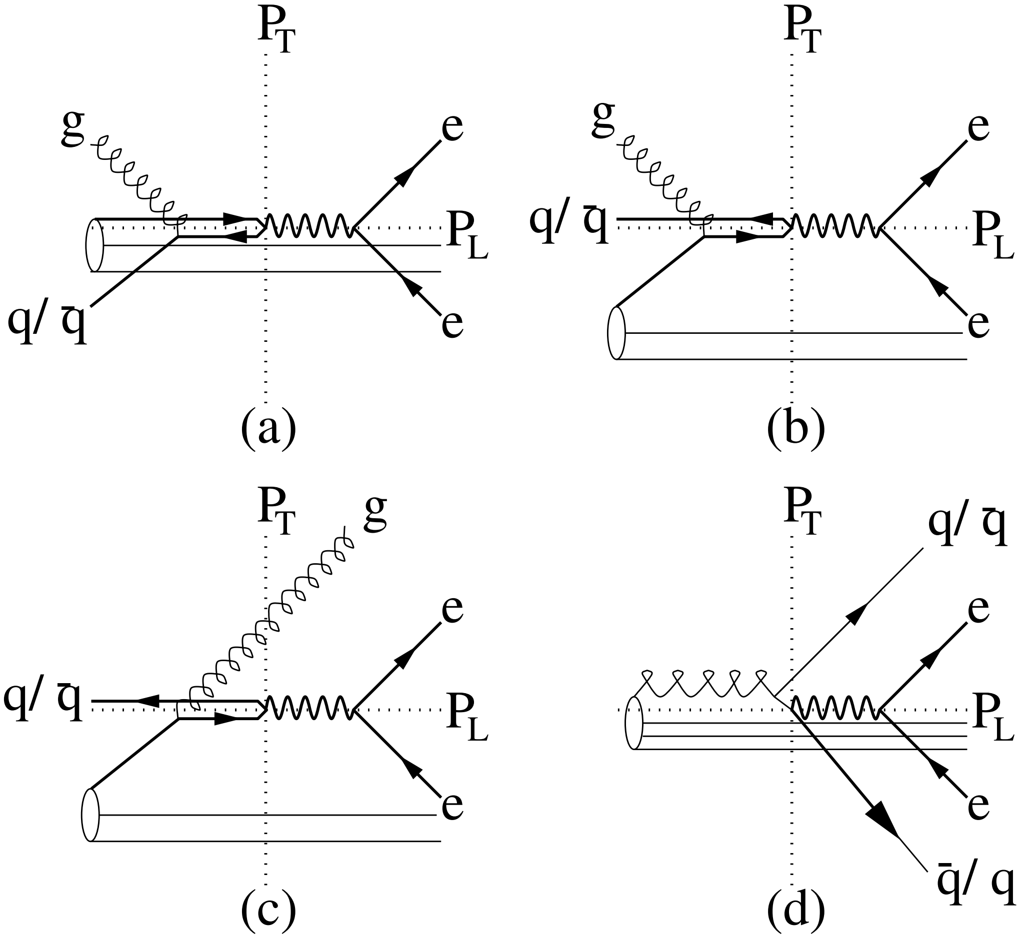

Figure 2.8: Feynman diagrams of leading order DIS processes in the Breit frame. (a) final state QCDC, (b) initial state QCDC with soft gluon emission, (c) initial state QCDC with collinear gluon emission, and (d) BGF process.

The event shape variables that will be presented in this thesis are thrust (T_z), jet broadening (B_c), invariant jet mass (ρ_E) and the C parameter (C_E). The definitions of these variables are given in equations 2.21 to 2.24. Here the particle's momentum 3-vector is given by $\vec{p}$, the momentum 4-vector by p^μ and $\vec{n}$ is a unit 3-vector aligned along the negative z axis (i.e. defined by the virtual photon 4-vector). In these expressions the sum i runs over all charged hadrons originating from the primary vertex in the current region of the Breit Frame.

$$T_z = \frac{\sum_i |\vec{p}.\vec{n}|}{\sum_i |\vec{p}|} = \frac{\sum_i p_z}{\sum_i |\vec{p}|}, \tag{2.21}$$

$$B_c = \frac{\sum_i |\vec{p} \times \vec{n}|}{\sum_i |\vec{p}|} = \frac{\sum_i p_\perp}{\sum_i |\vec{p}|}, \tag{2.22}$$

The variables T_z and B_c measure the longitudinal and transverse development of the hadronic system, produced by the struck quark, with respect to the photon axis.

$$\rho_E = \frac{\left(\sum_i \mathbf{p_i}\right)^2}{\left(2\sum_i E\right)^2} \tag{2.23}$$

$$C_E = 3\left(\lambda_1\lambda 2 + \lambda_2\lambda_3 + \lambda_3\lambda_1\right) \tag{2.24}$$

Here the variables λ_1, λ_2 and λ_3 are the eigenvalues for the linearised momentum tensor, given in equation 2.25.

$$\Theta^{\alpha\beta} = \frac{\sum_i \vec{p_i}^{\alpha}\vec{p_i}^{\beta} / |\vec{p_i}|}{\sum_j |\vec{p_j}|} \tag{2.25}$$

The variables ρ_E and C_E evaluate the invariant mass and relative $k_\perp$ of the hadrons. They do not depend on the photon axis and thus provide orthogonal information to that from T_z and B_c. A diagram showing the various configurations of two particles and their relation to the maxima and minima for all the event shape variables is shown in figure 2.9. For zeroth order the event shape variables have the value 0, except for thrust which is 1; thrust is therefore sometimes quoted as $(1 - T_z)$ so it also has the value

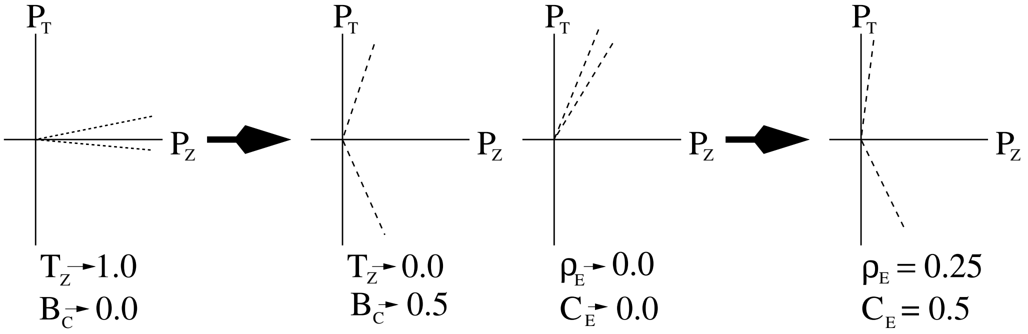

Figure 2.9: Diagrammatical representation of the event shape variables T_z, B_c, ρ_E and C_E for various two particle (shown as a dashed line) configurations.

0 at zeroth order. As particles are added to the event shape variable cross sections the variables all increase from zero (using $(1 - T_z)$ in place of (T_z)) to some finite value.

It is possible, particularly when measuring charged hadrons, that the current region of the Breit frame is void of hadronic activity. A question must be raised regarding the value of the event shape variables in this case. Do we look at the limit definitions represented in figure 2.9 and say, for example, thrust is zero and jet broadening is 0.5? One way to combat this is to require a percentage of the value of Q to be present as hadronic energy in the current region. This aspect of the analysis will be discussed in more detail in section 3.3.

The work presented in this thesis will concentrate mainly on the mean value of an event shape variable as a function of mean Q ($\langle Q \rangle$); the differential distributions are also measured. The theoretical interest, discussed in section 2.8, is currently centred on the mean values but additional work on the differential distributions exists [32].

2.8 Power Corrections

The calculation of DIS cross sections to an arbitrary order can be useful to experimentalists. However, when investigating deep inelastic scattering in the current region of the Breit frame, the detector measures hadrons. There is a fundamental step from the partonic world to the hadronic world, made difficult by the inapplicability of perturbative methods to scales below $\simeq 1$ GeV.

The estimation of these non-perturbative effects for the mean and differential event shape distributions has been the subject of much theoretical interest recently. Some time ago it was noticed that corrections from the NLO result to the measured distributions had a general $1/Q$ form, but the exact form was variable dependent. Work involving an infrared effective strong coupling [34], introduced below some scale, produced a $1/Q$ power correction which was variable specific.

This theory can be summarised in two equations. The first states that the hadron level mean event shape variable (here $\langle F \rangle$ is used to denote an arbitrary event shape variable) is a sum of the NLO result plus a generalised power correction:

$$\langle F \rangle = \langle F \rangle_{NLO} + \langle F \rangle_{pow} \tag{2.26}$$

The second equation defines the generalised power correction as:

$$\langle F \rangle_{pow} = a_F \frac{A_1}{Q} \tag{2.27}$$

which gives a $1/Q$ dependence with a normalisation factor, a_F, which is calculable for each event shape variable. The term A_1 is given by:

$$A_1 = \frac{C_F}{\pi} \mu_I \log^p \left(\frac{Q}{Q_0} \right) \left[\overline{\alpha_0} - \alpha_s(Q) - \frac{\beta_0}{2\pi} \left(\log \left(\frac{Q}{\mu_I} \right) + \frac{K}{\beta_0} + 1 \right) \alpha_s^2(Q) \right] \tag{2.28}$$

Where $\beta_0 = 11 - \frac{2}{3}N_f$, $K = \frac{67}{6} - \frac{\pi^2}{2} - \frac{5}{9}N_f$ and N_f is the number of active quark flavours at the scale μ_I, usually taken to be 3.

Equation 2.28 introduces a new phenomenological constant, $\overline{\alpha_0}$, which is postulated to be a universal (i.e. the same for all event shape variables for all processes) hadronisation constant. This phenomenological constant $\overline{\alpha_0}$ is defined as the first moment of the effective strong coupling below the scale μ_I and is given by:

$$\overline{\alpha_0}(\mu_I) = \frac{1}{\mu_I}\int_0^{\mu_I} \alpha_{\text{eff}}(\mu^2)d\mu \tag{2.29}$$

and is thus the average value of the effective coupling below the matching scale μ_I. The variable μ_I is the matching scale for where the effective strong coupling constant is valid, usually taken to be 2 GeV. The power correction should be insensitive to the value take for μ_I.

Equation 2.28 also contains $\log(Q/\mu_I)$ and $\log^p(Q/Q_0)$ terms. The second log term contains a Q_0 term which is an unknown scale taken to be equal to, or about, μ_I. This logarithmic term is also to the power p, which is also dependent on the variable. A table detailing the variable specific normalisation constants, a_F, and the logarithmic power factor, p, is shown in 2.1. Some ambiguity still remains in the calculation of the C_E normalisation factor so the range of possible values are given, also the value of p for B_c is still under consideration[1].

2.8.1 Milan Factor

Further work [35, 36] on these universal power corrections has produced a further addition to the theory. The inclusion of the two loop calculation to the power correction have indicated that the normalisation factors, a_F, need to be multiplied by a new factor. This factor is called the "Milan Factor",

---

[1] See Y.Dokshitzer's talk ICHEP98

Parameter	$\langle T_z \rangle$	$\langle B_c \rangle$	$\langle \rho_E \rangle$	$\langle C_E \rangle$
a_F	1.0	0.5	0.5	$3\pi/2$ - $6\pi/2$
p	0	0 or 1	0	0

Table 2.1: Table of variable dependent normalisation factors (a_F) and logarithmic power factor (p) for the power corrections to next to leading order predictions.

represented by the symbol $\mathcal{M}$, and has a value of 1.8 for 3 active flavours of quarks. However, in addition to this factor a new definition of $\overline{\alpha_0}$ is proposed.

$$\overline{\alpha_0}(\mu_I) = \frac{1}{\mu_I} \int_0^{\mu_I} \alpha_{\mathrm{s}}(\mu^2) d\mu \tag{2.30}$$

where it is not the first moment of an effective coupling but the first moment of the strong coupling. The redefinition of $\overline{\alpha_0}$ produces an additional $2/\pi$ term entering in the right hand side of Equation 2.27 which now becomes:

$$\langle F \rangle_{pow} = a_F \frac{2\mathcal{M}}{\pi} \frac{\mathcal{A}_1}{Q} \tag{2.31}$$

The change of the term A_1 to $\mathcal{A}_1$ is to denote the difference in the definition of $\overline{\alpha_0}$.

The inclusion of the two loop correction also resolves the ambiguity in the value of a_F for the C parameter. The value is now thought to be $3\pi/2$. However, problems involving recoil terms have plagued the calculation of the two loop terms for jet broadening. For the purposes of this thesis the one loop a_F term will be used with the Milan Factor and results for any fits be taken accordingly.

In summary the NLO contribution for a mean event shape is dependent on the scale Q and α_s, while the power correction is dependent on the scale, α_s and $\overline{\alpha_0}$. Thus, a measurement of the mean event shape variable distributions, as a function of mean Q, can be fitted to this functional form to obtain a measurement of both of these important parameters.

Chapter 3

Data Analysis

In this chapter the various methods of kinematic reconstruction are explained. The areas of phase space where the various methods are most accurate are described. From this starting point selection criteria are discussed which secure a reasonably pure sample of DIS events for analysis. The procedure of boosting a DIS event to the Breit frame, using the best understood method of kinematic reconstruction, is presented.

A cut that ensures a well defined value for the event shape variables, based on the energy in the current region, is described and the magnitude of this cut evaluated.

3.1 Kinematic Reconstruction

The deep inelastic scattering kinematics covered in section 2.1 are a appropriate place to start the discussion of the experimental techniques involved in analysing DIS events observed in a detector. An experimentalist cannot observe the exchanged photon or struck quark directly but must infer the kinematics from other observables. Three methods to determine the kinematic variables will be presented and their relative benefits outlined. These three methods use different observable quantities to evaluate the kinematics and are called the “electron method” (denoted by variables with subscript e), the “Jacquet-Blondel method” (denoted by variables with subscript JB) and the “Double Angle method” (denoted by variables with subscript DA).

3.1.1 The Electron Method

The simplest method to determine the event kinematics is the “electron method”. Recall equation 2.4, in which the variable Q^2 is defined as the negative four momentum squared of the exchanged photon, then if the electron is scattered with energy E'_e and angle θ_e (measured with respect to the proton direction) one can determine:

$$Q^2_e = 2E_eE'_e(1 + \cos(\theta_e)) \tag{3.1}$$

and also from equation 2.6 one can deduce:

$$y_e = 1 - \frac{E'_e}{2E_e}(1 - \cos(\theta_e)) \tag{3.2}$$

and finally, using equation 2.8, the Bjorken scaling variable can be written:

$$x_e = \frac{E'_e}{2y_eE_p}(1 + \cos(\theta_e)) \tag{3.3}$$

The measurement of the kinematic variables using the electron method relies upon the understanding of the energy resolution of the electromagnetic calorimeter. The kinematic resolution is poor when the scattered electron energy is $\simeq E_e$, or when $y_e \ll 0.1$. However, when the scattered electron energy is greatly different to the incoming electron energy then the resolution is relatively good, this relates to the relatively high y_e region.

3.1.2 The Jacquet-Blondel Method

The “Jacquet-Blondel method” is most useful when the scattered electron is not detected at all, such as photoproduction events where Q^2 is zero and the electron escapes down the beampipe, or charged current events. The calculation relies solely on the measurement of the hadronic final state, X. The assumption which justifies this approach is that the net transverse momentum, carried away by any hadronic activity not detected, is small. This is a valid assumption because the detector has almost 4π solid angle coverage and the only gaps are those to accommodate the beampipe, thus the transverse energy of particles lost through these holes will be relatively small.

With this assumption one can write :

$$Q^2_{JB} = \frac{\sqrt{\left(\sum_h p^2_{\perp}\right)^2}}{1 - y_{JB}} \tag{3.4}$$

where the sum is over all hadronic activity in the calorimeter and :

$$y_{JB} = \frac{\sum_h (E - p_z)}{2E_e} \tag{3.5}$$

However, this approach is prone to large uncertainties due to the resolution on the hadronic energy scale. This said the resolution on y_{JB} at low values (around 0.04) is better understood than the other methods.

3.1.3 The Double Angle Method

The final reconstruction method is the “Double Angle method” which includes both information from the scattered electron and hadronic final state, specifically the scattered electron angle and an angle γ_h associated with the hadronic final state. In the naïve parton model the angle γ_h is the angle through which the quark is scattered. The kinematic variables are given by:

$$Q^2_{DA} = 4E^2_e \frac{\sin(\gamma_h)\,(1 + \cos(\theta_e))}{\sin(\gamma_h) + \sin(\theta_e) - \sin(\gamma_h - \theta_e)} \tag{3.6}$$

and:

$$y_{DA} = \frac{\sin(\theta_e)\,(1-\cos(\gamma_h))}{\sin(\gamma_h)+\sin(\theta_e)-\sin(\gamma_h-\theta_e)} \tag{3.7}$$

This method has a better resolution than the others because the electron scattering angle is well measured and the variable γ_h is calculated using the equation:

$$\cos(\gamma_h) = \frac{\sqrt{\left(\sum_h p_\perp\right)^2} - \left(\sum_h (E-p_z)^2\right)}{\sqrt{\left(\sum_h p_\perp\right)^2} + \left(\sum_h (E-p_z)^2\right)} \tag{3.8}$$

which is dependent on a ratio of hadronic energies, thus, mostly insensitive to the uncertainty in the absolute scale. This method generally gives the best resolution over the whole kinematic range when there is an identified electron in the detector.

The “Double Angle method” is used to determine the kinematics for the analysis presented in this thesis. This is because of the better understanding of this variable in Monte Carlo studies. This method relies on the geometry of an event being correctly simulated. There is some energy flow model uncertainty but this is partially cancelled by the method being based on a ratio of energies.

However, the other two methods are used to reject photoproduction background, to ensure that the deep inelastic scattering event is in a region of phase space where QED radiative corrections are small and to ensure the event is in a kinematic region where the “Double Angle method” is well understood in the MC.

3.2 Electron Finding

The identification of scattered electrons in the ZEUS detector is central to any analysis of DIS events. This task can be performed by various electron finders, each of which perform the task using different information. The electron finder used in the selection of events for the analysis presented in this thesis is a neural network called SINISTRA95 [16].

The neural network uses information from the calorimeter to distinguish electromagnetic from hadronic activity. The neural network was trained on Monte Carlo events to optimise the weights and cuts applied to this calorimeter information.

An algorithm is applied to all electromagnetic calorimeter deposits to reduce the individual cells to clusters, called "islands". A probability of this island coming from an electron is then calculated. These candidates are then ordered in decreasing probability. For this analysis only events with an electron candidate with a probability greater than 0.9 are taken.

3.3 Data Analysis

Once the event kinematics have been reconstructed the selection and analysis of the data can be appreciated. The primary goal is to obtain a reasonably pure sample of DIS events and to exclude events that, for one reason or another, are poorly reconstructed. After this has been accomplished the remaining events can then be selected on the basis of the kinematic quantities. This will ensure that any background processes contaminating the sample, such as photoproduction, will be suppressed.

3.3.1 Data Selection

Data which has been selected by the ZEUS third level trigger is stored and later passes through the off line reconstruction code. This process produces Data Summary Tapes (DSTs) of individual reference numbers (or "bits"), which relate to a certain set of strict filters, associated with each event. This eases the procedure of data analysis because a DST "bit" can be chosen and only data passing these specific filters will be analysed. For the 1995, 1996 and 1997 analysis DST bit 18 was used to filter the data. An outline of the selection cuts are as follows.

- $|x_e|$ and $|y_e|$ position in calorimeter < 16 cm,

This ensure that the scattered electron is in a reasonably well understood area of the detector, with respect to the Monte Carlo simulation. Scattered electrons with either x or y positions smaller than 16 cm undergo energy loss from dead material which is not sufficiently modelled in the detector simulation.

- $E'_e > 10$ GeV,

The neural network used to identify electrons scattered into the calorimeter is 95% efficient for electrons with an energy greater than 10 GeV. The purity of this sample is greater than 90% for the lowest Q^2 region and improves with increasing Q^2.

- 35 GeV $< \sum_{\mathrm{Total}}(E - P_z) <$ 60 GeV,

If the electron in a DIS event undergoes a large amount of energy loss from Initial State Radiation (ISR) then the kinematics of the event change greatly. The upper cut on total $(E - P_z)$ excludes the number of ISR events with large radiation. In addition, selection of photoproduction events where the electron escapes down the beam pipe undetected and a π^0 is mistaken for an electron will be excluded by the lower cut.

- $y_{JB} > 0.04$,

When the hadronic activity in the calorimeter is low the noise coming from decays of the U^{235} can distort the measurement of kinematic variables. Events were therefore required to have a value of $y_{\rm JB}$, the method with best resolution in this region, greater than 0.04.

- number of vertex tracks > 1,

For tracking measurements to be made the event must contain at least one track with:

- $|z_{vtx}| < 60$ cm,

Upstream beam gas events and cosmic muon events are suppressed by the inclusion of an event vertex cut. Also, non-uniformity of the field inside the CTD causes problems in track finding when the event vertex is too far from the nominal interaction point. These problems are circumvented by an event z vertex cut of 60 cm.

- $y_e < 0.95$.

As with the $\sum_{Total}(E - p_z)$ selection criteria the requirement for $y_e < 0.95$ will reduce the number of photoproduction events with a π^0 mistaken as an electron. This is only important at high Q^2 because at low Q^2 the electron energy cut of 10 GeV corresponds to a y_e cut of around 0.7.

Additional algorithms were applied which discard QED Compton, halo muon and cosmic muon events. Other selection criteria ensuring optimal detector operation (e.g. operational magnets, no sparks in calorimeter cells, correct gas mixtures and operational triggers) were also included in a global ZEUS routine called EvTake.

Once a relatively pure sample of deep inelastic scattering events has been obtained the events are be subdivided into various kinematic ranges. Once the data is separated into defined Q^2 regions the mean values for each range can be calculated. Following correction these mean values can then be used in a multi-parameter fit using the power corrections described in Section 2.8. It may also be desirable to examine the x dependence of the event shape variables. If one recalls section 2.8 the only x dependence that occurs in the mean, and differential, event shape variables will come purely from this next to leading order matrix element. The power correction term, $\langle F\rangle_{pow}$, should have no x dependence. Investigation of the validity of this will yield a good systematic test of theory.

From previous work on hadronic final states in the current region of the Breit frame [37], also carried out using tracks, a suitable set of kinematic bins have been determined and extended in order to incorporate the highest Q^2 data. These ranges are consistent with the resolutions in the kinematics variables and produce good acceptances for tracks in the current region of the Breit frame. A list of the different kinematic ranges and the number of events in each bin for each year's data is shown in Table 3.1.

3.3.2 Track Selection

The measurement of event shape variables presented in this thesis is determined using tracks measured by the CTD. Additional selection criteria need to be applied to ensure accurate measurement of tracks. Low momentum particles curve around within the CTD to form a tight helix. When this happens there may be problems with track finding, and thus lower efficiency which is not modelled completely in the Monte Carlo simulation. To avoid this problem a lower limit of 200 MeV is applied to the transverse momentum of any track found.

In addition to this problem, the magnetic field encompassing the tracking

Bin	x range	Q^2 Range	Events (Luminosity pb^{-1})			
#			1995	1996	1997	Total
			(6.66)	(10.71)	(26.55)	(43.92)
1	0.6-1.2 10^{-3}	10-20	45241			45241
2	1.2-2.4 10^{-3}	“	37851			37851
3	“	20-40	28261			28261
4	2.4-10.0 10^{-3}	“	31889			31889
5	1.2-2.4 10^{-3}	40-80	13981			13981
6	2.4-10.0 10^{-3}	“	27112			27112
7	“	80-160	13494	22943	59086	95523
8	1.0-5.0 10^{-2}	“	7511	11801	30457	49769
9	2.4-10.0 10^{-3}	160-320	3943	6624	16925	27492
10	1.0-5.0 10^{-2}	“	5767	9647	24899	40313
11	“	320-640	2484	4349	11494	18327
12	“	640-1280	969	1718	4493	7180
13	0.025-0.15	1280-2560	434	734	2101	3269
14	0.05-0.25	2560-5120	151	254	662	1067
15	0.06-0.4	5120-10240	51	82	212	345
16	0.1-0.6	10240-20480	13	15	40	68
17	0.2-0.8	20480-40960	1	1	3	5
Total	0.0006-0.8	10-40960	219143	58168	150372	427683

Table 3.1: Table of nominal kinematic ranges to be used in the analysis of event shape variables and the corresponding number of selected events for each year's data.

detectors has slight non-uniformity at the edges of the active tracking volume. Tracks traversing this area of non-uniformity have reconstruction problems associated with them. To reduce this problem all tracks must satisfy $|\eta| < 1.75$, where η is given by:

$$\eta = -\ln\left(\tan\left(\frac{\theta_{track}}{2}\right)\right) \tag{3.9}$$

This cut also ensures that the tracks are constructed with sufficient hits in several superlayers. A minimum requirement is hits in the first and third superlayer. The inner tracking detector reconstruction package, VCTRAK [15],supplied two tables of fitted tracks. The first table consists of all tracks that pass the above cuts. The second table is a subset of the first but with the additional constraint that the tracks have been fitted to a common event vertex. This second table was used to calculate the event shape variables from the data. This excludes tracks formed by secondary interactions with the beam pipe or decay products from long-lived hadrons (i.e. Weak decays).

3.4 Boosting To The Breit Frame

In order to perform a boost to the Breit frame, recall equation 2.20, where the photon four vector is needed. The double angle method gives the best resolution for the kinematic variables over the whole range and can be used to recalculate the scattered positron energy using equation 3.10.

$$E'_{DA} = \frac{Q^2_{DA}}{2E_e(1+\cos(\theta_e))} \tag{3.10}$$

All tracks passing the selection criteria discussed in section 3.3.2 are boosted to the Breit frame and those with negative p_z (i.e. in the current region of the Breit frame) are used to calculate the event shape variables. The pion mass is assumed for each track, which is the only assumption that can be made as no particle identification is performed.

3.5 Current Region Energy Cut

In section 2.7 it was noted that if the current region of the Breit frame was void of hadronic activity, which in this analysis corresponds to no tracks, then the event shape variables were undefined. This was remedied by the inclusion of a cut dependent on the energy measured in the current region. This will discard events which have a measured current region energy of less than $n\%$ of Q. A determination of n must be undertaken with the motivation that the statistical sample of the data must not be greatly reduced.

The 1995 data sample was used to determine the value of n. The mean value of thrust (T_z), for each of the kinematic ranges, was calculated for values of n ranging from 0 to 10%. When the cut was 0% events with zero tracks in the current region were not included in the calculation of the mean. The results are shown in figure 3.1. Most of the plots in the thesis are of this form; the x and Q^2 ranges are shown on the bottom and right of each graph respectively. Along the horizontal axis of the graphs is the percentage cut (n) while the vertical axis is mean thrust calculated for that energy cut $(\langle T_z \rangle_{Ecut})$ normalised to the mean thrust for no energy cut $(\langle T_z \rangle_{0\%})$.

The figure clearly shows that a value of $n \sim 2 - 3\%$ does not change the mean value greatly. However, if one looks at the number of events which the energy cut excludes it can be seen that an energy cut above 3-4% starts to impinge on the sample. With this in mind a energy cut of 3% was used which was also applied to both the reconstructed and hadron level Monte Carlo events (see chapter 4). Additional problems occur when considering the energy cut applied to the parton level calculation performed for this analysis. This is discussed in section 6.2.

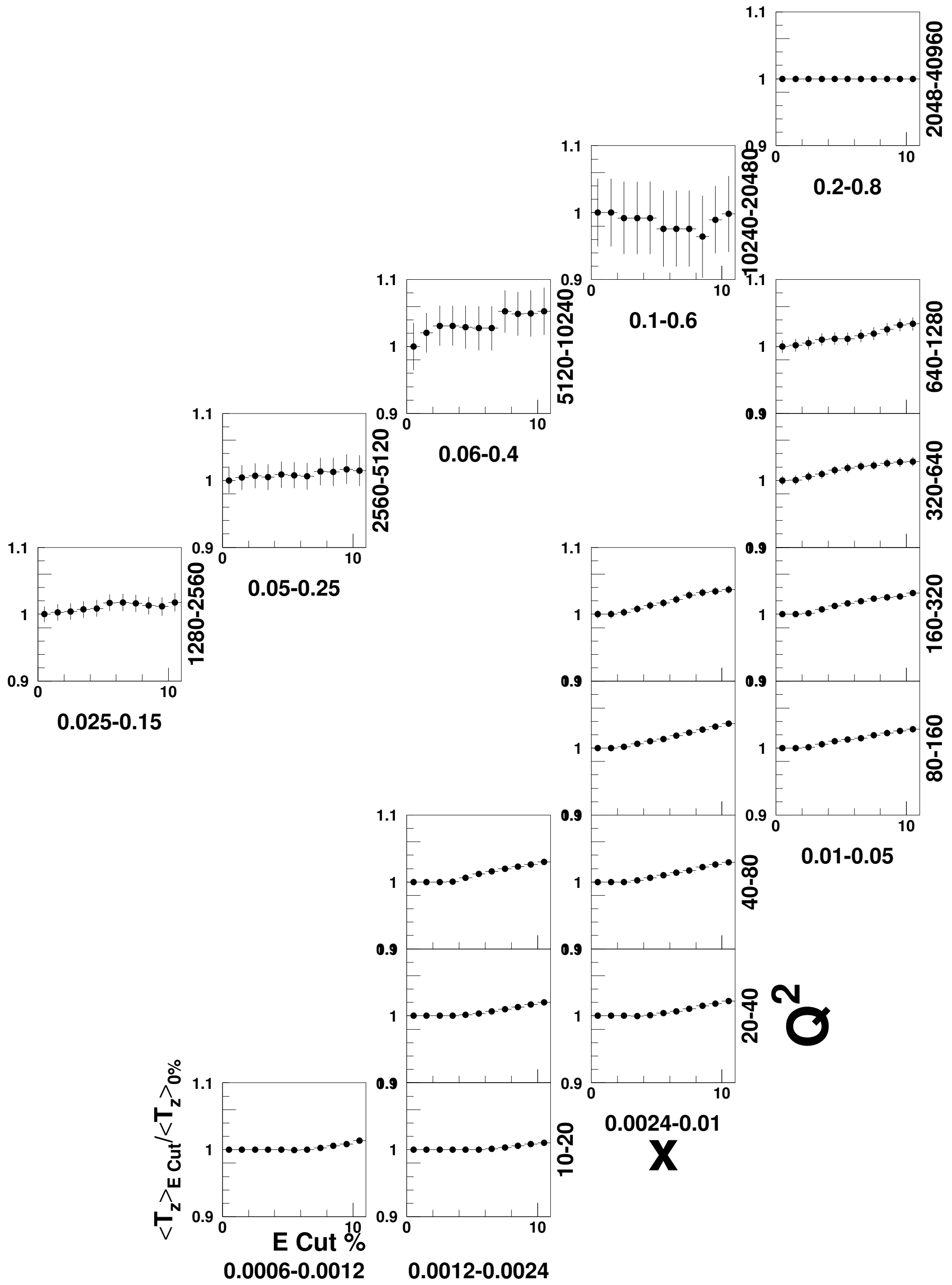

Figure 3.1: Ratio of reconstructed mean thrust ($\langle T_z \rangle$) for a specific energy cut divided by the mean thrust for no energy cut as a function of the percentage energy cut.

Chapter 4

Monte Carlo Simulation

This chapter deals with the Monte Carlo method essential for a modern particle physics analysis. A brief introduction to the motivation for such models is discussed. The main components of a Monte Carlo event generator are described and their function discussed. The methods of detector simulation are outlined. Two Monte Carlo event generators, used in the work presented in this thesis, are described.

Work carried out for the Future Physics at HERA Workshop [39] in determining a better reproduction of data from one of these models, ARIADNE, is explained and results presented.

4.1 Introduction

The extraction of physical quantities and distributions from detector data relies on the collision process as well as the detector response being well understood. The number of biasing effects and resolution parameters that need to be taken into account when measuring, even the simplest, observables preclude the evaluation of the effect analytically so that the calculation of this response function must be performed numerically.

Firstly a Monte Carlo (MC) model, based on the relevant physical theory, is needed to simulate basic topological and kinematic properties of the physics under study. Secondly, a MC model of the detector response is needed to evaluate the acceptance of a specific processes and determine the accuracy with which one is measuring physical quantities.

The combined response of these two distinct models is used to enhance certain physical processes by the evaluation of selection criteria applied to observable quantities. They are also used for studies of the resolution of measurable quantities.

For $e^{\pm}p$ scattering the simulation of an interaction consists of 3 parts:

- calculation of the distribution in phase space of different hard scattering sub-processes using perturbative QCD.

This is presently calculated to order α_s^2 but MC event generators which include a hadronisation stage only implement the order α_s result. This is dependent on the incoming energies and the structure of the proton, defined by a Parton Density Function (PDF). A randomly chosen, probability weighted, hard scattering event is then passed to a QCD cascade model.

- Calculation of further partonic emissions using a cascade model.

To determine further parton production at higher orders either a DGLAP evolution algorithm, based on the splitting functions defined in Section 2.3, or dipole formalism, employed by ARIADNE, is used.

- Confinement based models are applied to the partonic final state to produce hadrons.

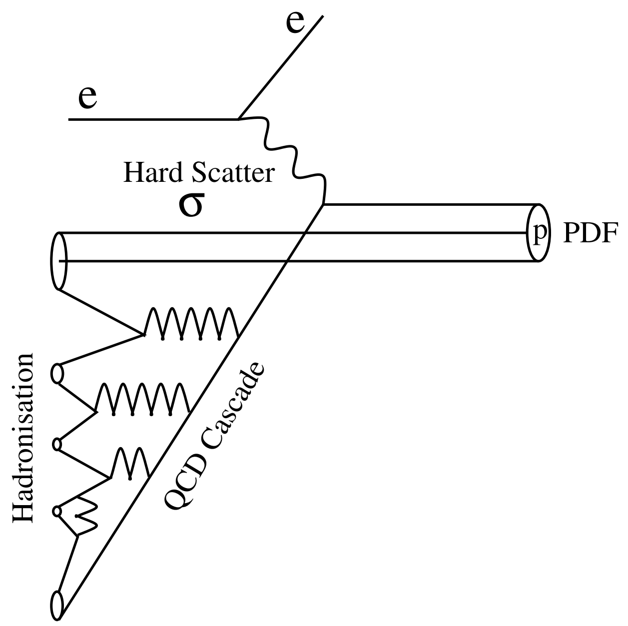

Figure 4.1: Representation of the three phases of Monte Carlo deep inelastic scattering simulation.

The final partonic system is then passed to a hadronisation model which determines how confinement is achieved and the subsequent decays of particles assessed. This three stage process is represented in figure 4.1.

The output hadrons from the hadronisation model are the particle four vectors. This data can then be passed to a detector simulation, which simulates the response of the detector. This procedure then allows the comparison of 'true' events and 'detected' events to produce the acceptance corrections and determines the selection criteria as mentioned previously.

4.2 The ARIADNE Event Generator

The ARIADNE program only simulates the QCD Cascade process using a Colour Dipole Model (CDM); therefore it needs to be interfaced to other programs which simulate the hard scatter process and the hadronisation process. The MC generators used for the calculation of the hard scatter process are either LEPTO [40] or PYTHIA [41, 42, 43]. LEPTO uses the full lepton-quark electroweak cross sections calculated to leading order. The hadronisation and decays are modelled using the JETSET [42, 43, 44] MC which uses the Lund string model.

The CDM was initially developed to simulate $q\bar{q}$ production from e^+e^- collisions, then further developed to include DIS. For an explanation of the theoretical approach it is preferable to look at $q\bar{q}$ production in e^+e^- collisions first; then proceed onto DIS.

The basic concept of the CDM is that gluons are emitted from the colour dipole between the $q\bar{q}$, and to a good approximation secondary softer gluon emission can be treated as radiation from a $g\bar{q}$ or gq dipole. This is in contrast to previous models where each parton was considered as an individual gluon emitter. Further sub-division of the colour dipoles continues to a fixed scale, which is a parameter of the model which must be tuned.

The starting point of QCD cascade models are the corresponding Matrix Elements (ME) of gluon emission from $e^+e^= \rightarrow q\bar{q} \rightarrow q\bar{q}g$, analogous to the splitting function in DIS covered in Section 2.3, which are given by:

$$\frac{d\sigma_{q\bar{q}}}{dx_1 dx_3} = \frac{2\alpha_s}{3\pi}\frac{x_1^2 + x_3^2}{(1-x_1)(1-x_3)} \tag{4.1}$$

$$\frac{d\sigma_{qg}}{dx_1 dx_3} = \frac{3\alpha_s}{4\pi}\frac{x_1^3 + x_3^2}{(1-x_1)(1-x_3)} \tag{4.2}$$

$$\frac{d\sigma_{gg}}{dx_1 dx_3} = \frac{3\alpha_s}{4\pi}\frac{x_1^3 + x_3^3}{(1-x_1)(1-x_3)} \tag{4.3}$$

The cross section for each of these processes can be calculated from the relevant Feynman diagram (figures 4.2 to 4.4), and are given in equation 4.1

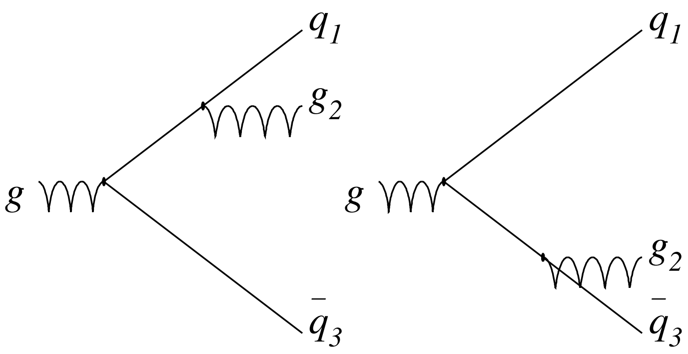

Figure 4.2: Feynman diagrams for $qq \longrightarrow qqg$

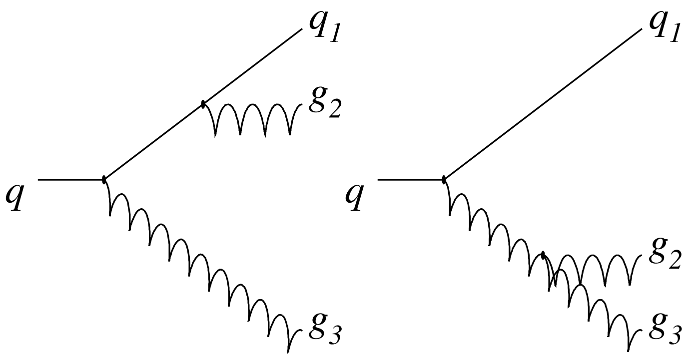

Figure 4.3: Feynman diagrams for $qg \longrightarrow qgg$

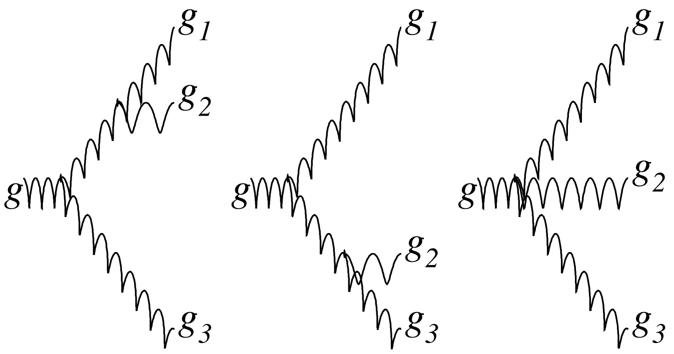

Figure 4.4: Feynman diagrams for $gg \longrightarrow ggg$

to 4.3. Here x_i is the final state energy fraction of parton i in the dipole centre of mass system, $\sqrt{S_{dip}}$:

$$x_i = \frac{2E_i}{\sqrt{S_{dip}}} \tag{4.4}$$

The value for α_s runs with the scale taken to be the $p_\perp^2$ of the emission.

When transforming the cross section in terms of $p_\perp^2$ and y, with y corresponding to the rapidity of the emitted gluon (equation 4.5), all three cross sections, with slight differences in colour factors, simplify to equation 4.6.

$$y = \frac{1}{2} \ln \frac{1 - x_1}{1 - x_3} \tag{4.5}$$

$$d\sigma \propto \alpha_s \frac{dp_\perp^2}{p_\perp^2} dy \tag{4.6}$$

The available phase space for emissions can be approximated by a triangle in the $(\ln(p_\perp^2), y)$ plane, figure 4.5. The light and medium gray area defines the phase space available for the first emission and the medium grey and dark grey shows the phase space available for the second. Note the second emission has an added degree of freedom which depends on the first emission. The CDM proves to be a good approximation only when the emissions of gluons are strongly ordered in $p_\perp^2 : p_{\perp 1}^2 > p_{\perp 2}^2 > p_{\perp 3}^2$. However, as can be seen from figure 4.5 there exists the possibility of emissions above the first. This is, however, suppressed by introducing a Sudakov form factor (i.e. exponential dependence, $e^{P_T^2}$) into the probability of emitting a gluon at some scale $p_\perp$.

In addition to emission of gluons there is the splitting of gluons into $q\bar{q}$ pairs. The cross section for this event can be factorised into the cross section for $q\bar{q} \longrightarrow q\bar{q}g$ (equation 4.1) and $q\bar{q}g \longrightarrow q\bar{q}Q\bar{Q}$. This second cross section is divided into a contribution from qg and $\bar{q}g$ dipoles. This gives a cross section for splitting a gluon, from a qg dipole, into a $Q\bar{Q}$ pair shown in equation 4.7.

$$\frac{d\sigma_{qg \to qQ\bar{Q}}}{dx_1 dx_3} = \frac{3\alpha_s}{8\pi} \frac{(1 - x_2)^2 + (1 - x_3)^2}{(1 - x_1)} \tag{4.7}$$

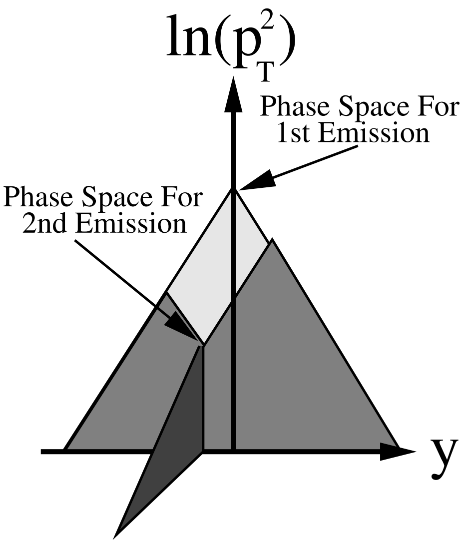

Figure 4.5: Available phase space for gluon emission from the CDM

As before, a Sudakov form factor is introduced to equation 4.7 to suppress further emissions with higher $p_\perp^2$.

This model of g and $q\bar{q}$ production is extended to include DIS by the inclusion of various suppression factors due to the extended nature of the proton and the struck quark. The first of these is due to the extended nature of the proton remnant. Emissions of small wavelengths from extended antenna are suppressed. In ARIADNE the emissions of short wavelength (high $p_\perp$) gluons are suppressed by the factor in equation 4.8,

$$a = \left(\frac{\mu}{p_\perp}\right)^\alpha \tag{4.8}$$

where μ is the inverse size of the proton remnant, about 1 GeV^{-1}, and α the dimensionality of the remnant, equal to 1 for a simple string. This allows only the fraction a of the proton remnant light-cone to take part in emissions with a transverse momentum $p_\perp$. For suppression in the $(\ln(p_\perp^2), y)$ plane equation 4.8 corresponds to the thick line in figure 4.6. Experimentally this

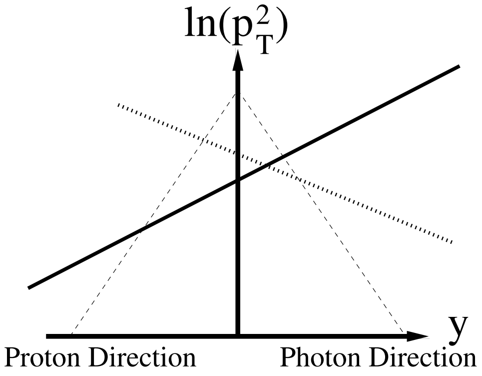

Figure 4.6: Phase space suppression from proton remnant in the CDM

suppresses gluon emission in the direction of the proton.

A second, smaller, suppression of the phase space comes from the extended nature of the struck quark itself. As the probing photon can only ‘see’ to a distance $d \propto 1/Q$, the photon cannot resolve below this scale. When the scatter has low Q^2 and low x the quark is not free and has some associated structure. Thus another suppression of the form in equation 4.8 is imposed. This is shown by the thick dotted line in figure 4.6.

To balance this sharp cut-off in the phase space another factor is introduced. This governs the probability of emissions above the suppression line, allowing a fraction a' of the remnant's light-cone momenta to take part in the emission with probability given by equation 4.9. The factor b is a free parameter of the model, thus the probability of ‘above cut-off’ emissions can be adjusted. This is also the Sudakov suppression factor used in ordering emissions.

$$\frac{dP(a')}{da'} = \frac{b}{a}\frac{\left(\frac{a'}{a}\right)^{b-1}}{\left(1+\left(\frac{a'}{a}\right)^{b}\right)^{2}} \tag{4.9}$$

4.2.1 The JETSET Event Generator

The ARIADNE MC generator uses the JETSET [42, 43, 44] event generator to perform its hadronisation. The hadronisation model used in JETSET is based on the Lund String Model.

The Lund string model assumes the idea of linear confinement. That is, each pair of coloured partons is assumed to have a colour field between them which can be modelled as a colour flux tube. The flux tube stretches as the two partons move apart until there is enough energy, stored as tensile energy in the tube, to provide mass for two new coloured partons. As this process continues all coloured partons are colour connected into colour neutral object which do not have enough energy to create more partons.

Naturally this model has many parameters which have been tuned over the years to produce the correct number and type of particles. This model has proved very successful in describing experimental data.

4.3 The HERWIG Event Generator

The HERWIG [47] event generator simulates the whole particle collision process and need not be used in conjunction with other programs. The program contains a database of electroweak and QCD $2 \rightarrow 2$ scattering sub-processes and it uses this as a starting point in determining initial and final state radiation.

The momentum transfer scale, Q, and initial parton energies (dependent on x when one or both of the partons are hadron constituents) are then used to calculate the initial and final state radiation by using a branching algorithm called the *coherent initial/final state branching* algorithm. The only difference between the two processes is that for initial state radiation the struck parton is evolved down to the scale defined by the hard sub-process and the final state carries on this branching evolution to some cut-off scale. The assumption that parton emission can be described by a branching algorithm is justified because the emission of partons has been shown, given certain caveats, to be factorisable.

The final stage of the event simulation is the progression from partons to hadrons. The model used in HERWIG is loosely based on Local Parton Hadron Duality (LPHD) which can be summarised as :

> . . . partons are converted into hadrons locally in phase space.

and proposes that the relative hadron production ratios are independent of the hard scale of the event and only rely on the parton to hadron conversion parameters.

The clustering process starts with all the gluons being converted into quark anti-quark or di-quark pairs. Once this is done each quark can be colour connected to an anti-quark or di-quark pair to form a colourless object. Once these clusters have been formed they are fragmented into hadrons (the type of which is dependent on the quark flavours) relative to the invariant mass of the cluster.

4.4 The ZEUS Detector Simulation

Once the event generators have produced an event in the desired region of kinematic phase space the output can then be used as input to the ZEUS detector simulation. The process of tracking these events in a detector is statistical by nature. For this reason a sufficient number of events must be simulated to obtain an accurate simulation.

The detector simulation, called MOZART, is based on the GEANT package [45] and simulates the passage of the generated particles through the ZEUS detector. This simulation includes such things as curvature of charged particles from the inner tracking field, loss of energy from ionisation in tracking chambers and the deposition of energy in the calorimeter.

The detector simulation evolves with each year data-taking period. Between the 1995 and 1996 period the VXD was removed and part of the BPRES installed. These changes in the detector set up are included in the detector simulation. For the 1996 and 1997 data taking periods the detector underwent no major changes, and thus the 1996 detector simulation was used to correct the 1997 data sample.

In Table 4.1 a list of the MC sample for each year's data is shown with the number of events simulated, generator and PDF used. Two MC samples were used to correct the 1995 data sample. The lower Q^2 sample was used to correct the data with $Q^2 < 80$ GeV^2 and the higher MC sample for $Q^2 > 80$ GeV^2, in order to ensure sufficient statistics were used to correct the whole kinematic region of the data sample.

4.5 Tuning An Event Generator

To evaluate a "good" set of tuned parameters it is necessary to measure, using a χ^2, the model's ability to describe experimental distributions. A useful tool that facilitates this, developed by the Future Physics at HERA Workshop, is the HZTool package [39]. This package has stored within it various experimental distributions, which can be accessed and compared to a model's prediction. The tool also applies the exact cuts and selection criteria to the model, thus reproducing the experimental analysis. In using

Year	Number (1000's)	Kinematic Cuts	Generator	PDF
1995	500	Q^2 >6	HERWIG	GRV 94
1995	1000	Q^2 >6	ARIADNE	GRV 94
1995	100	Q^2 >70	HERWIG	MRS A'
1995	380	Q^2 >40	ARIADNE	MRS A'
1996	100	Q^2 >70	HERWIG	MRS A'
1996	200	Q^2 >70	ARIADNE	MRS A'

Table 4.1: Table showing Monte Carlo events generated to correct the 1995 and 1996 data samples.

this tool the calculation and storage of χ^2 is automatic.

The first step taken was to run ARIADNE in conjunction with HZTool for 100,000 DIS events. Different PDFs were used to determine whether a large change in results occurred. A decision was made to tune using only the GRV PDF, which best described the data, because including other PDFs would be excessively CPU time consuming.

With many experimental distributions available, a function of many χ^2 is needed, denoted by $f\left(\chi^2\right)$. However, it is a difficult decision to determine which χ^2 values should be included, and the weighting of each. This problem has previously occurred in similar work, to quote [46] ...

> ... among the many possible distributions some have been chosen in an ad hoc way, ...

In overcoming this problem the DELPHI [46] collaboration calculated sensitivity plots for all tuning parameters and distributions. Examination of these sensitivity plots then determines which distributions should be included in the tuning.

4.5.1 Sensitivity Plots

In equation 4.10 the definition of a sensitivity distribution is shown; where $\delta MC(x)$ is the change of the distribution $MC(x)$ when changing the model parameter p_i by δp_i around its central value, where δp_i is a reasonable change consistent with the physical quantity under investigation. An example of a sensitivity plots is shown in figure 4.7; with the parameter PARA(10) as 0.5 and 2.0. The distribution analysed is an energy energy correlation [48].

$$S(x) = \frac{\left.\frac{\delta MC(x)}{MC(x)}\right|_{p_i}}{\frac{\delta p_i}{p_i}} \tag{4.10}$$

To decide on the distributions included in the $f\left(\chi^2\right)$ several sensitivity plots were produced for each distribution available in HZTool. This would allow the distributions sensitive to certain parameters to be included in the $f\left(\chi^2\right)$. A large number of events (roughly 100,000) were produced with ARIADNE with the default parameters (shown in table 4.3) changed to double and half the nominal value. To reduce the number of parameters to a manageable level, PARA(1) and PARA(3), which have been previously tuned by the DELPHI collaboration at LEP [46], were held at their default values. The last 5 parameters of table 4.3 are highly correlated which adjust the phase space suppression. The three most sensitive parameters are PARA(10), PARA(15) and PARA(27) and adjust the gradient and intercept of the two suppression lines in figure 4.6; they relate to the parameters α and μ in equation4.8 for both the proton remnant and struck quark. Thus, only plots that were 'sensitive' to these final 3 parameters were to be considered in $f\left(\chi^2\right)$.

To decide whether a plot is 'sensitive' the weighted mean (equation 4.11) of the sensitivity plot is calculated. If the absolute value is above 0.2 the

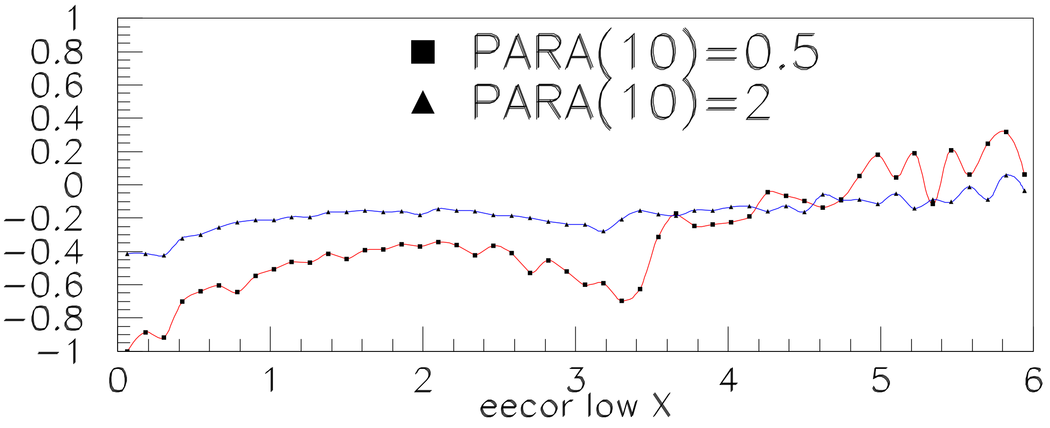

Figure 4.7: Sensitivity plot for an Energy Energy Correlation at low x.

plot is considered 'sensitive'. However, if the statistics are very low, large fluctuations can occur in the plot so it is ignored altogether. This method then gives a list of which plots are sensitive to changes in the 3 parameters to be tuned.

$$\bar{x}_{weighted} = \frac{\sum_i \left(\frac{S_i(x)}{\sigma_i^2}\right)}{\sum_i \left(\frac{1}{\sigma_i^2}\right)} \tag{4.11}$$

In conjunction with others tuning the generators LEPTO and HERWIG [47], a list of distributions was produced. This is shown in table 4.2. A complete description of the distributions can be found in the relevant DESY preprints (see table), with the plots being identified by the histogram identification number in the HZTool manual. This list encompasses a range of physical processes measured in DIS.

4.5.2 Results Of Tuning ARIADNE

A program was written to scan the 3 parameters over $(6 \times 6 \times 5)$ points; the values for the various sets are shown in table 4.3. For each of the parameter space points $f(\chi^2)$ was calculated, then a simple program to determine the

Preprint Number	ID in HZTool	Description
94-033 [48]	19	$\langle P_{\perp}^{*2} \rangle$-vs-$x_f$
	116	Charged particle spectrum for $\langle W \rangle = 77$ GeV
	118	Charged particle spectrum for $\langle W \rangle = 169$ GeV
95-007 [49]	113	$\log 1/x_p$ in the Breit frame for bin 2
	123	$\log 1/x_p$ in the Breit frame for bin 3
	144	$\log 1/x_p$ in the Breit frame for bin 6
95-108 [50]	11	$E_{\perp}$-vs-η for $\langle x \rangle = 0.00016$ and $\langle Q^2 \rangle = 6.8$ GeV^2
	14	$E_{\perp}$-vs-η for $\langle x \rangle = 0.00063$ and $\langle Q^2 \rangle = 14.2$ GeV^2
	18	$E_{\perp}$-vs-η for $\langle x \rangle = 0.0021$ and $\langle Q^2 \rangle = 30.9$ GeV^2
	21	$\langle P_{\perp} \rangle$ at $\eta = 0$
95-221 [51]	12	charged particle $P_{\perp}$ distribution
	13	$\langle P_{\perp}^{*2} \rangle$-vs-$x_f$

Table 4.2: Table of sensitive distributions to be included in $f\left(\chi^2\right)$.

Parameter	Default Value	Scanned Points	Tuned
PARA(1)	0.22	-	0.22
PARA(3)	0.6	-	0.6
PARA(10)	1.0	0.5,0.75,1.0 1.25,1.5,1.75	1.5
PARA(14)	1.0	-	1.0
PARA(15)	1.0	0.5,0.75,1.0 1.25,1.5,1.75	0.5
PARA(25)	2.0	-	2.0
PARA(27)	0.6	0.5,0.75,1.0,1.25,1.5	0.6

Table 4.3: Table of tuned parameters for DIS with ARIADNE

minimum was written. A graph of $f\left(\chi^2\right)$ values at various parameter points is shown in figure 4.8. To obtain an error on the value of $f\left(\chi^2\right)$ ARIADNE was run a number of times with the same parameter values, re-setting the random number seed each time. This gave a variation in the value of $f\left(\chi^2\right)$ of ±5%. This was taken as the error for the scan. The value of $f\left(\chi^2\right) = 5.46$ for the default values; after tuning this was reduced to $f\left(\chi^2\right) = 3.99 \pm 0.20$. One of the largest improvements was in the Seagull plot which is shown in Figure 4.9(d) where the default and tuned distributions are shown along with the experimental distribution. Other distributions which were included in the $f(\chi^2)$ are also shown in Figure 4.9. Other distributions, such as the energy energy correlations used in figure 4.7, did improve with the new tuned values; but were not included in the $f\left(\chi^2\right)$. However, some of the transverse energy flow distributions which were included in $f\left(\chi^2\right)$ did get slightly worse but were still well within experimental errors.

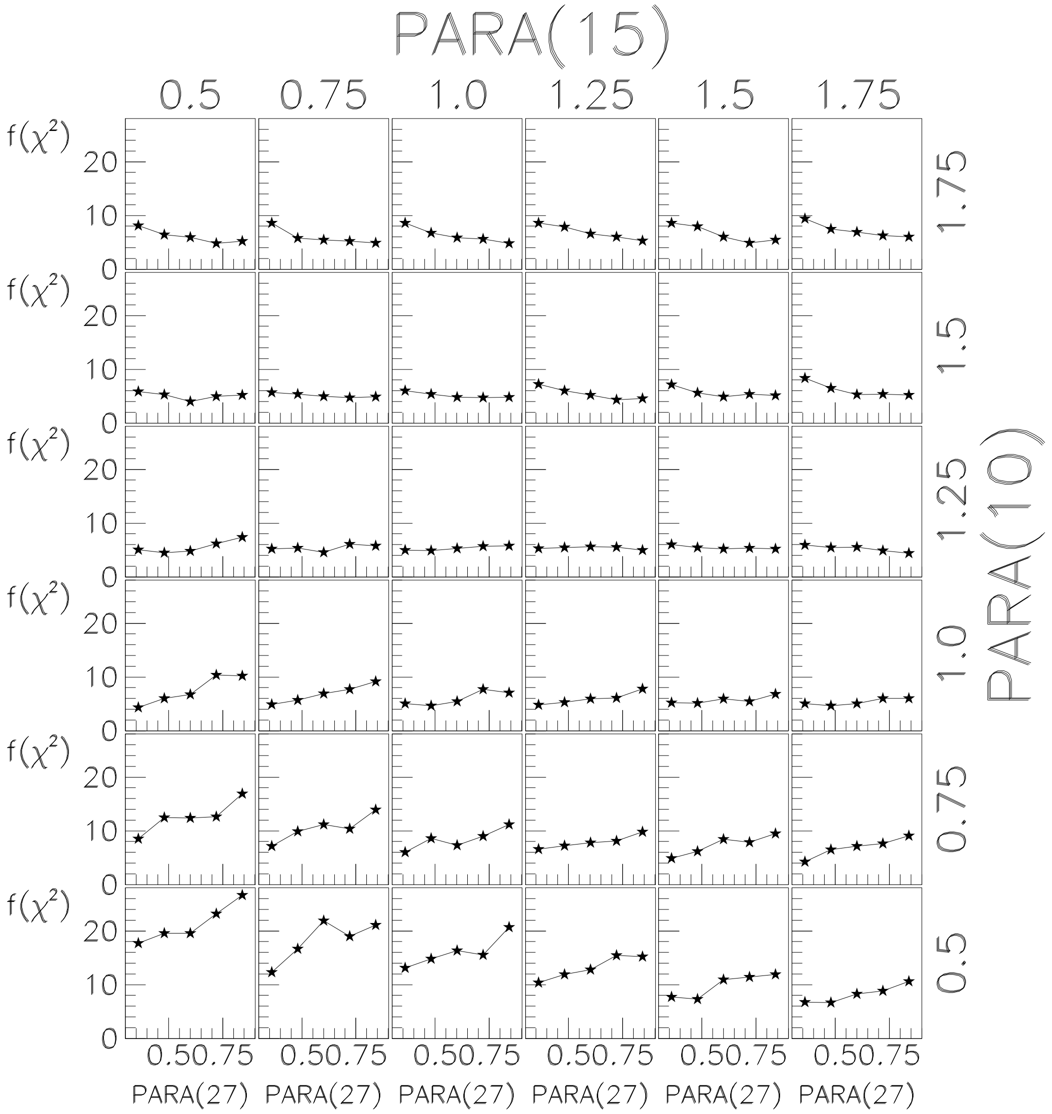

Figure 4.8: Variation of $f\left(\chi^2\right)$ as a function of the tuned parameters PARA(10), PARA(15) and PARA(27).

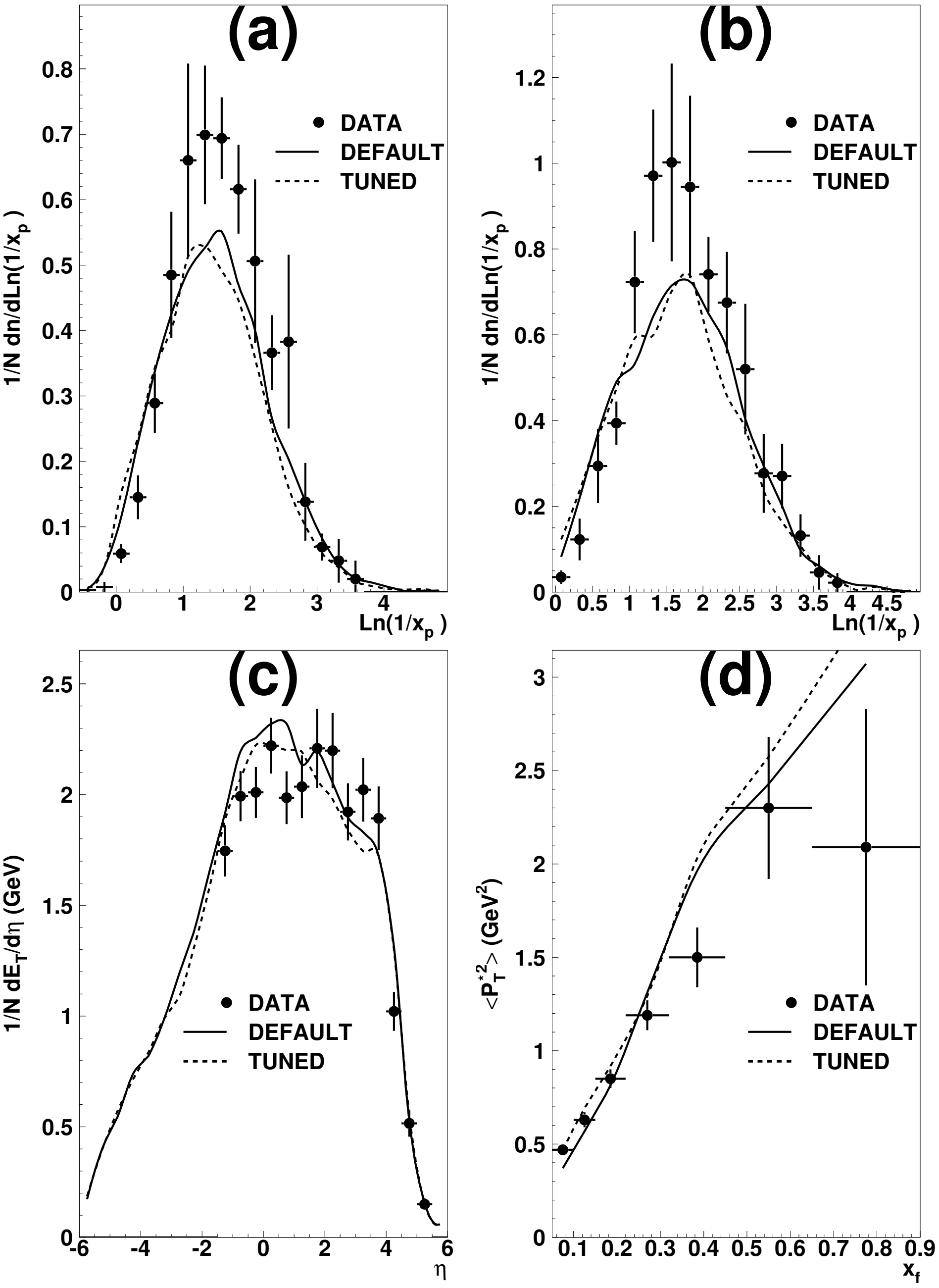

Figure 4.9: Data (points), default MC (line) and tuned MC (dashed) plots of $\ln(1/x_p)$ for bins 2 (a) and 3 (b), E_T as a function of η (c) and the Seagull plot (d).

In conclusion, the ability of ARIADNE to reproduce experimental data has improved. Only one PDF was used and, as such, the tuned values only apply while using the GRV PDF. The generators LEPTO and HERWIG were also tuned by other members of the working group.

Chapter 5

Monte Carlo Studies

The ZEUS detector is a very complex system of subcomponents, an analytic evaluation of resolutions and migrations impossible. This chapter presents and discusses the work undertaken involving the Monte Carlo event generators and detector simulation. Studies of simulated event are essential in determining the resolution of measurements and the complex interplay of migrations which occur in reconstructed data.

These studies will first deal with the kinematic variables x_{DA} and Q^2_{DA} which are needed to define DIS events (see section 2.1). These studies have been performed for all event shape variables presented in this work but, due to brevity, only the results for the variable thrust (T_z) will be shown. Specific uncertainties on the measurement of thrust, due to detector resolution, will be discussed and various contributions to the uncertainty evaluated.

The results from these Monte Carlo studies can only be considered correct if the event generators and detector simulation give a good description of the measured data. The final section of this chapter deals with the extent to which these simulations model the measured data.

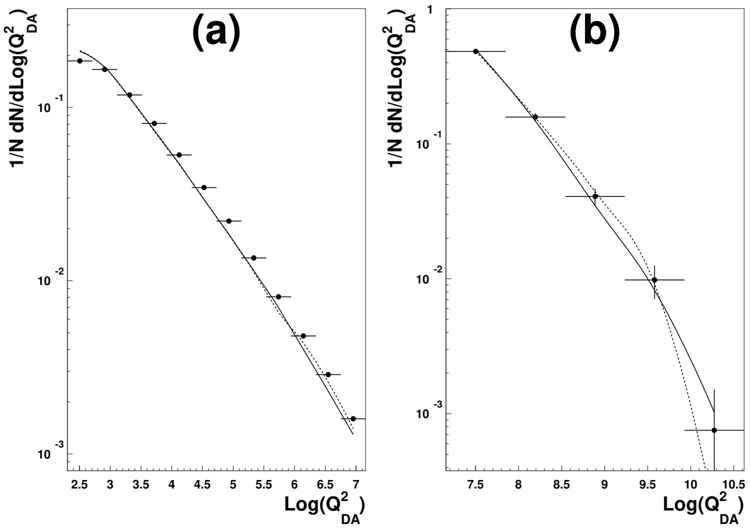

Figure 5.1: Q^2_{DA} distributions for 1995 data (as points), ARIADNE (solid line) and HERWIG (dashed line) using 1995 detector simulation. Part (a) is low and part (b) high Q^2 sample.

5.1 Reproduction of Kinematics

The kinematic ranges used in this analysis, given in Table 3.1, have been determined from previous work regarding resolution of kinematic variables and acceptance of tracks in the current region of the Breit frame.

The area normalised distributions for 1995 uncorrected data, detector level ARIADNE and HERWIG (both with the 1995 detector simulation) are shown in Figure 5.1. Both generators produce a reasonable reproduction of the data for the high Q^2 sample. However, the low Q^2 sample shows a slight discrepancy for the lower bins. As this is the bin with the largest statistics the rest of the distribution is steepened. This difference between data and MC is from the inclusion of a pre-scaled trigger. A pre-scaled trigger is where the ZEUS trigger system throws away certain events, in this case DIS events

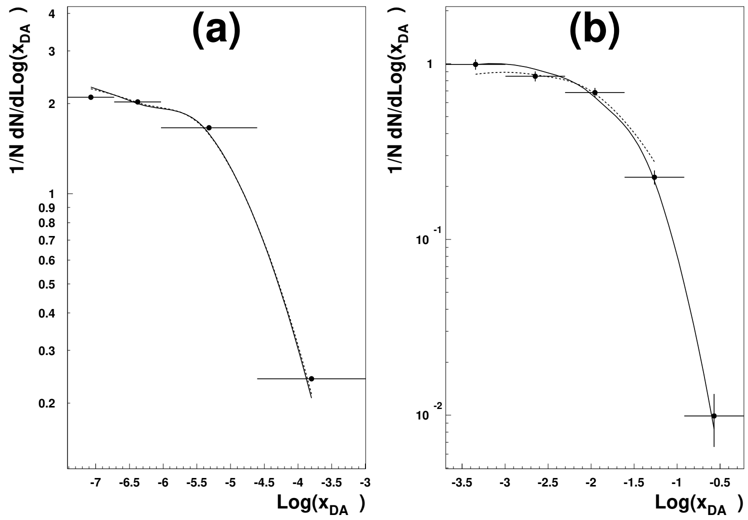

Figure 5.2: x_{DA} distributions for 1995 data (as points), ARIADNE (solid line) and HERWIG (dashed line) using 1995 detector simulation. Part (a) is low and part (b) high Q^2 sample.

with $Q^2 < 10$ GeV^2, to save data storage space; this way storage area can be used for more interesting, or less well measured, events.

In Figure 5.2 the equivalent plot for the x distribution is shown. Again the left figure is the low Q^2 sample and the right figure the high Q^2 sample. Both sample reproduce the data well, with the possible exception of the lowest x bin of the low Q^2 sample. This is again due to the pre-scale difference between data and MC.

The same distributions are presented in Figure 5.3 for the 1996 and 1997 combined data along with the ARIADNE and HERWIG MC sample reconstructed using the 1996 detector simulation. For the 1996 and 1997 data analyses only events with $Q^2_{DA} > 80$ GeV^2 are analysed. The left distribution in Figure 5.3 shows the Q^2_{DA} distribution while the right distribution is the x_{DA} distribution.

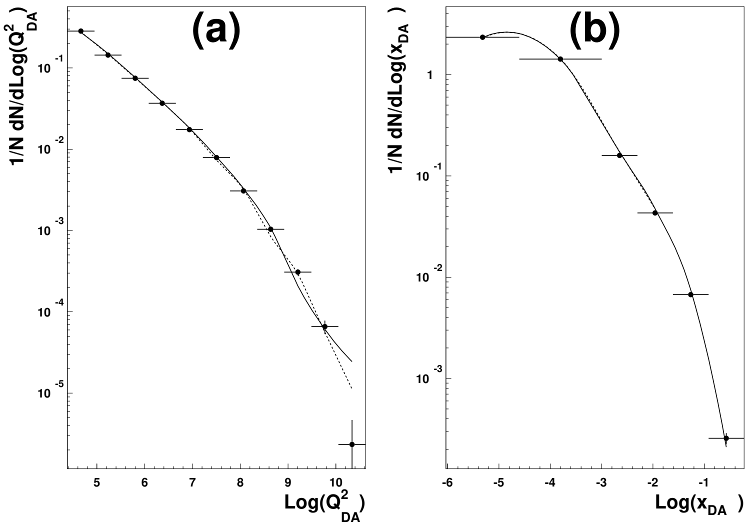

Figure 5.3: Q^2_{DA} (a) and x_{DA} (b) distribution for reconstructed 1996 and 1997 data (as points), ARIADNE (solid line) and HERWIG (dashed line) using 1996 detector simulation.

5.2 Resolution Of Observables

The first of the Monte Carlo studies deals with the measured accuracy of the kinematic variables x and Q^2. A useful way to present the accuracy in measuring these variables is to plot the value of the variable determined from the "reconstructed" level minus that of the "truth" level and normalised to the reconstructed value to obtain the fractional error. A plot of this resolution parameter for the variable Q^2_{DA}, for each of the kinematic ranges, is shown in figure 5.4.

One can see that the distributions are not symmetric and the value of Q^2_{DA} is generally overestimated, producing a slight propensity for events to migrate to higher kinematic bins. However, for the majority of events the reconstructed value of Q^2_{DA} would place the event in the correct range. This is also supported by the RMS value, which is a conservative estimator of resolution, showing that the reconstructed value is well within the kinematic width for each bin.

Shown in figure 5.5 is the same plot of Q^2_{DA} resolution using the ARIADNE event generator but using the 1996 detector simulation. A feature of these plots is the improved accuracy in the measurement of Q^2_{DA} as it increases. This is due to the improving measurement of γ_h from thinner jets and θ_e from higher energy, both used in the calculation of Q^2_{DA}.

In the kinematic overlap region of the 1995 and 1996 MC sample the resolution on Q^2_{DA} is slightly better for 1996. This is due to the VXD being removed during the 1995-1996 shutdown period and thus a reduction in the amount of dead material which acts to broaden the hadronic jet, thus a poorer measurement of γ_h, and energy loss in the scattered electron, thus a poorer energy measurement.

The kinematic variable x_{DA} is shown in the same way in figure 5.6 and 5.7 for the 1995 and 1996 detector simulation respectively. The resolution in x_{DA} is worse than that of Q^2_{DA} but an improvement can be seen as Q^2_{DA} increases, due to the reasons stated above. The conclusion to be drawn from these studies of event kinematics is that for the bins defined the variables are well reconstructed and migrations kept to an acceptably low level.

The kinematic overlap region of the 1995 and 1996 MC sample, as with Q^2_{DA}, shows an improved determination of x_{DA}. This is also due to the reasons stated above.

Now the kinematic variables have been investigated, attention can be focused on the event shape variables. Results for the variable thrust (T_z) will be shown as an example of the studies carried out. All four event shape variables were studied and the conclusions from the other variables presented

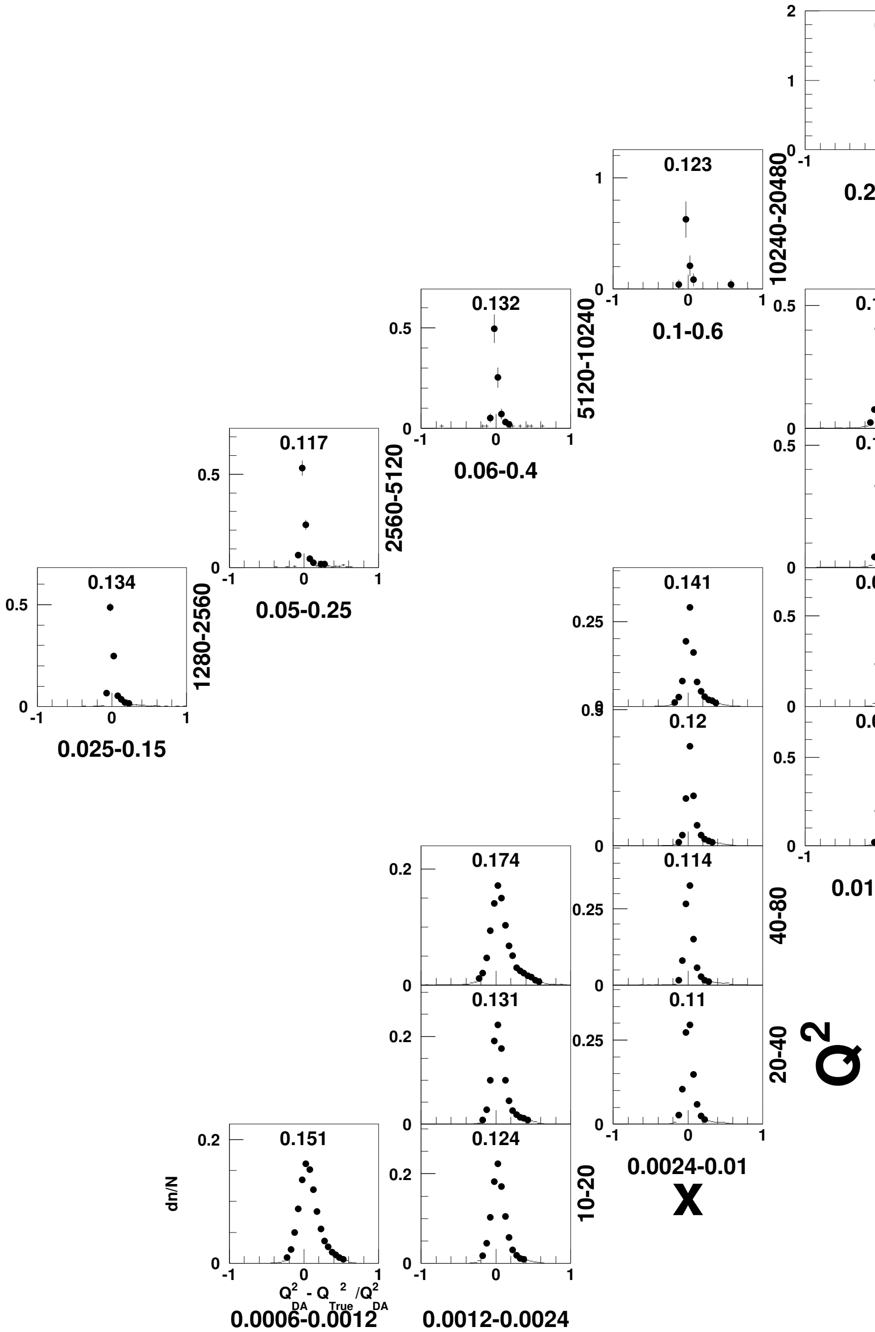

Figure 5.4: Distribution of $(Q^2_{DA} - Q^2_{\mathrm{true}})/Q^2_{DA}$ with the RMS value of the distribution shown for each (x, Q^2) interval. The Monte Carlo generator used was ARIADNE with the 1995 detector simulation.

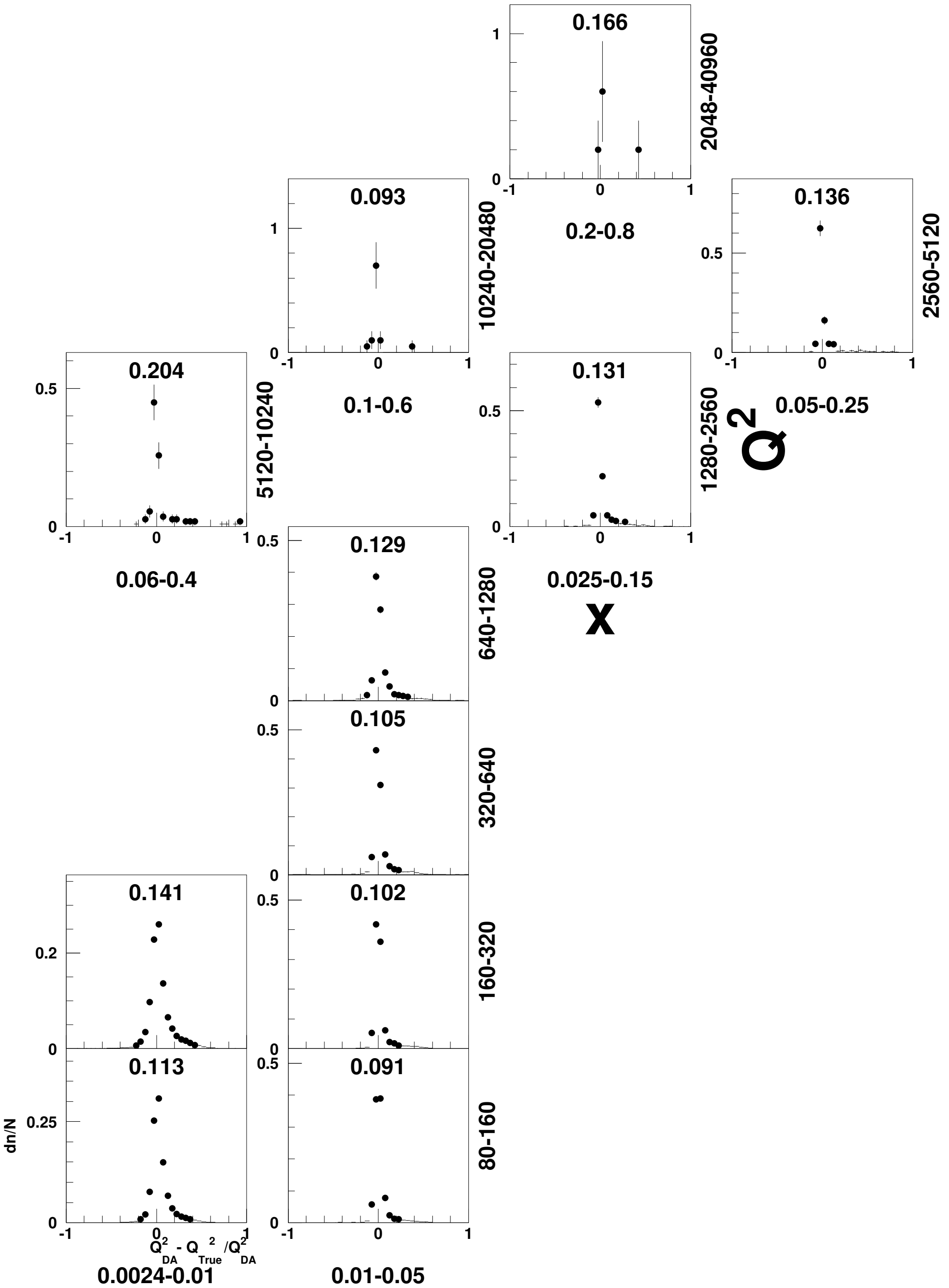

Figure 5.5: Distribution of $(Q^2_{DA} - Q^2_{\rm true})/Q^2_{DA}$ with the RMS value of the distribution shown for each (x, Q^2) interval. The Monte Carlo generator used was ARIADNE with the 1995 detector simulation.

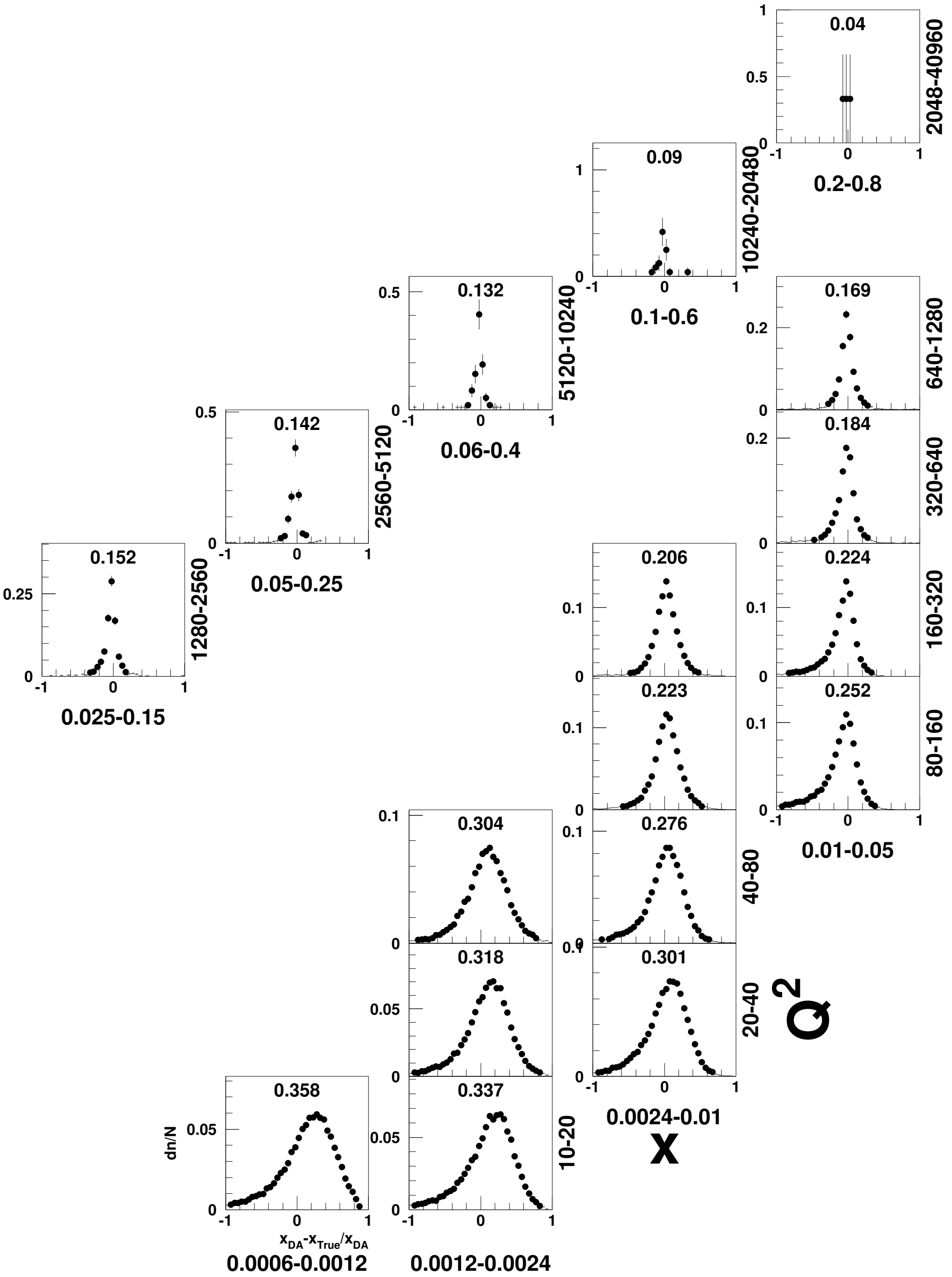

Figure 5.6: Distribution of $(x_{DA} - x_{\rm true})/x_{DA}$ with the RMS value of the distribution shown for each (x, Q^2) interval. The Monte Carlo generator used was ARIADNE with the 1995 detector simulation.

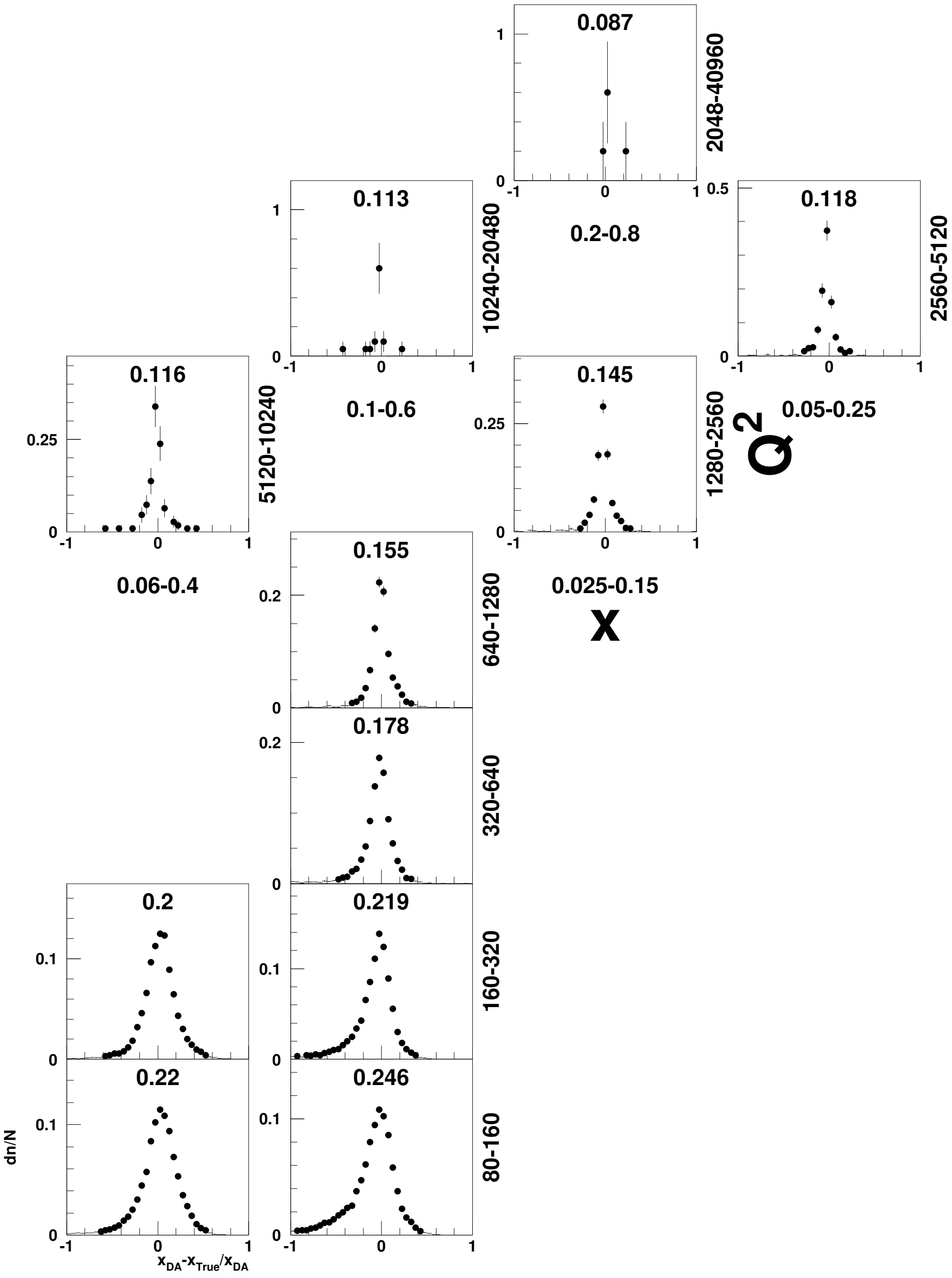

Figure 5.7: Distribution of $(x_{DA} - x_{\mathrm{true}})/x_{DA}$ with the RMS value of the distribution shown for each (x, Q^2) interval. The Monte Carlo generator used was ARIADNE with the 1996 detector simulation.

later in this section.

A plot of the reconstructed thrust minus the true thrust is shown in figure 5.8 for the 1995 detector simulation and figure 5.9 for the 1996 detector simulation. It can be seen from the figures that the resolution in thrust improves with increasing Q^2_{DA}. This is due to the resolution in x_{DA} and Q^2_{DA} improving and thus the improved accuracy of the boost to the Breit frame.

However, there are two factors involved in the increasing resolution of thrust; the first is the improvement of the boost which is counter balanced by the reduction in resolution of track momentum with increasing Q^2. When events have a high Q^2 the available energy to the hadronic final state increases, this produces higher momentum hadrons which are less well measured than lower momentum hadrons (see section 1.3).

From these studies a discrete measurement of the thrust distribution can be achieved with a segmentation of around five or six bins. Studies show that the resolution on thrust is also thrust dependent and, thus, requires a non uniform segmentation. The distribution segmentation chosen in shown, along with the other event shape variables, in table 5.2.

5.3 Efficiencies And Purities Of Event Shape Variables

Now the ranges for the kinematic and event shape variables has been evaluated it is now possible to test how well the events are being measured in the distributions and the correction factors that need to be applied to data. For the first part of this the variables *efficiency* and *purity* are used and from these the correction factors, and errors on the correction factors, can be calculated. The definitions for *efficiency* and *purity* are shown in equations 5.1

Event shape variable	Number of bins	Range	Variable bin ranges
T_Z	6	0.0-1.0	0.0-0.25, 0.25-0.45, 0.45-0.65, 0.65-0.8, 0.8-0.9, 0.9-1.0
B_c	7	0.0-0.5	0.0-0.06, 0.06-0.12, 0.12-0.18, 0.18-0.24, 0.24-0.31, 0.31-0.39, 0.39-0.5
ρ_E	6	0.0-0.25	0.0-0.03, 0.03-0.06, 0.06-0.095,0.095-0.135, 0.135-0.18, 0.18-0.25
C_E	8	0.0-1.0	0.0-0.14, 0.14-0.25, 0.25-0.36, 0.36-0.47, 0.47-0.59, 0.59-0.72, 0.72-0.85, 0.85-1.0

Table 5.1: Table of event shape variable bin sizes.

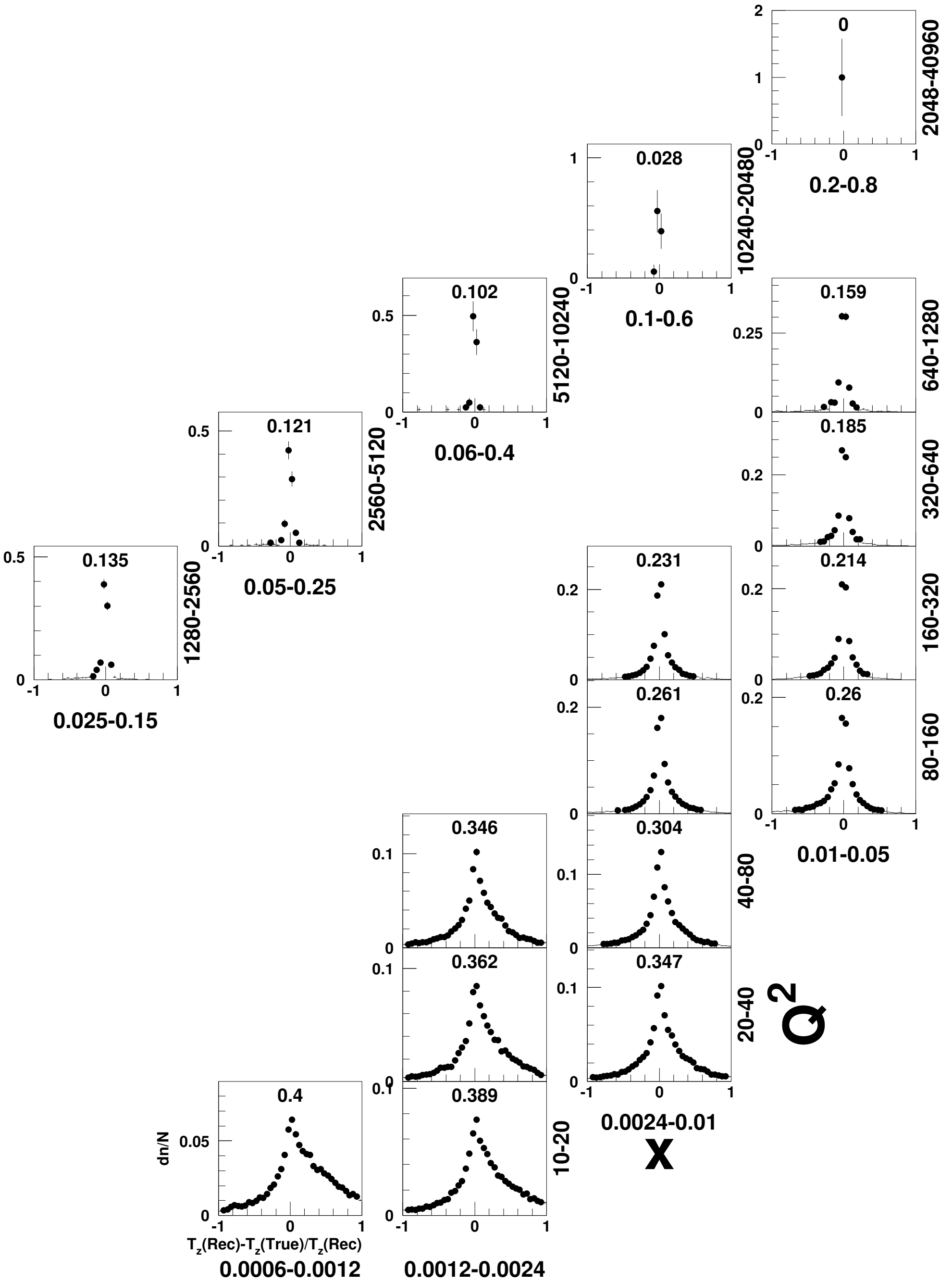

Figure 5.8: Distribution of (T_z(rec) $-$ T_z(true)/T_z(rec) with the RMS value of the distribution shown for each (x, Q^2) interval. The Monte Carlo generator used was ARIADNE with the 1995 detector simulation.

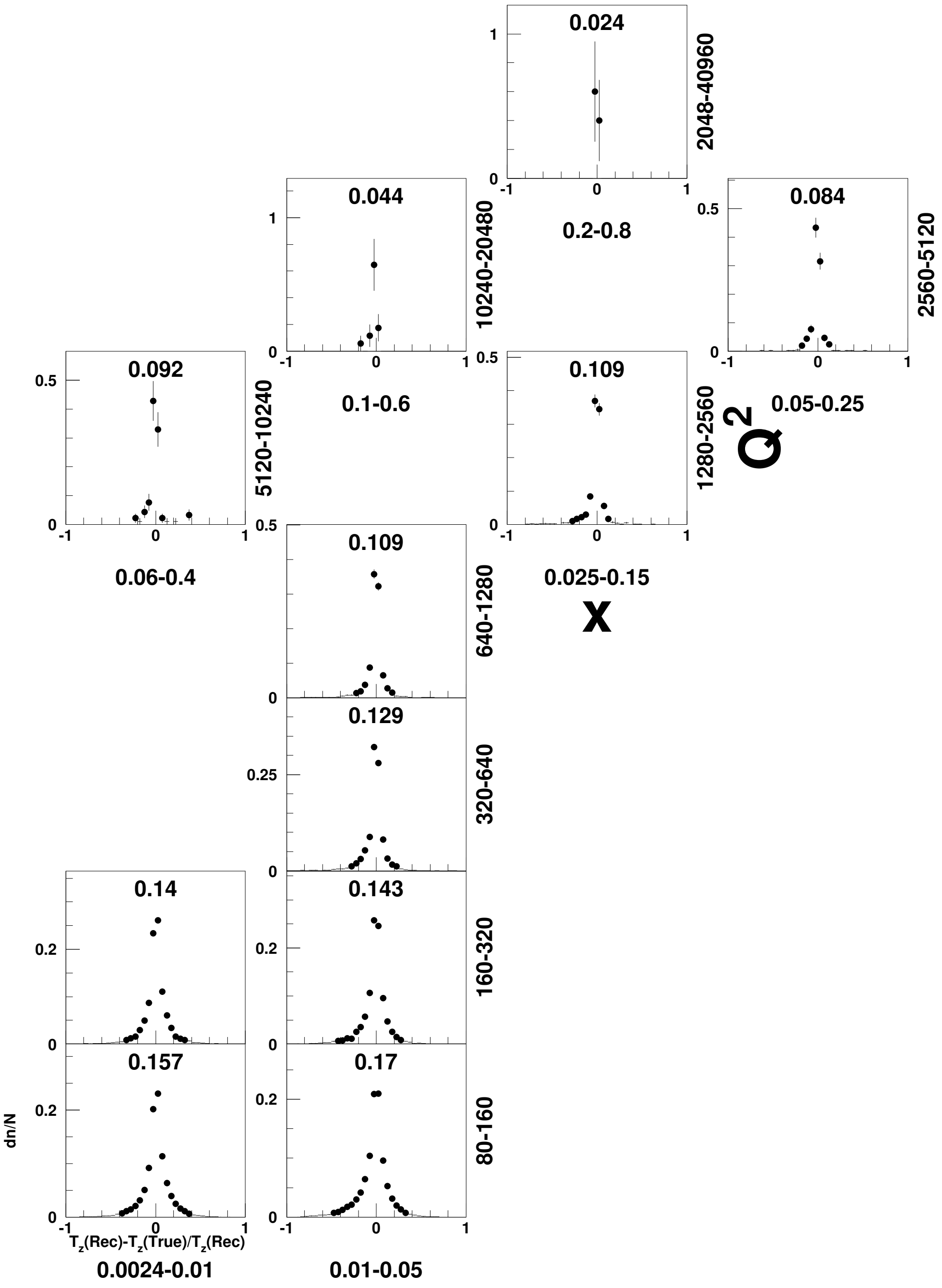

Figure 5.9: Distribution of $(T_z(\mathrm{rec}) - T_z(\mathrm{true})/T_z(\mathrm{rec})$ with the RMS value of the distribution shown for each (x, Q^2) interval. The Monte Carlo generator used was ARIADNE with the 1996 detector simulation.

and 5.2 respectively.

$$\varepsilon_i = \frac{true_i \oplus rec_i}{true_i} \tag{5.1}$$

$$p_i = \frac{true_i \oplus rec_i}{rec_i} \tag{5.2}$$

The first variable, *efficiency* (ε_i), is the number of events that are both generated ($true_i$) and reconstructed (rec_i) in bin i divided by the total number of events generated in that bin. This can be done for any discrete distribution, like Q^2 or thrust, and gives a measure of how efficiently an analysis is correctly measuring a certain variable in a particular phase space.

The second variable, *purity* (p_i), has the same numerator but the denominator is the total number of events reconstructed in bin i. This is a measure of how pure the sample of events in bin i are, or how many events have remained in the correct bin.

Both the efficiency and purity calculated for this analysis are "global", that is to say when we talk of bin i it refers to not only the correct thrust bin, for example, but also the correct kinematic bin (i.e. bin i is a cube in (T_z, x_{DA}, Q^2_{DA}) space). Figure 5.10 and 5.11 show the efficiency of the thrust distribution for the 1995 and 1996 detector simulation respectively. The equivalent plots for purity are shown in figure 5.12 and 5.13.

From the increasing resolution in T_z with increasing Q^2_{DA} (see section 5.2), it is easy to assume that the *efficiency* and *purity* will also improve with increasing Q^2_{DA}. This is indeed the case. However, the lower three bins have rather low *efficiency* and *purity* distributions. Therefore, the final distributions depend more significantly upon the details of the MC.

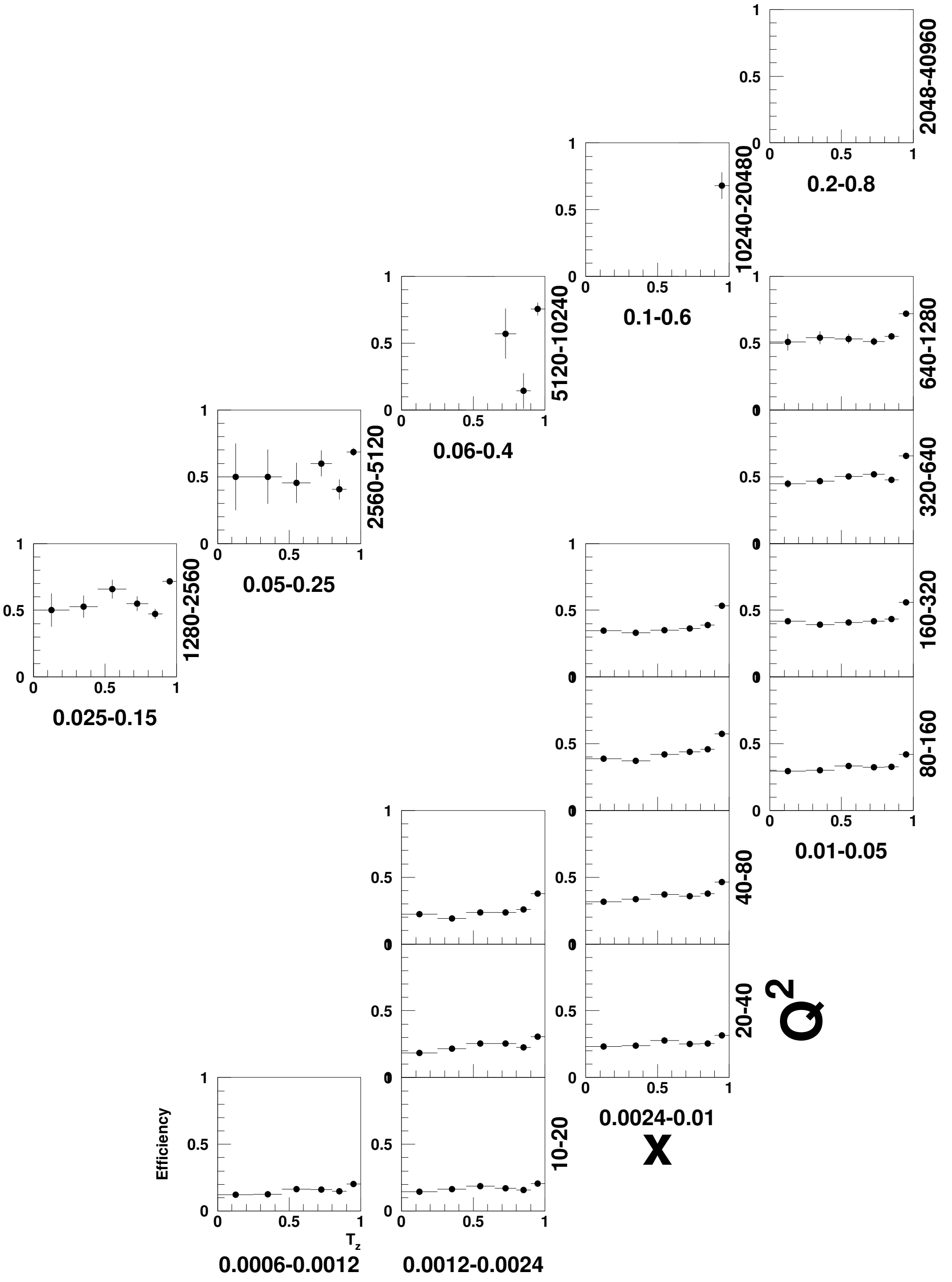

Figure 5.10: Efficiency of thrust distribution. The Monte Carlo generator used was ARIADNE with the 1995 detector simulation.

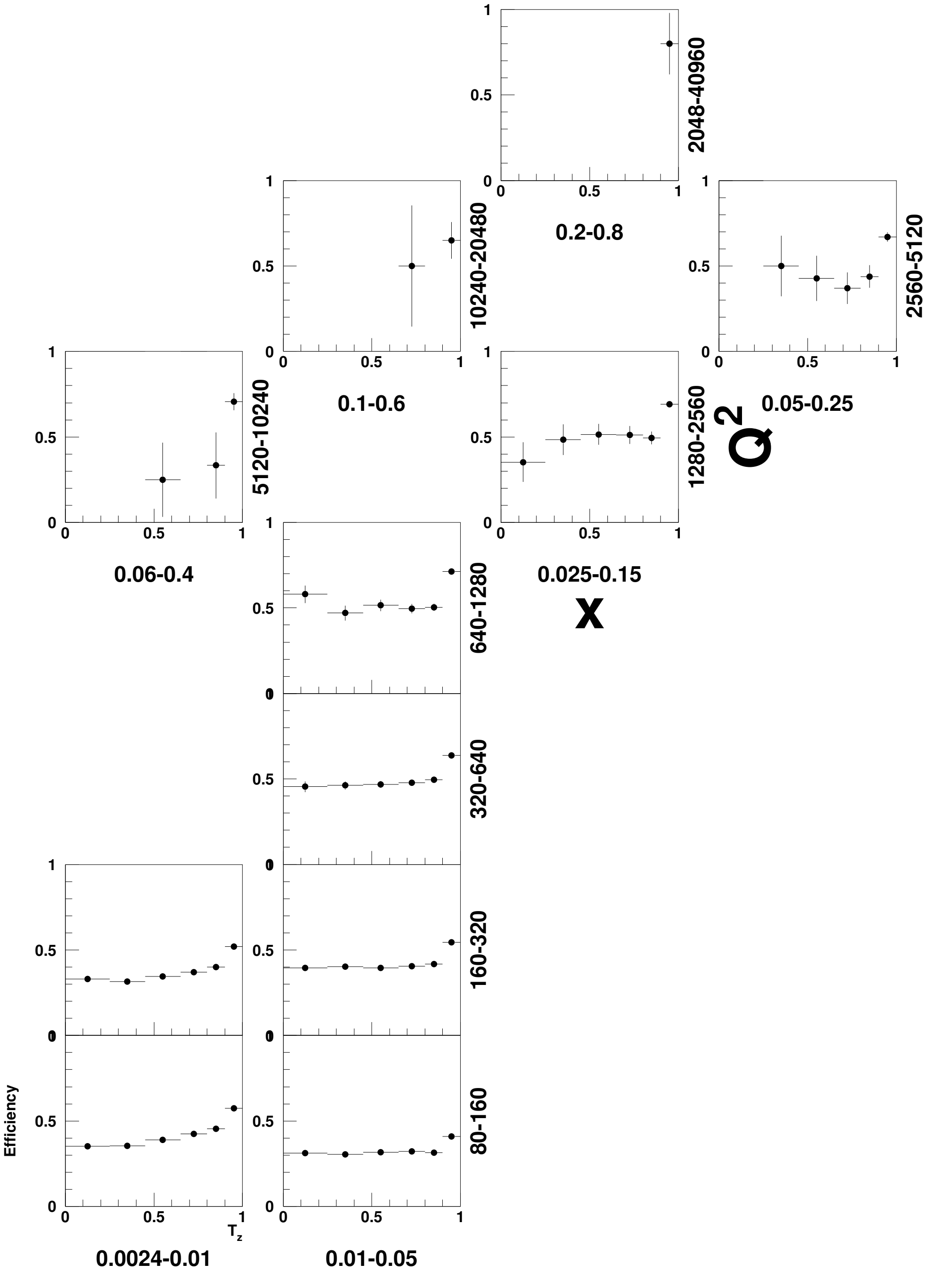

Figure 5.11: Efficiency of thrust distribution. The Monte Carlo generator used was ARIADNE with the 1996 and 1997 detector simulation.

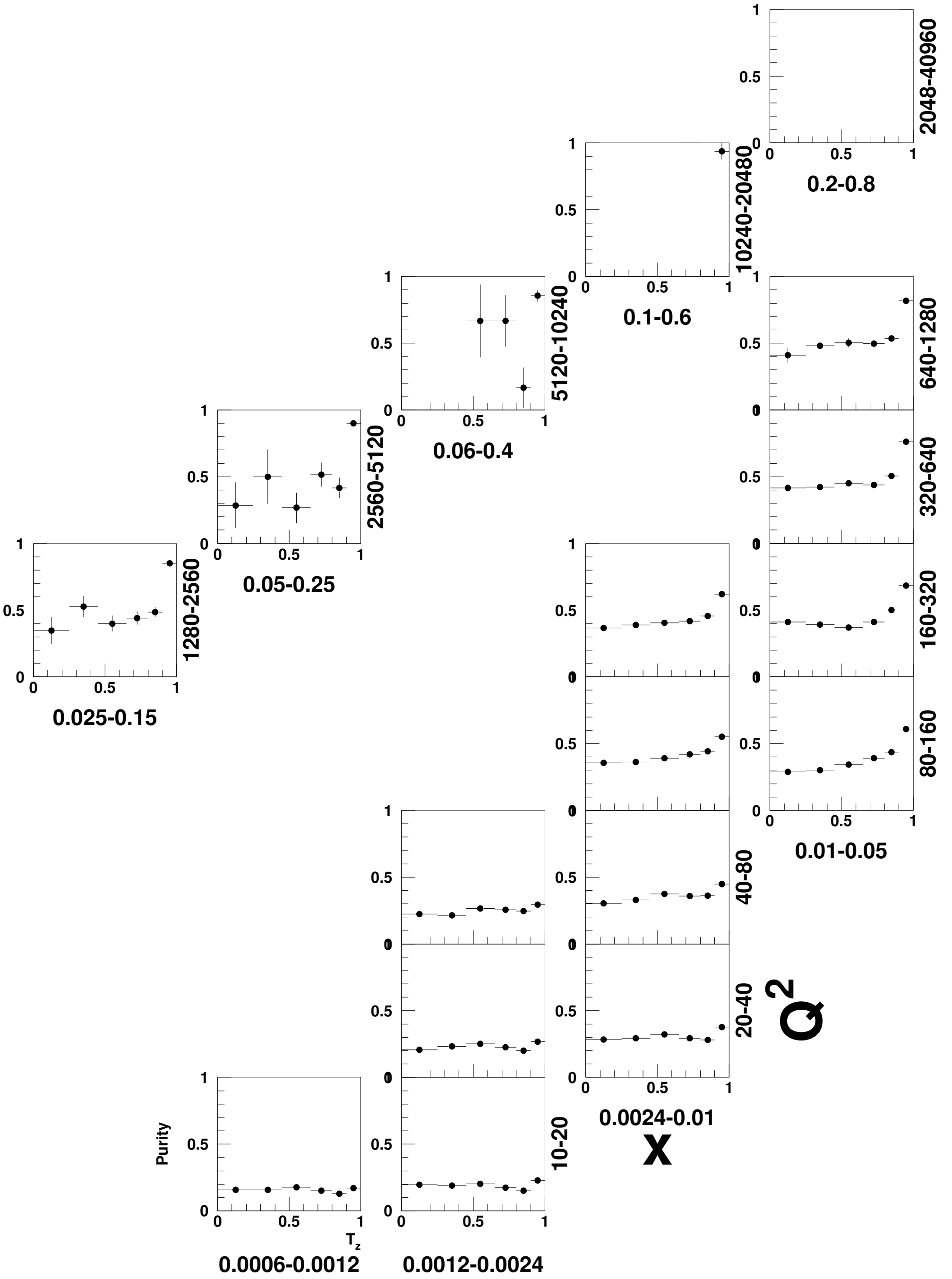

Figure 5.12: Purity of thrust distribution. The Monte Carlo generator used was ARIADNE with the 1995 detector simulation.

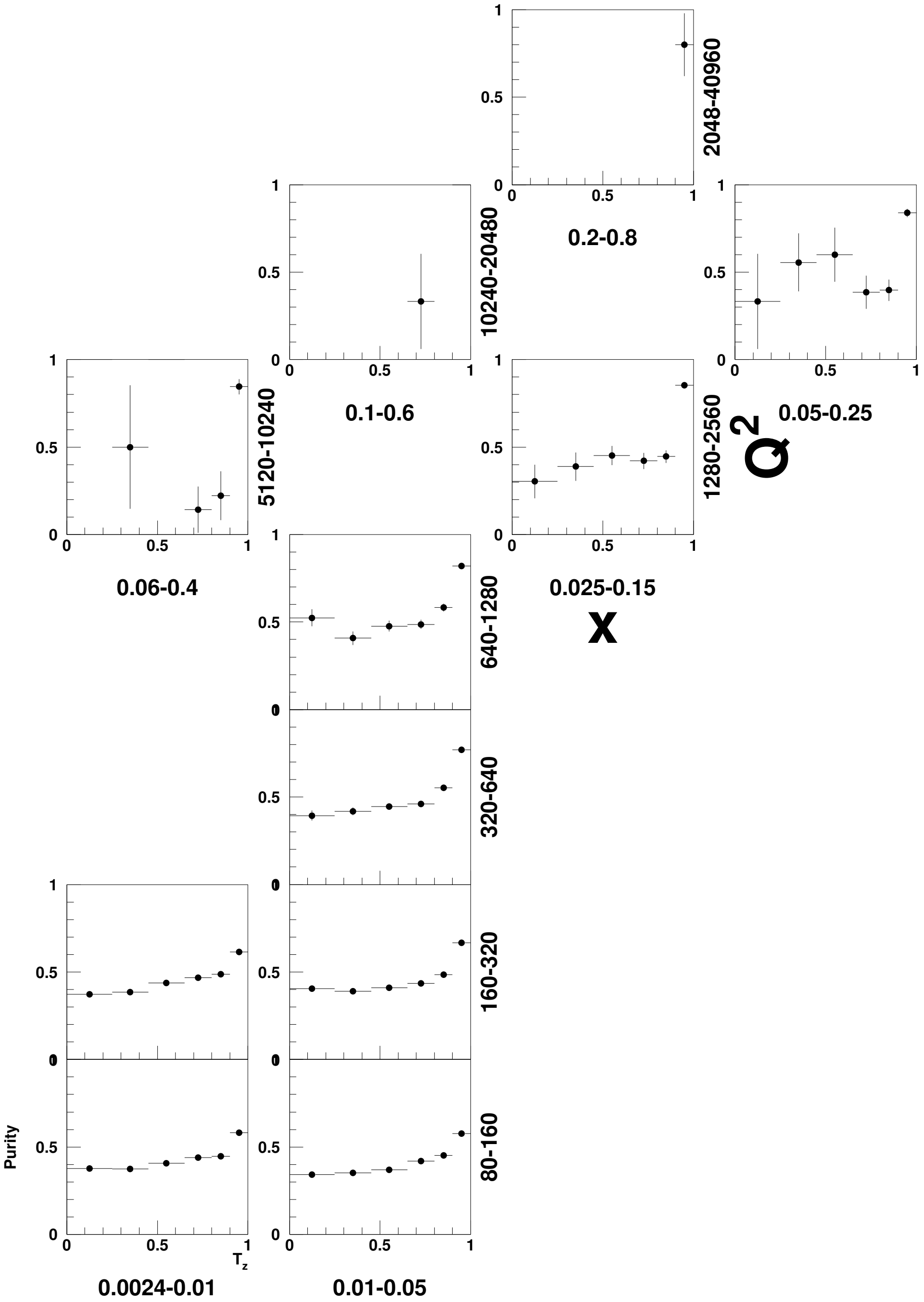

Figure 5.13: Purity of thrust distribution. The Monte Carlo generator used was ARIADNE with the 1996 1997 detector simulation.

5.4 Correction Factors

From the two variables defined in the previous section, *efficiency* and *purity*, it is possible to calculate a correction factor, to be applied to reconstructed data, which will compensate for any migrations of events from bin to bin. This correction factor, c_i, is defined by:

$$c_i = \frac{true_i}{rec_i} \simeq \frac{p_i}{\varepsilon_i} \tag{5.3}$$

The correction factors for the 1995 and 1996 detector simulation are shown in figure 5.14 and 5.15 respectively. Throughout the kinematic range the correction factors for each bin deviates from unity by less than 20%.

5.5 Monte Carlo Description of Thrust

As with the kinematic distributions it is also prudent to examine the ability of the MC event generator to model the distributions of the event shape variables. In Figure 5.16 the differential distribution, normalised to the total number of events in that kinematic bin, for the reconstructed thrust (points) along with the reconstructed distributions for the 1995 MC sample of ARIADNE and HERWIG are shown. Figure 5.17 shows the same distribution for the combined 1996 and 1997 data sample along with ARIADNE and HERWIG MC samples using the 1996 detector simulation.

The differential distributions are reproduced quite well by both the ARIADNE and HERWIG generator for all years data. Some discrepancy can be seen at very high thrust ($T_z \sim 0.9 - 1.0$) and low x and Q^2 but the general features of the distribution are acceptable.

The reconstructed MC data for the other event shape differential distributions reproduce the data equally as well or better than that for thrust. A

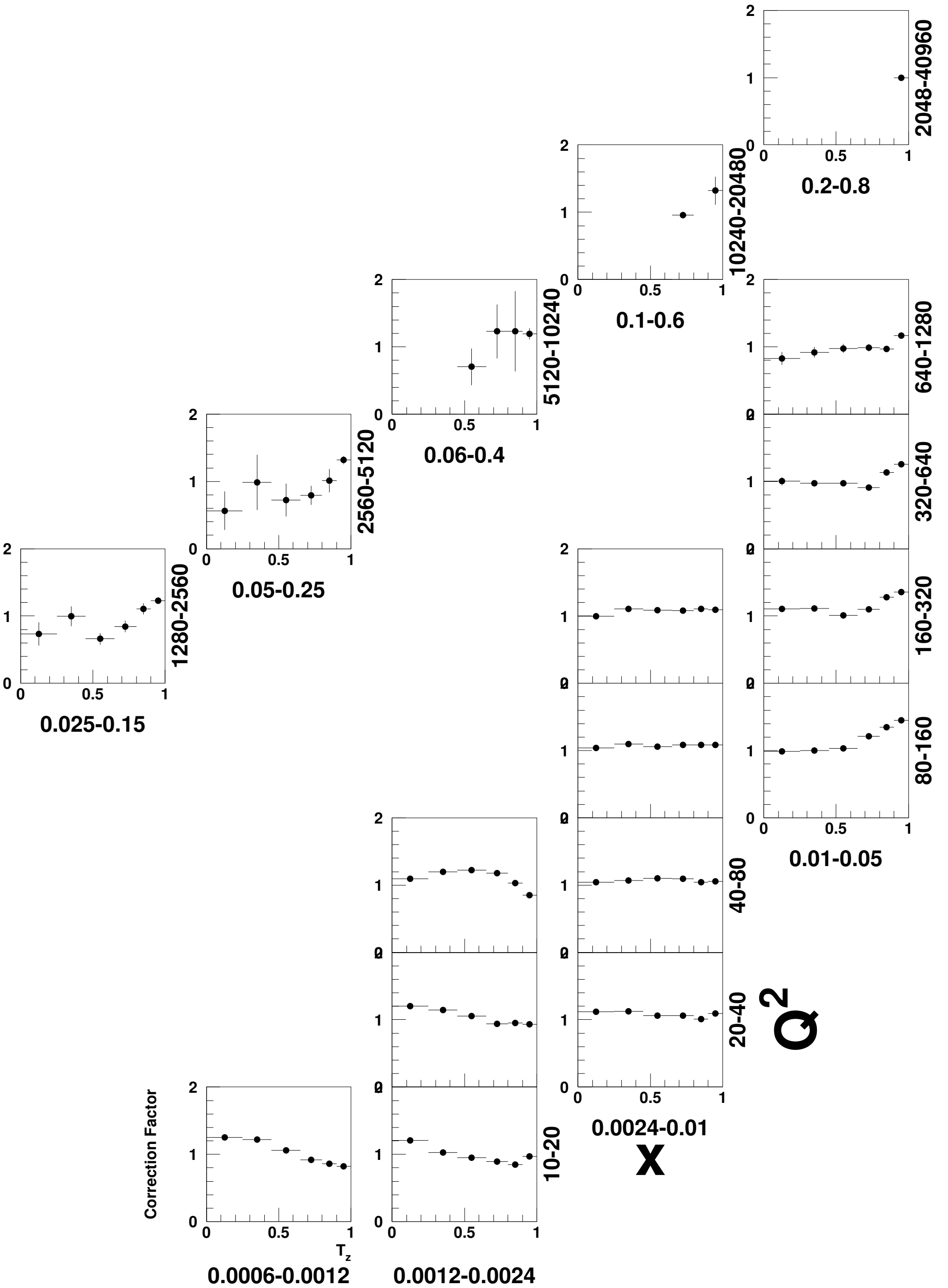

Figure 5.14: Correction factors for thrust shown with the RMS value of the distribution. The Monte Carlo generator used was ARIADNE with the 1995 detector simulation.

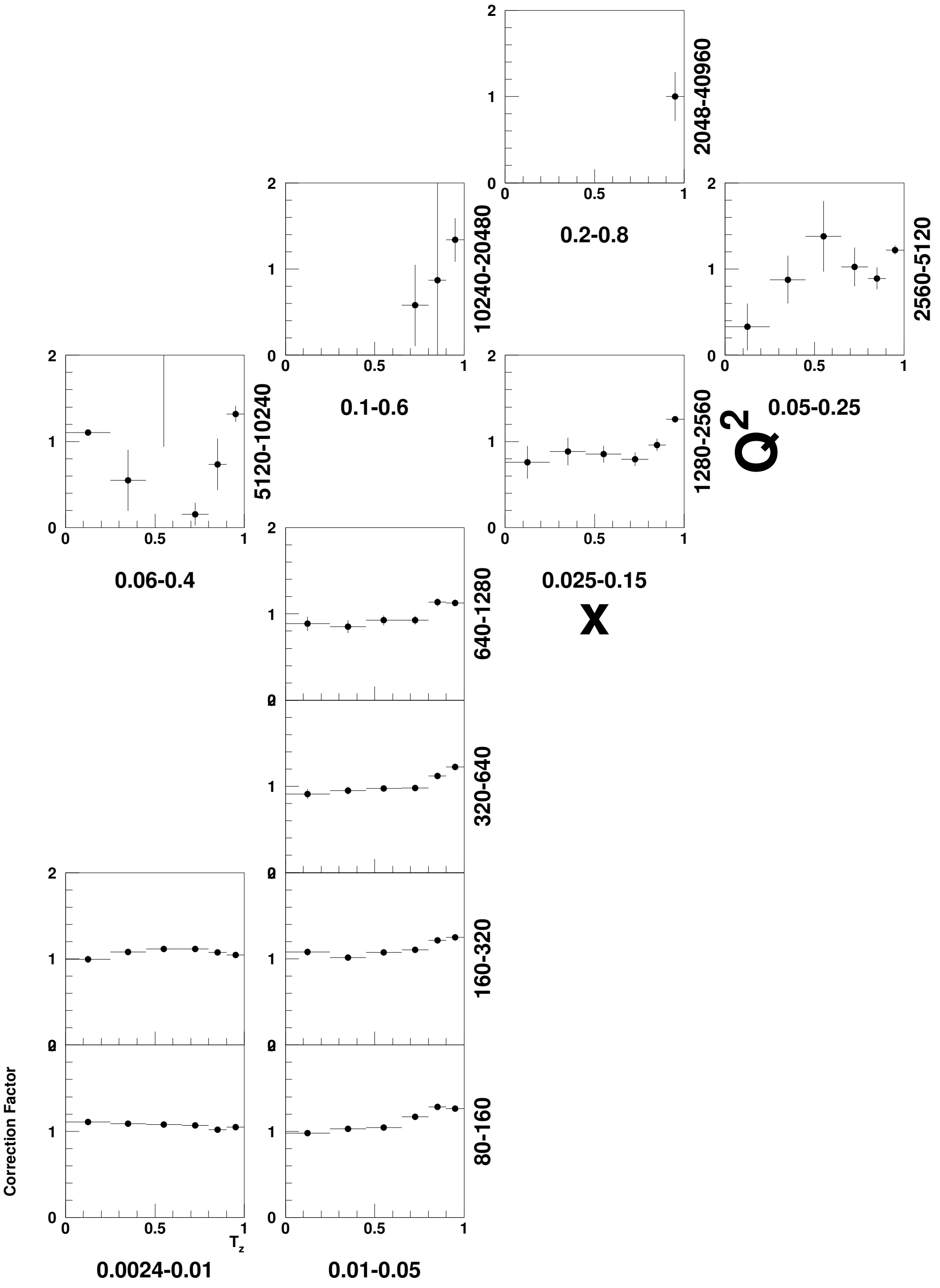

Figure 5.15: Correction Factors for thrust shown with the RMS value of the distribution. The Monte Carlo generator used was ARIADNE with the 1996 and 1997 detector simulation.

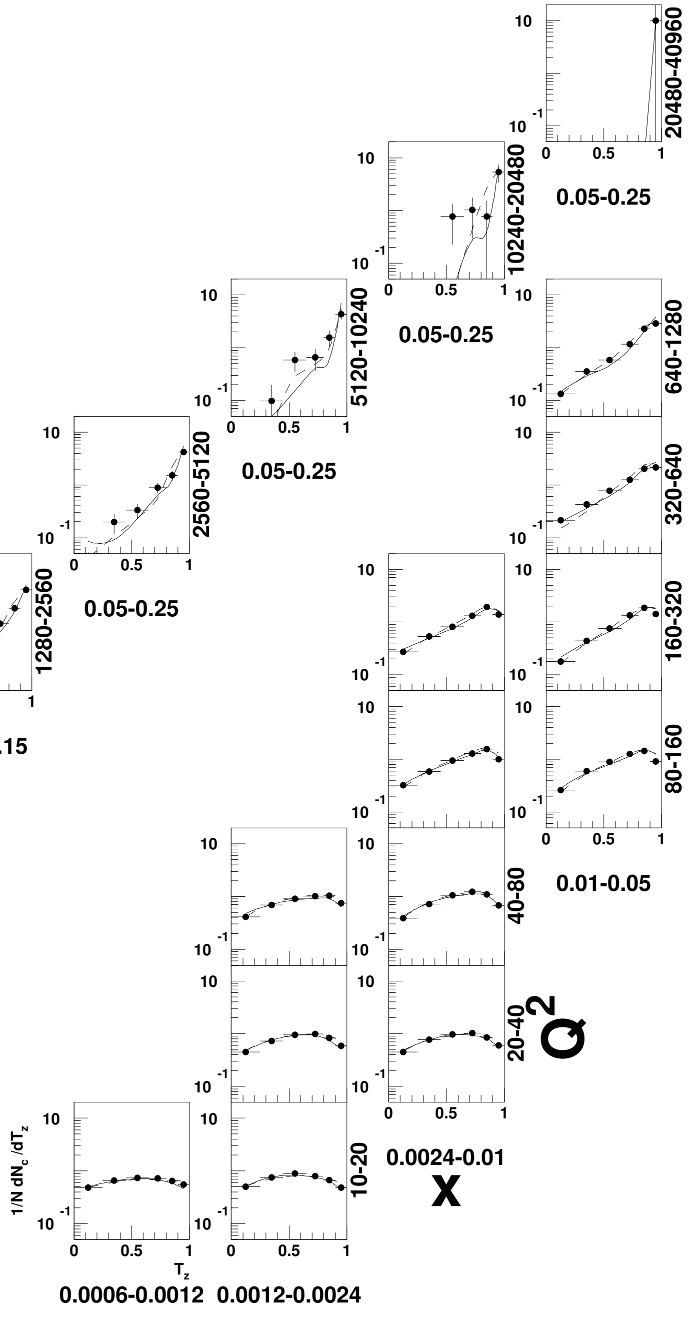

Figure 5.16: Reconstructed differential distribution of thrust for 1995 data (points) and the Monte Carlo event generator ARIADNE (solid line) and HERWIG (dashed line) using the 1995 detector simulation.

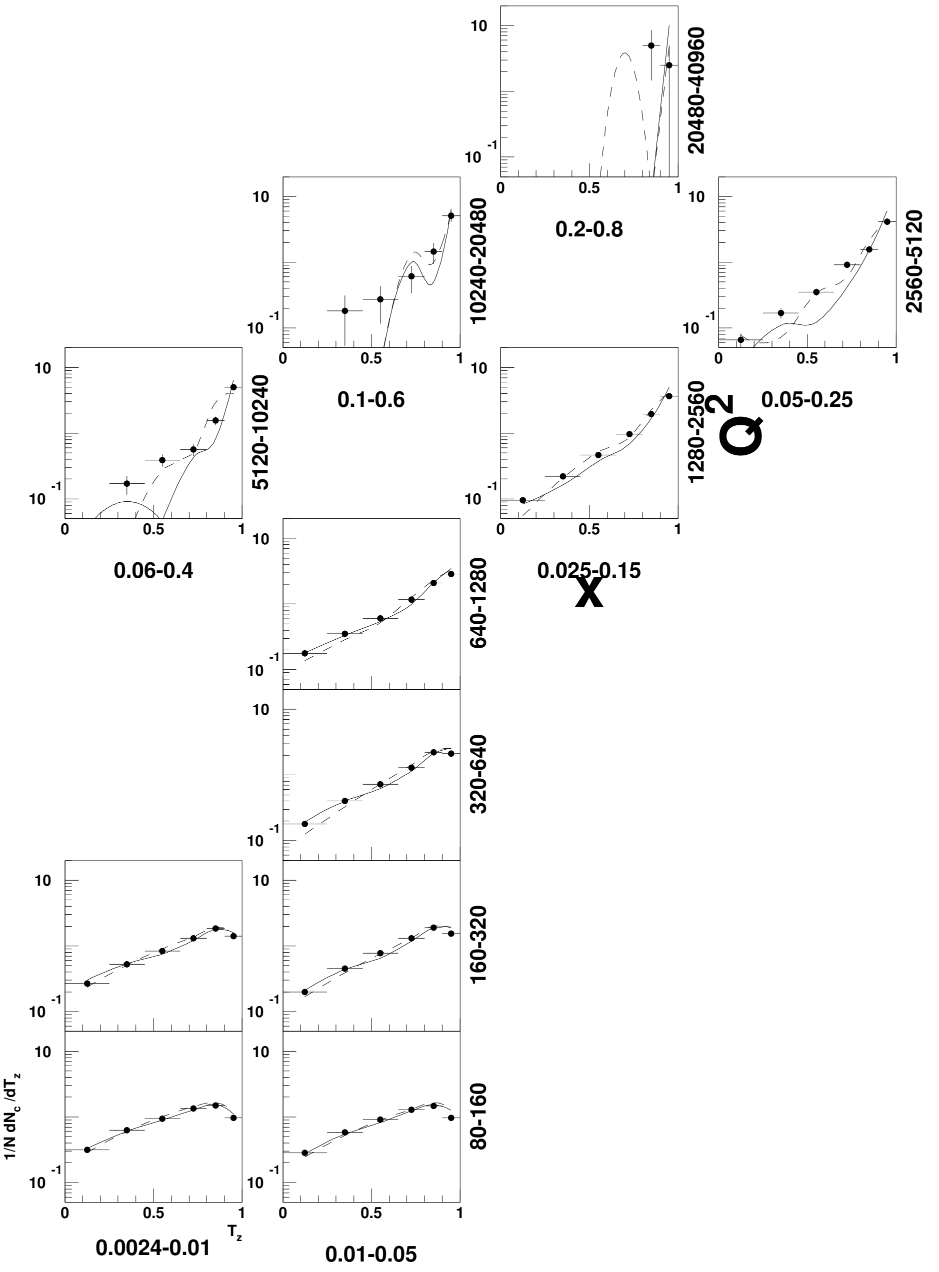

Figure 5.17: Reconstructed differential distribution of thrust for combined 1996 and 1997 data (points) and the Monte Carlo event generators ARIADNE (solid line) and HERWIG (dashed line) using the 1996 detector simulation.

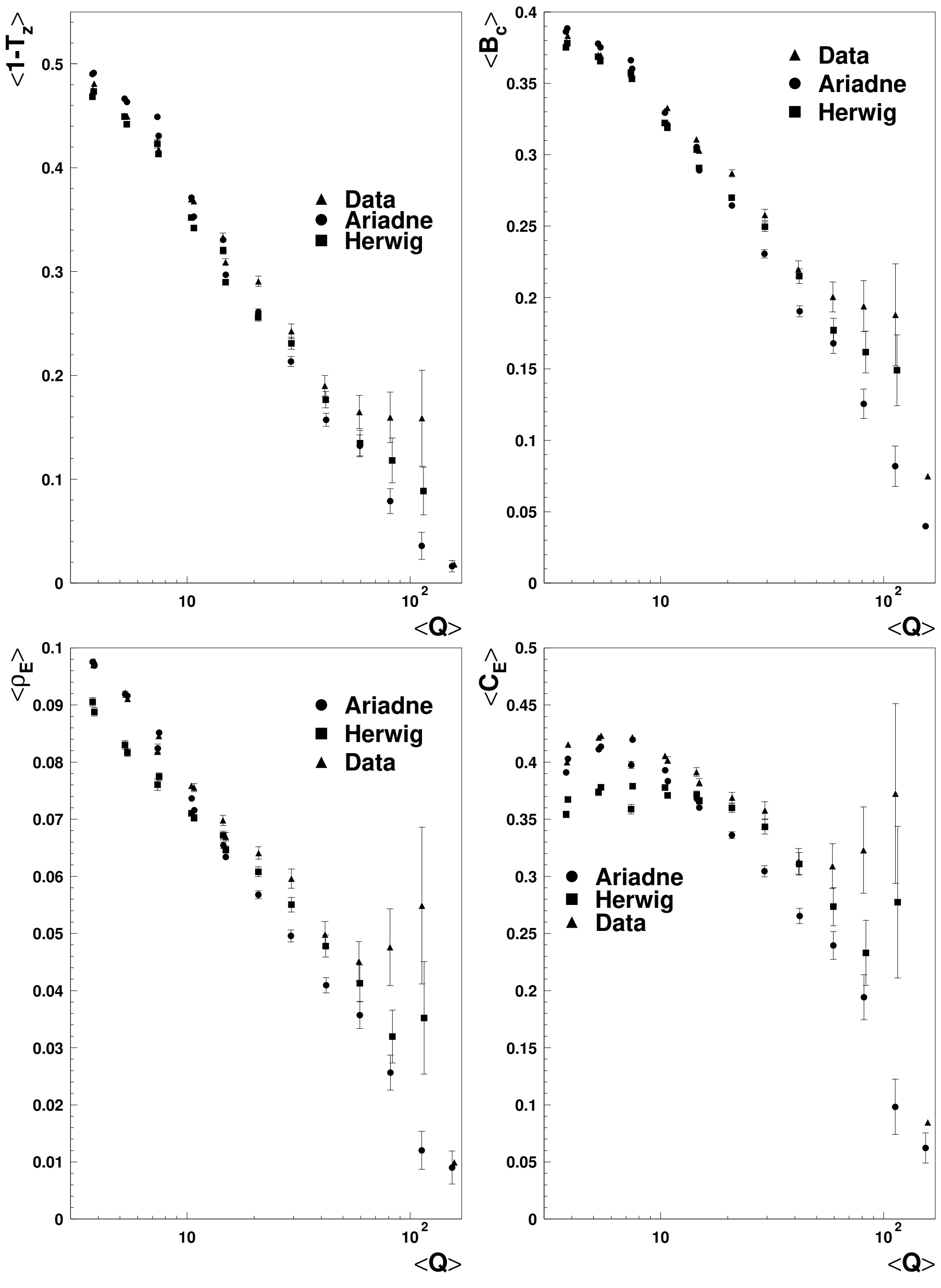

Figure 5.18: Reconstructed mean event shapes for 1995 data and the Monte Carlo event generator ARIADNE and HERWIG using the 1995 detector simulation.

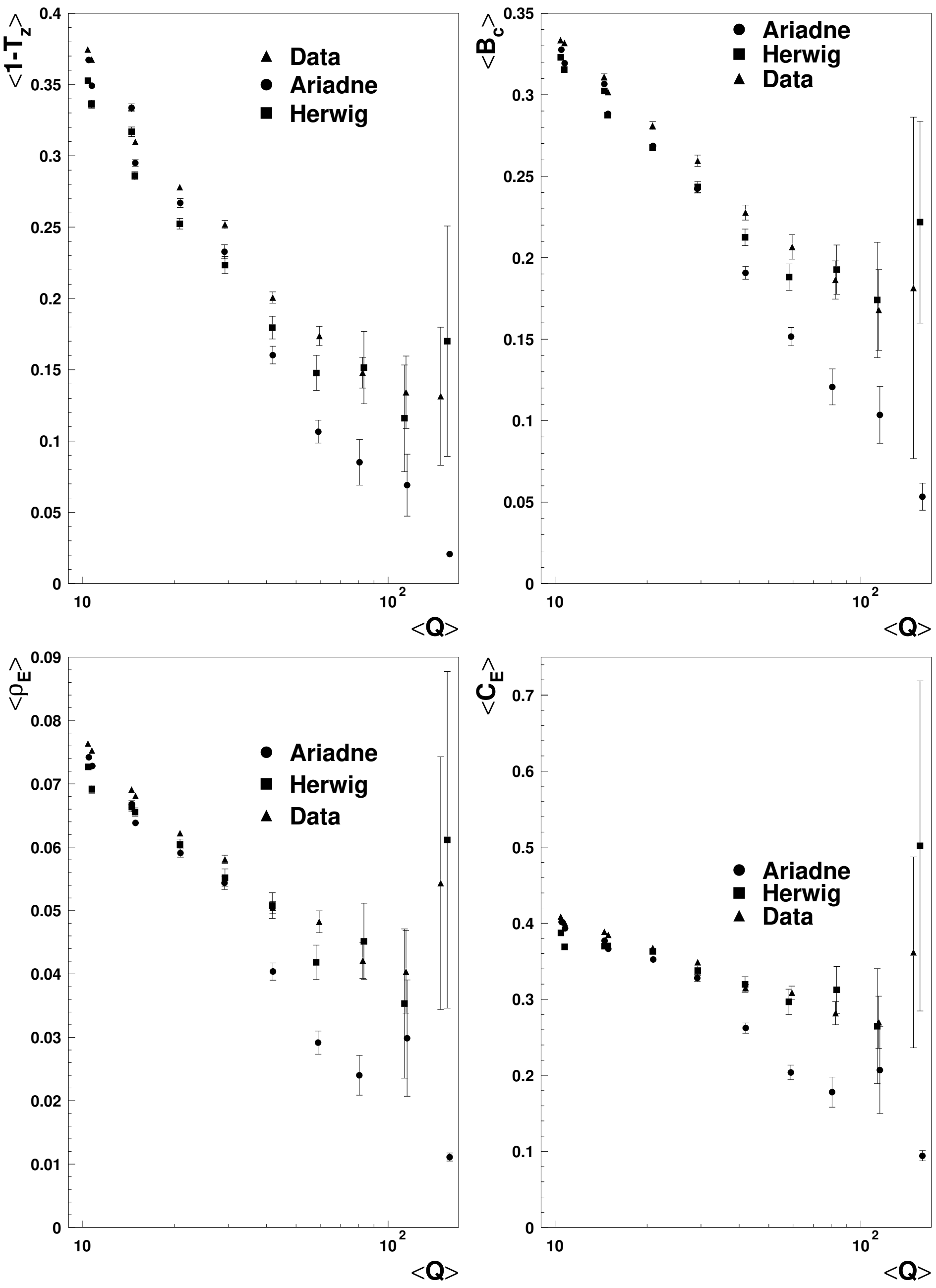

Figure 5.19: Reconstructed mean event shape as a function of mean Q for combined 1996 and 1997 data and the Monte Carlo event generator ARIADNE and HERWIG using the 1996 detector simulation.

similar discrepancy for that of thrust is observed for low jet broadening but this is not as pronounced for jet mass or the C parameter.

The reconstructed mean distributions for the 1995 MC agree within 4% of the reconstructed data for thrust for the majority of the kinematic range. The agreement for jet broadening is similarly as good for the lower 10 kinematic bins, above these the disagreement is slightly worse at 10-15%. The mean jet mass distributions also has discrepancies less than 5% for the first 10 kinematic bins and worsens to 10-20% for the remaining bins. The situation for the C parameter is similar with the agreement for the first 10 bins less than 5% and increasing after this.

The situation with the 1996 MC sample is the same except that the larger disagreements start around bin 12. Other than this fact the trends are the same.

Chapter 6

NLO Event Shapes

The purpose of this chapter is to introduce and define the parameters used in the production of the NLO predictions for the mean and differential event shape variables. The NLO Monte Carlo program used is DISENT. The phase space, parton density function and infrared safe cuts are defined and studies relating to the infrared cutoff are briefly presented.

The results from a high statistics evaluation are outlined. These results are then used to parameterise the NLO contributions to the mean event shape variable distributions as a function of $\Lambda_{QCD}^{[4]}$.

These parameterisations are then used in the extraction of the phenomenological constant, $\overline{\alpha_0}$, and the strong coupling constant, α_s, using a χ^2 minimisation technique. This is performed for all the event shape variables over a variable kinematic range to test the validity of the theory in different kinematic regions.

6.1 Input variables for DISENT

The first cuts applied to the DISENT program are the kinematic regions defined in the data analysis. The kinematic selection is detailed in section 3.3 and table 3.1; note also that the y range of 0.04 to 0.95 is also applied to relevant x and Q^2 regions. No other kinematic cuts were applied.

Another input value for the DISENT Monte Carlo is a parton density function. A parton density function was used which had been determined for several fixed values of the strong coupling constant, or alternatively $\Lambda^{[n]}_{QCD}$. The set of CTEQ 4 [52] parameterisations were used, specifically CTEQ 4A1, CTEQ 4A2, CTEQ 4A4 and CTEQ 4A5 which relate to $\Lambda^{[4]}_{QCD}$ values of 213, 253, 296, 344, and 399 MeV respectively; which correspond to α_S values of 0.110, 0.113, 0.116, 0.119 and 0.122 respectively. The $\overline{MS}$ renormalisation scheme is used for these parton density sets.

To obtain a numerically stable result from DISENT the results must be calculated from a reasonably high number of “points”. This is far more important for the high statistics lower Q^2 regions and thus for bin 1 to 8 the results are based on 10 million “points”, while the results from bins 9 to 12 are based on 5 million “points” and the remaining bins have results based on 1 million “points”.

6.2 NLO Energy Cut

In section 3.5 an energy threshold, applied to data, of 3% Q was determined. This ensures all events in the sample have defined values of the various event shape variables. A similar cut needs to be applied to the partons in the current region of the Breit frame to ensure the infra-red safeness of the partonic contributions.

The first response to such a requirement is to apply the same cut as applied to data. However, one needs to consider that the analysis is based on the measurement of event shape variables using only charged tracks. However, the parton level calculations given by DISENT, and other such programs, may assign a quark flavour to the partons but do not give the charge of the final hadron which a particular parton will evolve into. One could say that a particular fraction of the partons will turn into charged hadrons, say 2/3, so should the cut be applied to only 2/3 of the partons in the current region ? An upper limit would be a 4.5% cut on the total partonic energy.

To evaluate how the change from a 3% to 4.5% energy requirement will effect the NLO calculation given by DISENT the program was run for 10 different values of the cut (previously given the nomenclature n). In figure 6.1 the mean value of thrust ($\langle T_z \rangle$) for the kinematic bin 1 is given for a varying energy cut. The results show clearly that the NLO calculation does not depend greatly on the value of the cut when it is $\geq$ 3%. The change in mean thrust is less than 2% which is relatively small compared to the other uncertainties in the analysis. Therefore, the energy cut percentage used for both data and NLO calculation was 3%.

6.3 Mean And Differential NLO Distributions

In Figure 6.2 the NLO differential distribution of thrust (T_z) is shown. The figure is displayed in the same format as the data differential distributions. It can be seen that the NLO differential distribution exhibits a Q^2 dependence but one must view the corresponding mean distribution, shown in Figure 6.3, to appreciate the x dependence.

The NLO results shown in both Figure 6.2 and 6.3 were produced using

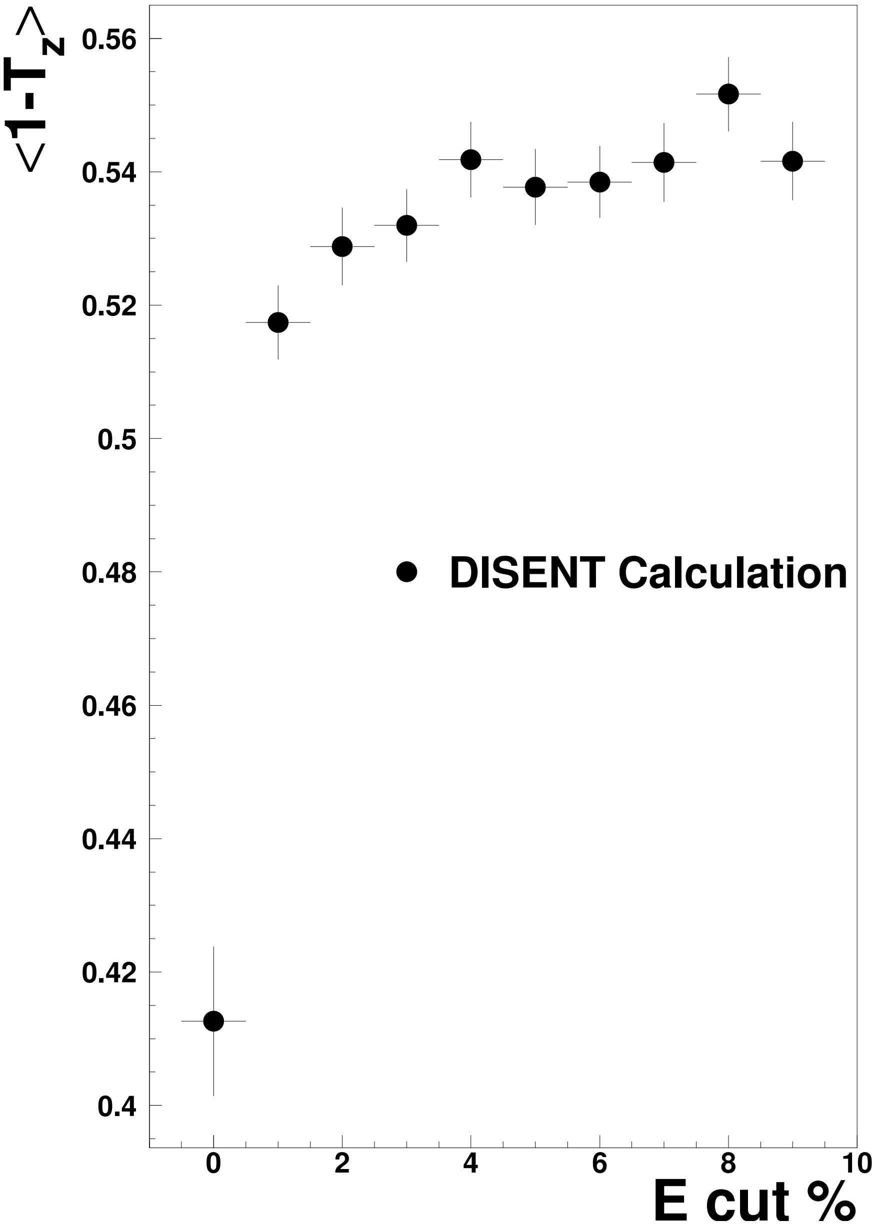

Figure 6.1: NLO prediction for mean thrust ($\langle T_z \rangle$) for kinematic bin 1 as a function of the energy requirement cut.

the CTEQ 4 A3 PDF set, which corresponds to a $\Lambda^{[4]}_{QCD}$ value of 296 MeV, and the energy cut applied was 3%. A particular feature of the differential distribution is the absence of the highest thrust bins. The values for these bins ($0.9 \leq T_z \leq 1.0$) are calculated but the results are not within the minimum and maximum range of the plot. The reason for this is the divergence of the cross section from collinear emissions. This produces a numerically unstable value in the highest thrust bin because the subtraction method, used by DISENT, does not cancel the collinear divergence totally.

6.4 NLO Mean Event Shape Fits

It is now necessary to return to the question of the PDF sets. Consider first the NLO contribution introduced in equation 2.26. It can be seen that both the NLO and the power correction contribution are dependent on α_s. Thus, if one wishes to fit α_s to the data, the dependence of the NLO contribution must be parameterised.

It is convenient, when discuss different values of the strong coupling constant, to instead use $\Lambda^{[n]}_{QCD}$ which is used directly in the DISENT code. The parton density function library routines [28] quote the strong coupling constant in this way, along with the renormalisation scheme used. For the CTEQ 4 parameterisations the value quoted is Λ_{QCD} for 4 active flavours, recalculated for 5 flavour when the scale is above the bottom mass. Empirically it is observed that, for an arbitrary mean event shape variable $\langle F \rangle$, the NLO contribution can be defined in terms of equation 6.1.

$$\langle F \rangle_{NLO} = m\Lambda^{[4]}_{QCD} + c \tag{6.1}$$

Where the two fitted coefficients m and c the NLO contribution to the mean event shape variable can be calculated for any value of $\Lambda^{[4]}_{QCD}$.

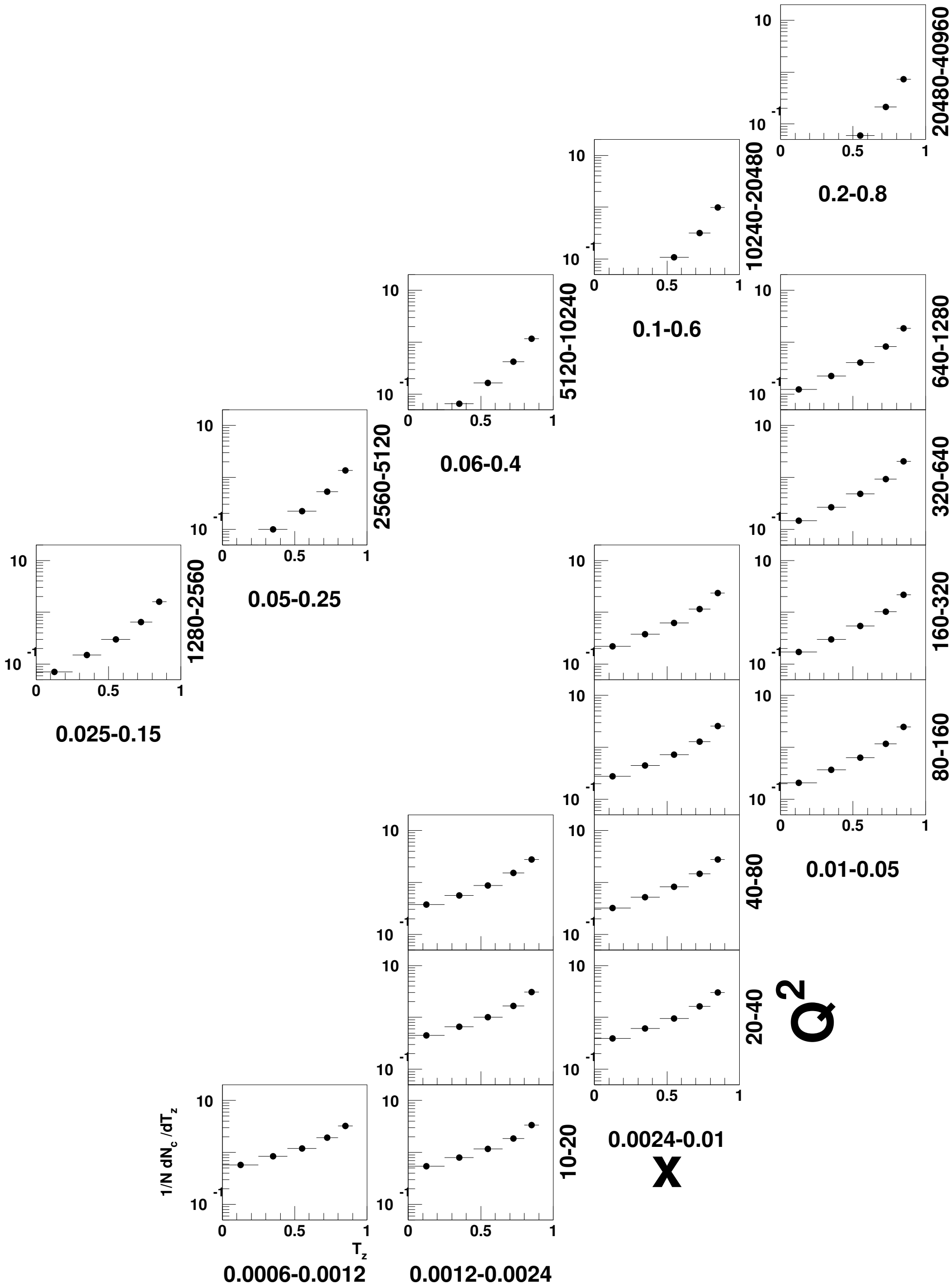

Figure 6.2: Next-to-leading order differential distribution of thrust (T_z) using the CTEQ 4 A3 PDF set ($\Lambda_{QCD}^{[4]} = 296$ MeV).

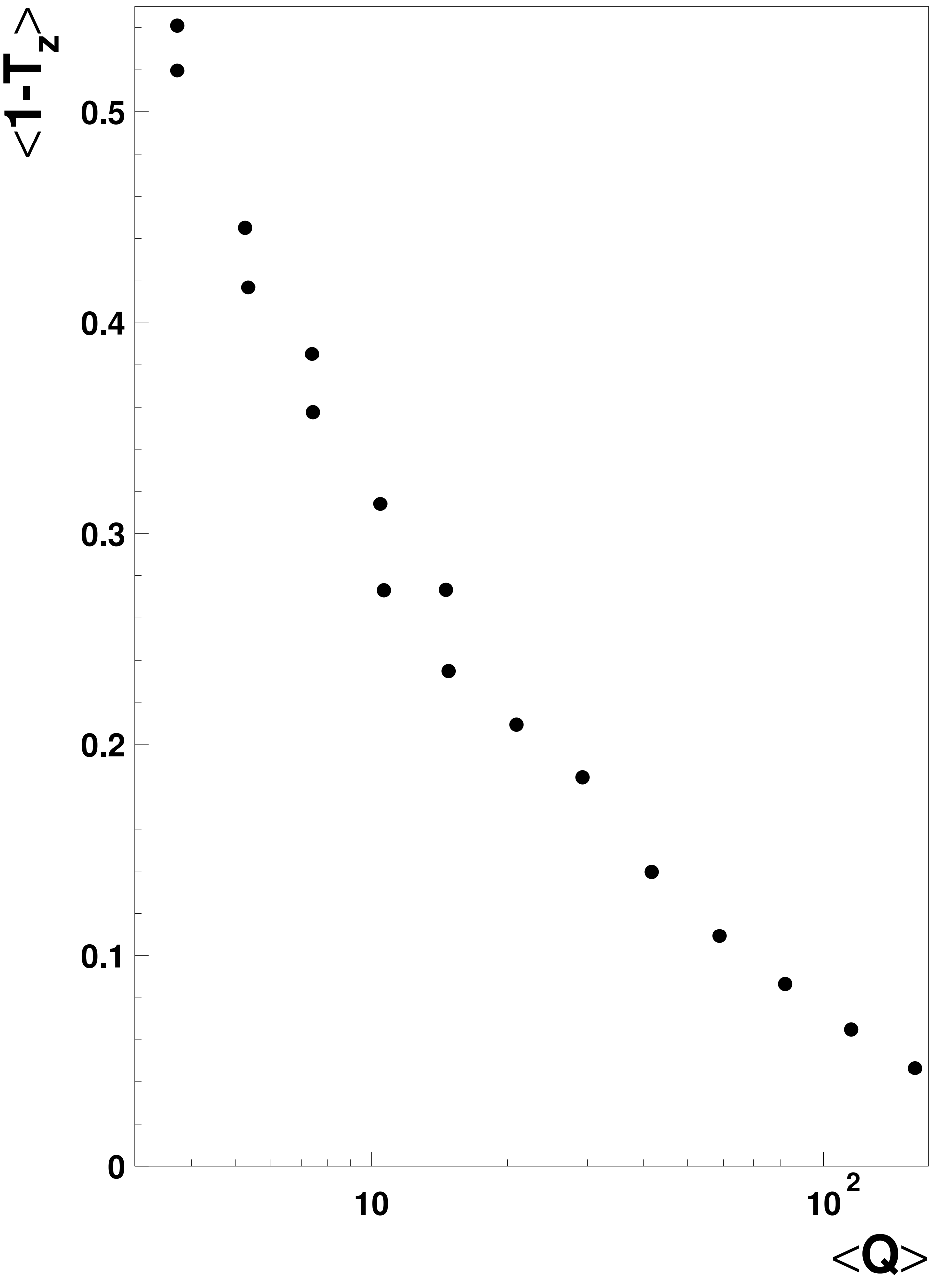

Figure 6.3: Next-to-leading order mean thrust (T_z) as a function of mean Q using the CTEQ 4 A3 PDF set ($\Lambda^{[4]}_{QCD} = 296$ MeV).

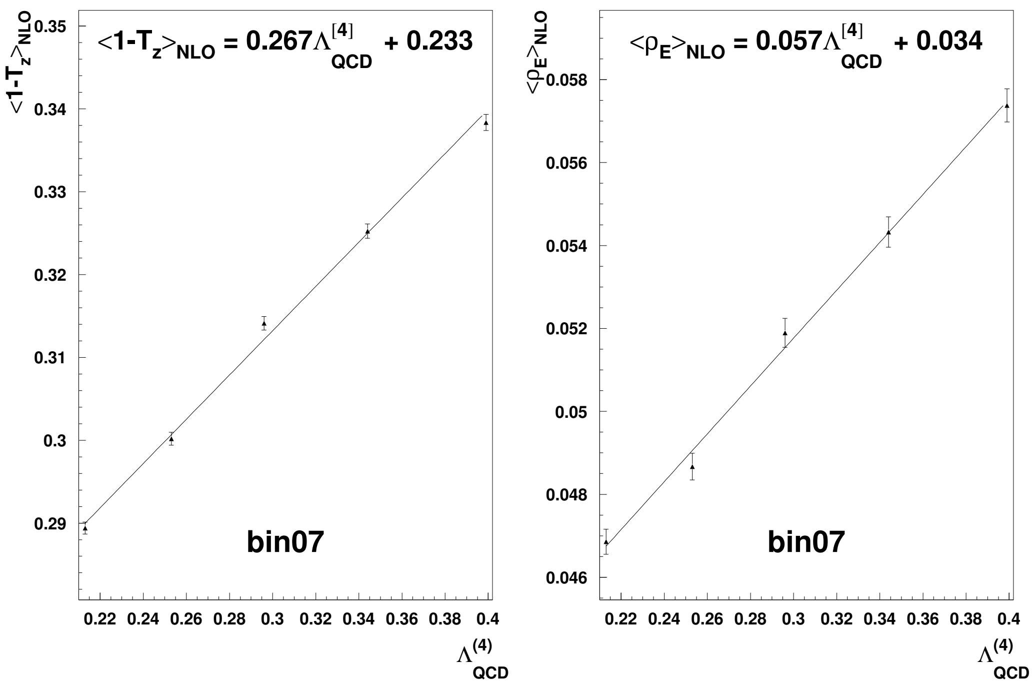

Figure 6.4: Linear fit to $\langle 1 - T_z \rangle$ and $\langle \rho_E \rangle$ in bin 7, from the DISENT NLO Monte Carlo generator, for 5 different parton density function with differing $\Lambda^{[4]}_{QCD}$.

An example of two of these fits, for thrust and jet mass, are shown in figure 6.4. Results of fitted coefficients for each of the four event shape variables, from equation 6.1, are shown in table 6.1 to 6.4. Included in this table are the χ^2/NDF for each of the fits. For the majority of the bins for all the event shape variables the fits are very good (i.e. with $\chi^2/\text{NDF} < 1$). The only possible exception is the lowest two kinematic bins. This would imply a small uncertainty is introduced by the parameterisation into the power correction fits discussed in Chapter 9.

Bin	T_z		
number	m	c	χ^2/ndf
1	0.92 ±0.02	0.269 ±0.005	11.68/4
2	0.86 ±0.01	0.270 ±0.004	10.73/4
3	0.59 ±0.01	0.273 ±0.003	5.08/4
4	0.50 ±0.01	0.268 ±0.003	0.10/4
5	0.39 ±0.01	0.271 ±0.003	1.50/4
6	0.36 ±0.01	0.252 ±0.002	0.83/4
7	0.27 ±0.01	0.233 ±0.002	2.92/4
8	0.228±0.004	0.204 ±0.001	8.81/4
9	0.196±0.007	0.214 ±0.002	1.40/4
10	0.167±0.005	0.184 ±0.001	1.99/4
11	0.138±0.004	0.167 ±0.001	3.82/4
12	0.111±0.003	0.151 ±0.001	3.69/4
13	0.079±0.003	0.116 ±0.001	0.79/4
14	0.066±0.002	0.0889±0.0007	2.33/4
15	0.052±0.002	0.0710±0.0008	1.73/4
16	0.040±0.002	0.0530±0.0007	0.57/4
17	0.027±0.002	0.0385±0.0007	0.07/4

Table 6.1: Table of fitted coefficients to the NLO thrust (T_z) predictions from the DISENT Monte Carlo.

Bin number	B_c		
	m	c	χ^2/ndf
1	-0.17 ±0.02	0.252 ±0.007	2.56/4
2	-0.07 ±0.02	0.247 ±0.006	2.44/4
3	0.08 ±0.02	0.230 ±0.005	1.60/4
4	0.10 ±0.01	0.240 ±0.004	0.62/4
5	0.07 ±0.01	0.232 ±0.004	0.26/4
6	0.13 ±0.01	0.228 ±0.003	0.18/4
7	0.124±0.009	0.218 ±0.003	3.47/4
8	0.143±0.006	0.212 ±0.002	2.42/4
9	0.11±0.01	0.207 ±0.003	0.86/4
10	0.116±0.007	0.202 ±0.002	1.14/4
11	0.108±0.006	0.188 ±0.002	1.61/4
12	0.104±0.005	0.173 ±0.002	0.42/4
13	0.090±0.005	0.149 ±0.001	0.57/4
14	0.081±0.003	0.128 ±0.001	1.34/4
15	0.070±0.003	0.1104±0.0009	1.89/4
16	0.057±0.004	0.093 ±0.001	1.35/4
17	0.050±0.004	0.074 ±0.001	0.16/4

Table 6.2: Table of fitted coefficients to the NLO jet broadening (B_c) predictions from the DISENT Monte Carlo.

Bin number	ρ_E		
	m	c	χ^2/ndf
1	0.092±0.007	0.032 ±0.002	2.56/4
2	0.103±0.006	0.033 ±0.002	1.21/4
3	0.087±0.004	0.033 ±0.001	1.75/4
4	0.082±0.005	0.037 ±0.001	0.21/4
5	0.062±0.005	0.036 ±0.001	0.19/4
6	0.069±0.003	0.0361±0.0009	0.95/4
7	0.058±0.002	0.0345±0.0007	0.89/4
8	0.056±0.002	0.0364±0.0005	4.46/4
9	0.046±0.003	0.0340±0.0009	1.05/4
10	0.043±0.002	0.0352±0.0006	0.25/4
11	0.038±0.002	0.0327±0.0005	1.60/4
12	0.033±0.001	0.0302±0.0004	1.89/4
13	0.026±0.002	0.0283±0.0005	0.41/4
14	0.022±0.001	0.0253±0.0003	1.09/4
15	0.018±0.001	0.0226±0.0004	1.45/4
16	0.016±0.001	0.0191±0.0003	0.50/4
17	0.011±0.001	0.0157±0.0003	0.16/4

Table 6.3: Table of fitted coefficients to the NLO jet mass (ρ_E) predictions from the DISENT Monte Carlo.

Bin number	C_E		
	m	c	χ^2/ndf
1	0.62 ±0.04	0.23± 0.01	0.29/4
2	0.69 ±0.04	0.22± 0.01	0.41/4
3	0.54 ±0.03	0.220±0.008	0.31/4
4	0.54 ±0.02	0.236±0.007	0.81/4
5	0.41 ±0.02	0.226±0.007	1.14/4
6	0.47 ±0.02	0.219±0.006	3.26/4
7	0.35 ±0.02	0.225±0.005	0.79/4
8	0.39 ±0.01	0.221±0.003	1.48/4
9	0.34 ±0.01	0.204±0.004	1.22/4
10	0.31 ±0.01	0.216±0.003	1.29/4
11	0.255±0.008	0.205±0.002	1.67/4
12	0.224±0.007	0.192±0.002	2.58/4
13	0.172±0.004	0.186±0.001	3.30/4
14	0.154±0.003	0.169±0.001	4.36/4
15	0.234±0.003	0.129±0.001	4.12/4
16	0.118±0.003	0.1354±0.0008	1.19/4
17	0.087±0.003	0.1190±0.0008	0.5/4

Table 6.4: Table of fitted coefficients to the NLO C parameter (C_E) predictions from the DISENT Monte Carlo.

Chapter 7

Results

In this chapter corrected differential and mean event shape distributions are presented. Systematic studies relating to the data analysis are introduced and the effect on the distributions presented and described. The combination of the systematic studies relating to different years data are described and subsequently combined 1995, 1996 and 1997 data are presented. The differential distributions are presented in two forms, first as a function of thrust (T_z) and second as a function of Q^2. The mean event shape distributions are shown as a function of $\langle Q \rangle$.

7.1 Differential and Mean Distributions

The corrected thrust (T_z) differential distributions for the 1995 and 1996-97 data sample are shown in Figure 7.1 and 7.2 respectively. The data were corrected using the ARIADNE MC event generator which used the MRS A' PDF set (see Table 4.1). Each year's data used the relevant detector simulation[1]

The 1995 and 1996-97 corrected data show a clear Q^2 dependence. An x dependence in the distributions cannot be clearly seen but inspection of the mean distributions, shown in Figure 7.3, indicated that one exists.

Another plot of the 1995 data which helps distinguish the x dependence in the differential distributions is shown in Figure 7.4. This figure presents the differential distributions as a function of Q^2 for a specific thrust range. The plot includes several points at the same Q^2 but with differing x range (see key in bottom right plot). This distribution shows a decrease in cross section with increasing Q^2 for the lower thrust bins. The medium thrust bins show a generally flat distribution over the whole Q^2 region while the higher thrust bins show a clear increase with increasing Q^2. It can also be seen from these points that an x dependence exists in the corrected differential distributions.

To ensure that each year's data is consistent, the ratio of the corrected differential event shape distributions for the 1995 and combined 1996-97 samples are calculated. Figure 7.5 shows the ratio for the thrust distribution as a function of thrust for the 11 overlapping kinematic bins. The ratio of the data shows a good agreement within the errors over the majority of the kinematic overlap (similar agreement is observed for the other event shapes).

7.2 Systematic Studies Of Data Analysis

The corrected points presented in the previous section are subject to further uncertainty, not solely of a statistical nature. The process of obtaining a

---

[1] The 1997 data were corrected using the 1996 MC sample since the detector did not change during the 1996-1997 shutdown period.

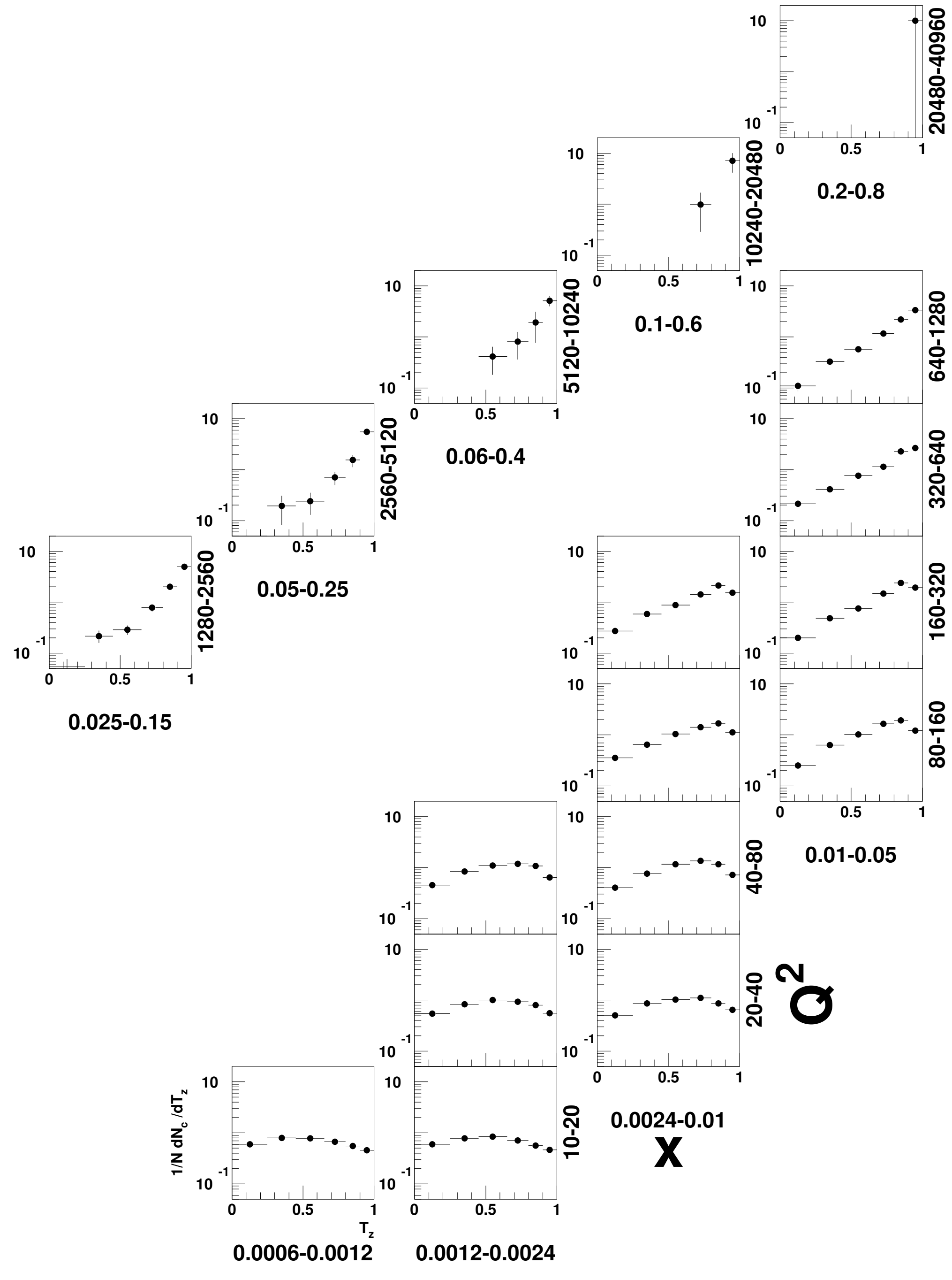

Figure 7.1: Corrected thrust distribution for 1995 data.

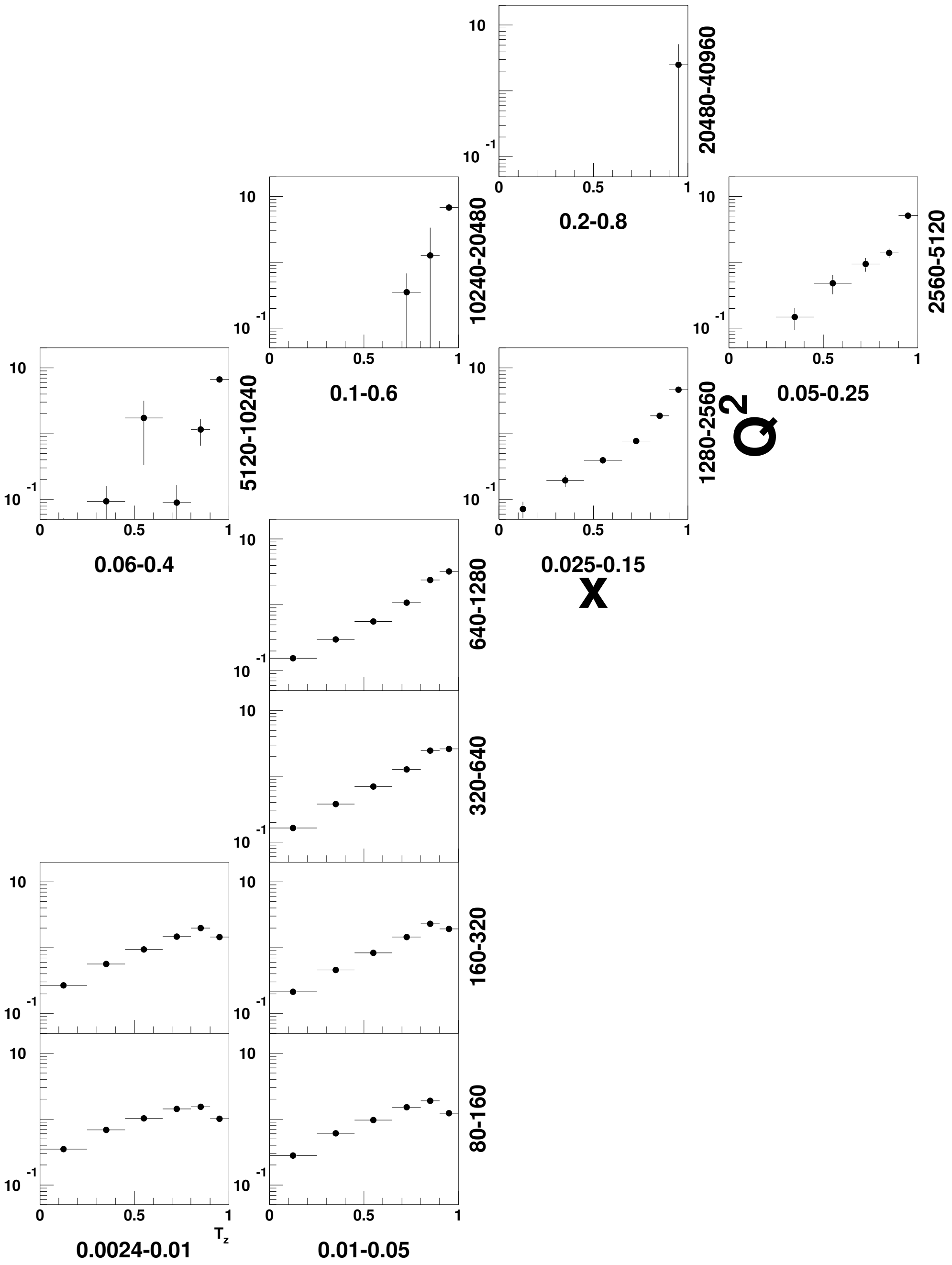

Figure 7.2: Corrected thrust distribution for combined 1996 and 1997 data.

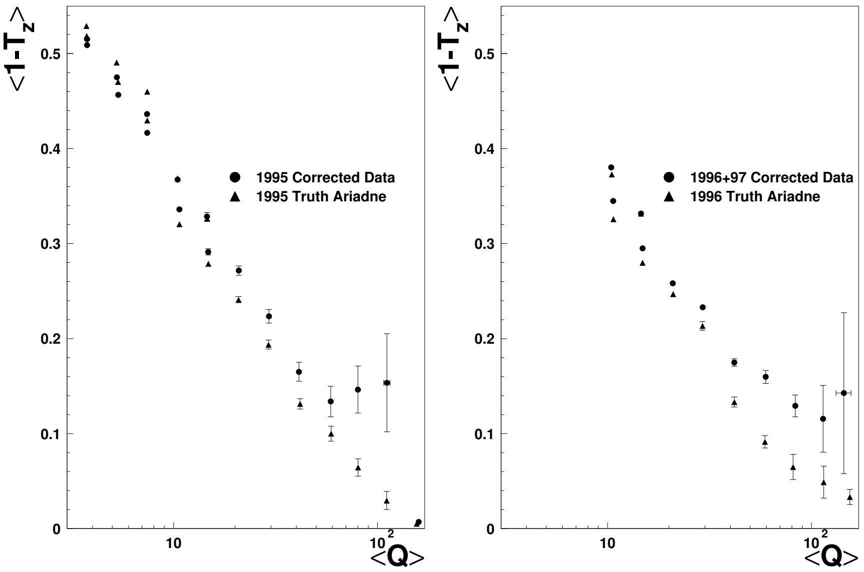

Figure 7.3: Corrected 1995 and 1996-97 mean thrust ($\langle T_Z \rangle$) distributions as a function of mean Q shown with the ARIADNE hadron level results.

sufficiently pure sample of DIS events requires a certain amount of selection criteria, discussed in Section 3.3. These selection criteria were in the form of cuts on experimental observable which have an uncertainty associated with them. In addition to these uncertainties, additional ones are introduced in the process of correcting the data.

The systematic studies of the data, in this case, can be separated into studies based on reconstruction and selection criteria and also into studies based on track reconstruction and selection criteria. The process of adjusting these selection criteria within their respective uncertainties must be undertaken and the effect on the corrected data evaluated. These systematic uncertainties are evaluated along with the statistical errors of the corrected data.

Each study is carried out individually and the final changes in measure-

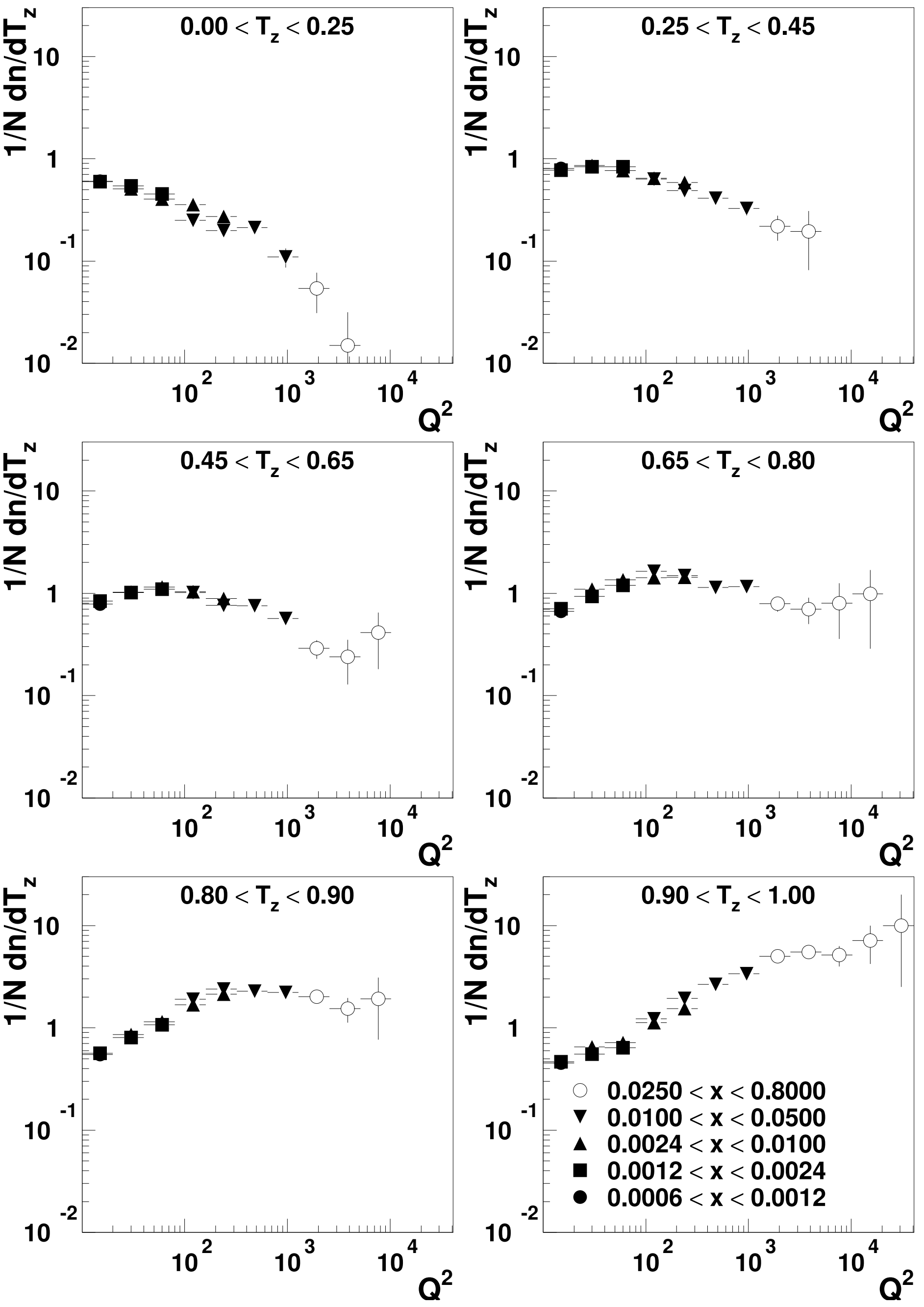

Figure 7.4: Corrected thrust distribution for 1995 data shown as a function of Q^2. The highest x range points have variable sized x intervals.

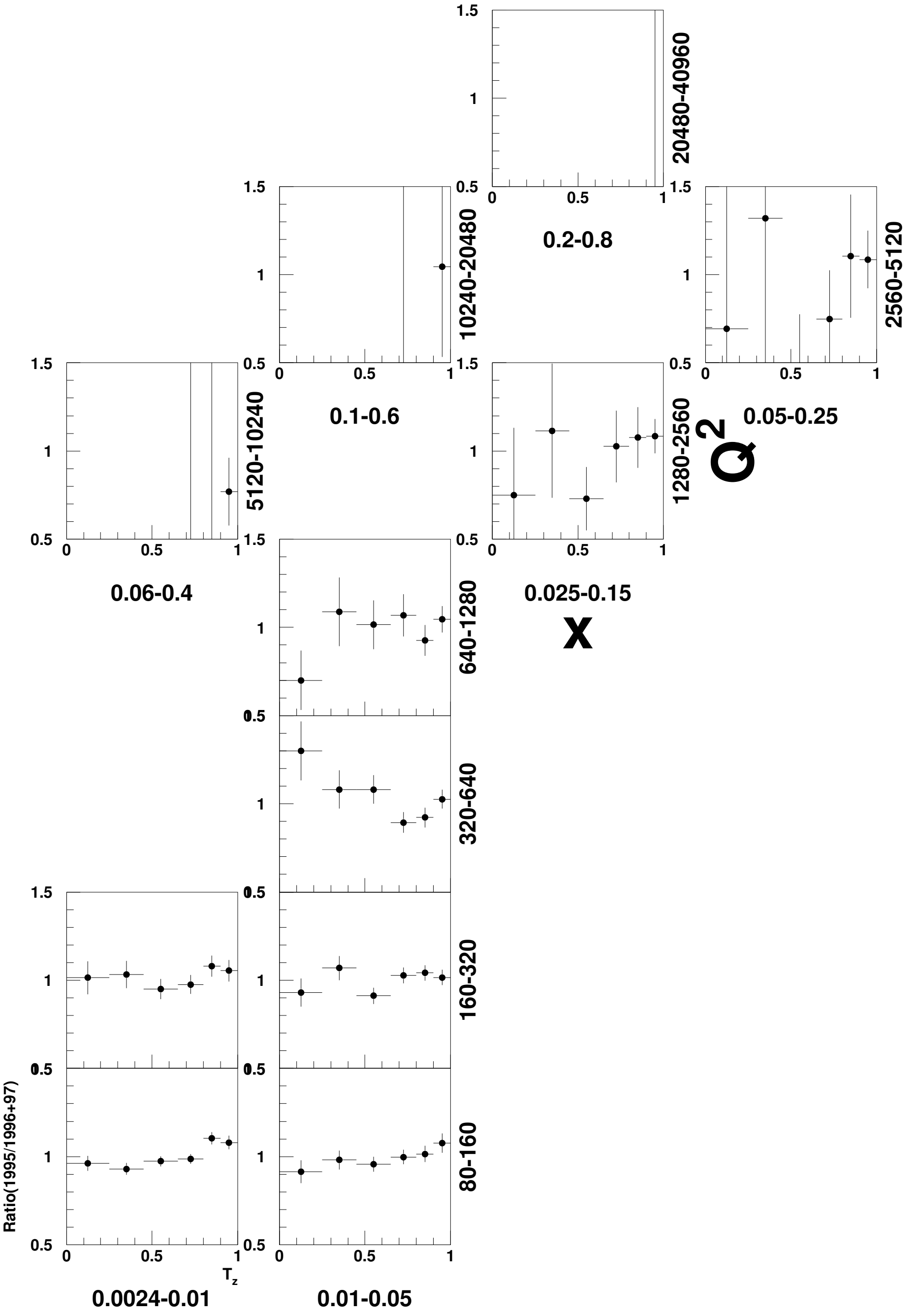

Figure 7.5: Ratio of 1995 and 1996+97 corrected thrust distribution, as a function of thrust, for the 11 overlapping kinematic bins.

ments combined in quadrature to produce the uncertainty in the measured quantity (i.e differential or mean distribution points).

7.2.1 Event Reconstruction and Selection Systematics

The event selection and reconstruction criteria were altered and the corrected differential and mean distributions recalculated. The following studies were performed (nominal values are shown in brackets):

- The lower cut for $\sum_{\text{Total}} E - P_z$ is changed to 40 (35) GeV;

The differential distributions for all the event shape variables over the majority of the kinematic range demonstrate only a small systematic change, of the order 1-3%. This change is the same size or smaller than the statistical errors for these points and there is no systematic direction for the shift. A small number of bins have larger shifts of 10-20% but this is of the same order as the statistical accuracy.

As may be concluded from the differential distributions the mean values for all event shapes change by very little, for most bins by less than 1 or 2%. For the highest 2 bins, shifts of 10% are observed but all are well within statistical accuracy.

- the y_{JB} cut is raised to 0.05 (0.04);

The y_{JB} systematic distributions, for all the event shape variables, demonstrate only small shifts of $\sim 1\%$ for the majority of the bins. Some bins are more affected, those which are intersected by the cut (i.e. 2, 4 and 8), and show larger deviations of 2-3%. However, the systematic shifts are of the same order, or only slightly larger, than the statistical errors.

The mean values for all the event shapes shift by less than 0.1%, except for the previously listed bins which have 1-3% shifts towards higher values of $\langle 1 - T_z \rangle$ and $\langle B_c \rangle$ and towards lower values of $\langle \rho_E \rangle$ and $\langle C_E \rangle$.

- the y_e cut is lowered to 0.8 (0.95).

This systematic change produces very little change in the differential distributions for bins 1 to 12, this is where the y_e cut has very little effect. The shifts are less than 0.5%. However, for bins 13 to 17 shifts around 5%, but up to 20%, are produced but this is still less than the statistical errors on these points.

The mean values for all the event shapes show no real sensitivity to the y_e cut. Only the highest kinematic bins showed any change, with shifts of 10-20%. This is far less than the statistical accuracy.

7.2.2 Data Correction Systematics

Correcting the data using a different MC event generator should evaluate the model dependence of the corrected data. As the analysis presented in this thesis requires the detector response to hadrons to be determined, it is important to compare at least two MC event generators which use different hadronisation models.

- the data are corrected using HERWIG (ARIADNE) event generator.

This change produces by far the largest of all those studied. When correcting the data using HERWIG, the differential distributions for the lowest two kinematic bins exhibit a large (20-30%) positive shift at both high and low values of thrust and jet broadening. For the higher kinematic bins the situation is similar but with only large (10-20%) negative shifts at high (low) values of thrust (jet broadening).

In the case of the C parameter most kinematic bins show large (20-50%) positive shifts at high values. The differential distributions for jet mass show large systematic shifts for certain points (∼10%) but with no general trend.

The effect of this systematic study is just as significant on the mean distributions. The mean values for both thrust and jet broadening are increased by 1% to 18% for the central x and Q^2 region. The lower kinematic bins do not change greatly and the higher bins are dominated by large statistical uncertainties. The situation for jet mass and the C parameter is less serious. Variations of 1-2% are observed but with no particular systematic direction.

7.2.3 Track Reconstruction And Selection Systematics

The track selection and reconstruction criteria were altered and the corrected differential and mean distributions recalculated. The following studies were performed (nominal values are shown in brackets):

- the η cut is relaxed to 2.0 (1.75);

The increase of the η selection on tracks does not change the differential event shape distributions by a significant amount (less than 0.3%). The higher kinematic bins show larger shifts of 5-10%. Subsequently the mean event shape distributions are not greatly changed for the entire kinematic region.

- the $P_\perp$ cut is relaxed to 0.1 (0.2) GeV;

The loosening of the transverse momentum cut does not change the event shape variable differential distributions significantly. The shifts are $\sim 0.3\%$ for most of the kinematic range. A small number of the higher kinematic bins exhibit larger shifts for both jet mass and the C parameter, mainly in points containing only a few events. Thus, for these variables the inclusion of additional tracks will change there value and the distribution greatly. The mean distributions for the events shapes exhibit less than a 1% change.

- non-vertex fitted tracks are used (vertex fitted).

The inclusion of the non-vertex fitted tracks produces the largest change of the tracking systematic studies. The differential distributions for thrust, jet broadening and jet mass have shifts of between 1 and 5 % for the majority of the kinematic bins. Larger shifts are seen in the higher kinematic bins but no overall direction for the shifts are seen. The C parameter differential distribution in some kinematic bins exhibit large shifts (∼10-40%) for the highest C_E bin, in both positive and negative directions.

The mean distributions, however, show little sensitivity to these systematic changes over the majority of the kinematic range. The higher $\langle Q \rangle$ points show systematic shifts to lower values of event shapes, except in the case of thrust where it is higher.

7.3 Systematic Distributions

Each systematic difference is considered separately and added in quadrature, with positive and negative shifts combined separately. In Figure 7.6 to 7.9 the 1995 differential distributions for all four event shapes are shown. They include statistical error bars as the inner ticks, and combined statistical and systematic as the outer error lines. The dominant systematic for the event shapes differential distributions is the MC hadronisation model dependence.

In Figure 7.10 the mean event shape distributions are shown, again the inner ticks are the statistical errors and the outer lines the statistical errors

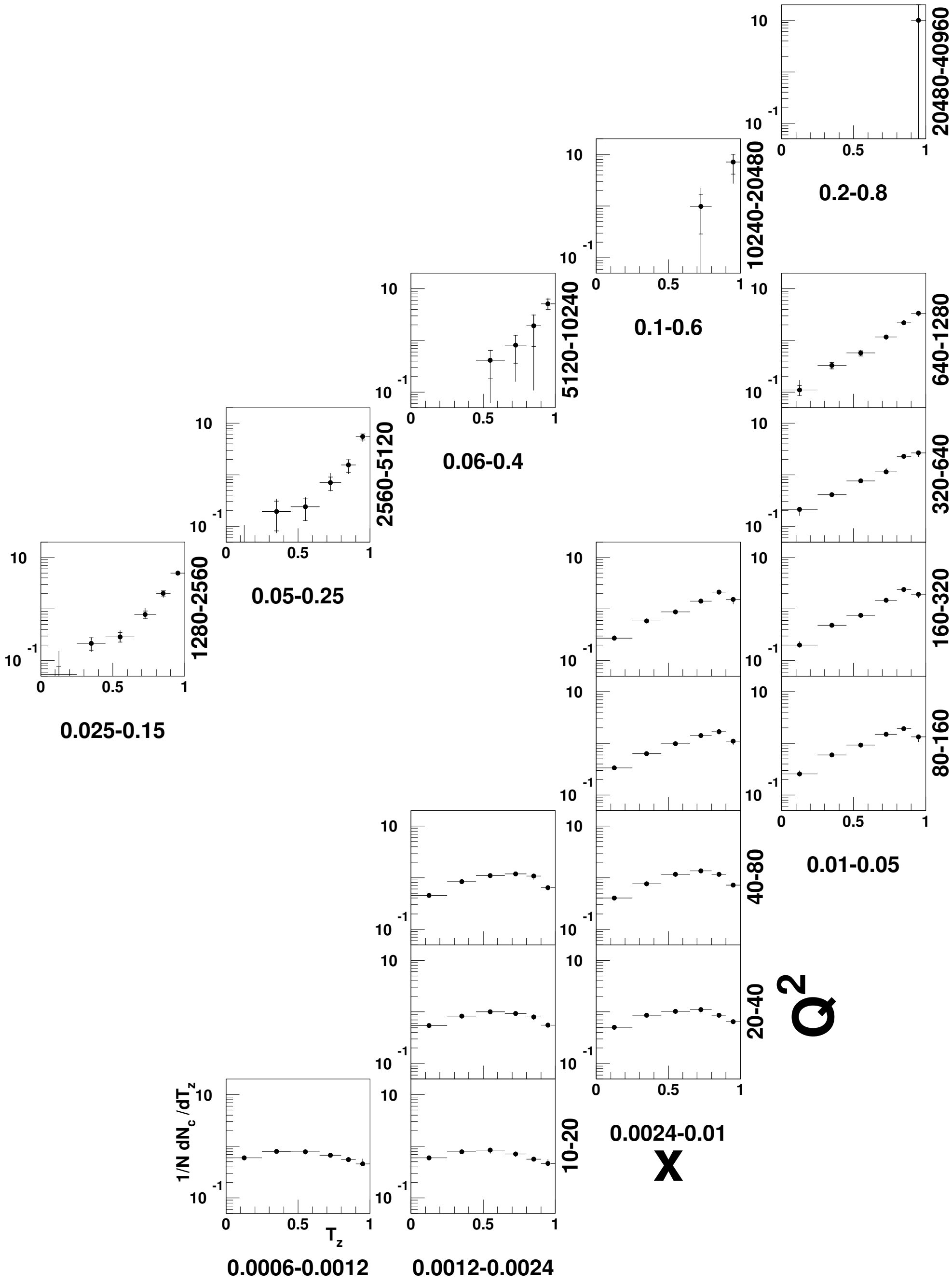

Figure 7.6: Corrected thrust distribution for 1995 data with systematic errors included. The inner error bars are statistical only with the outer as systematic and statistical combined in quadrature.

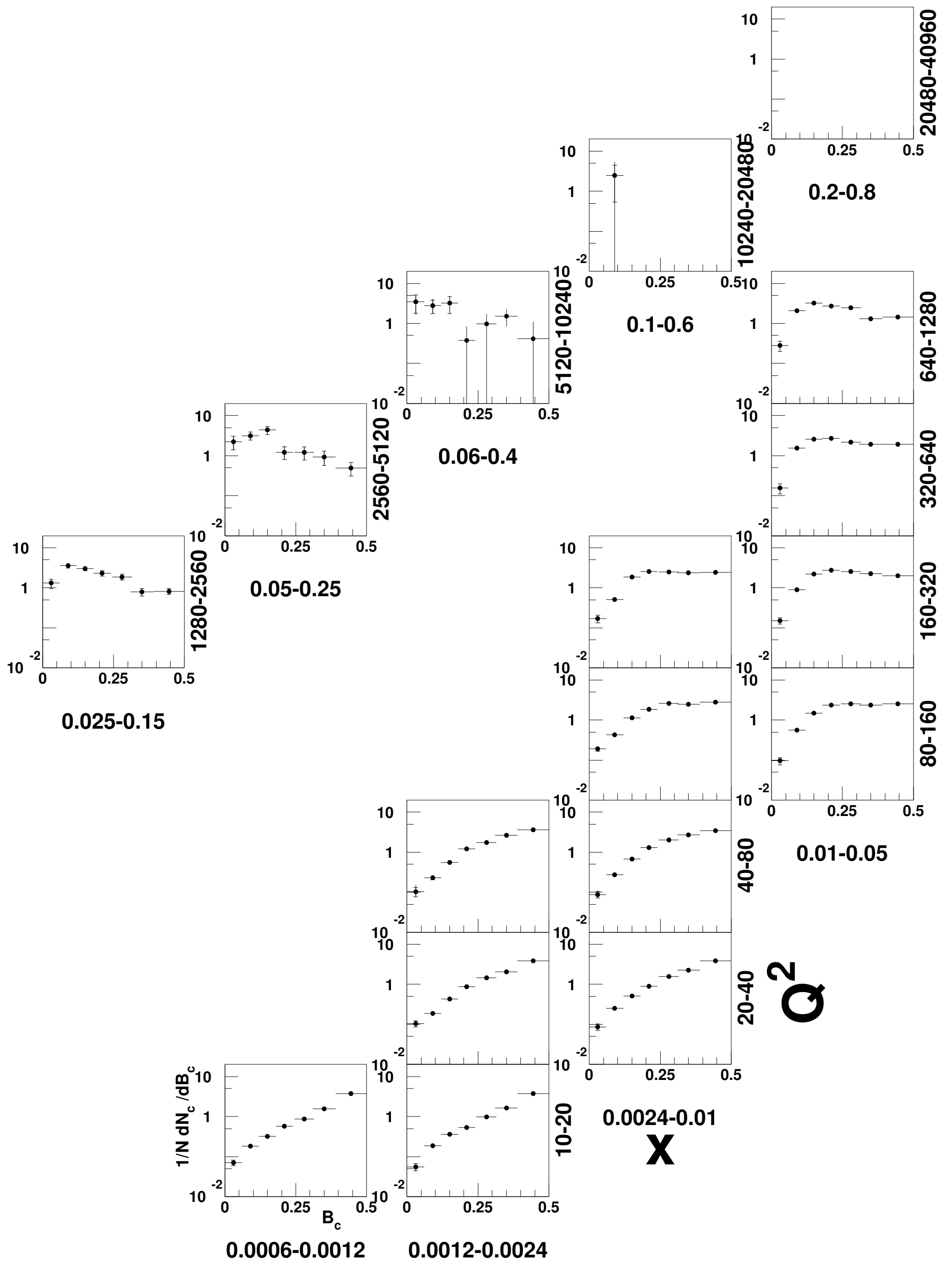

Figure 7.7: Corrected jet broadening distribution for 1995 data with systematic errors included. The inner error bars are statistical only with the outer as systematic and statistical combined in quadrature.

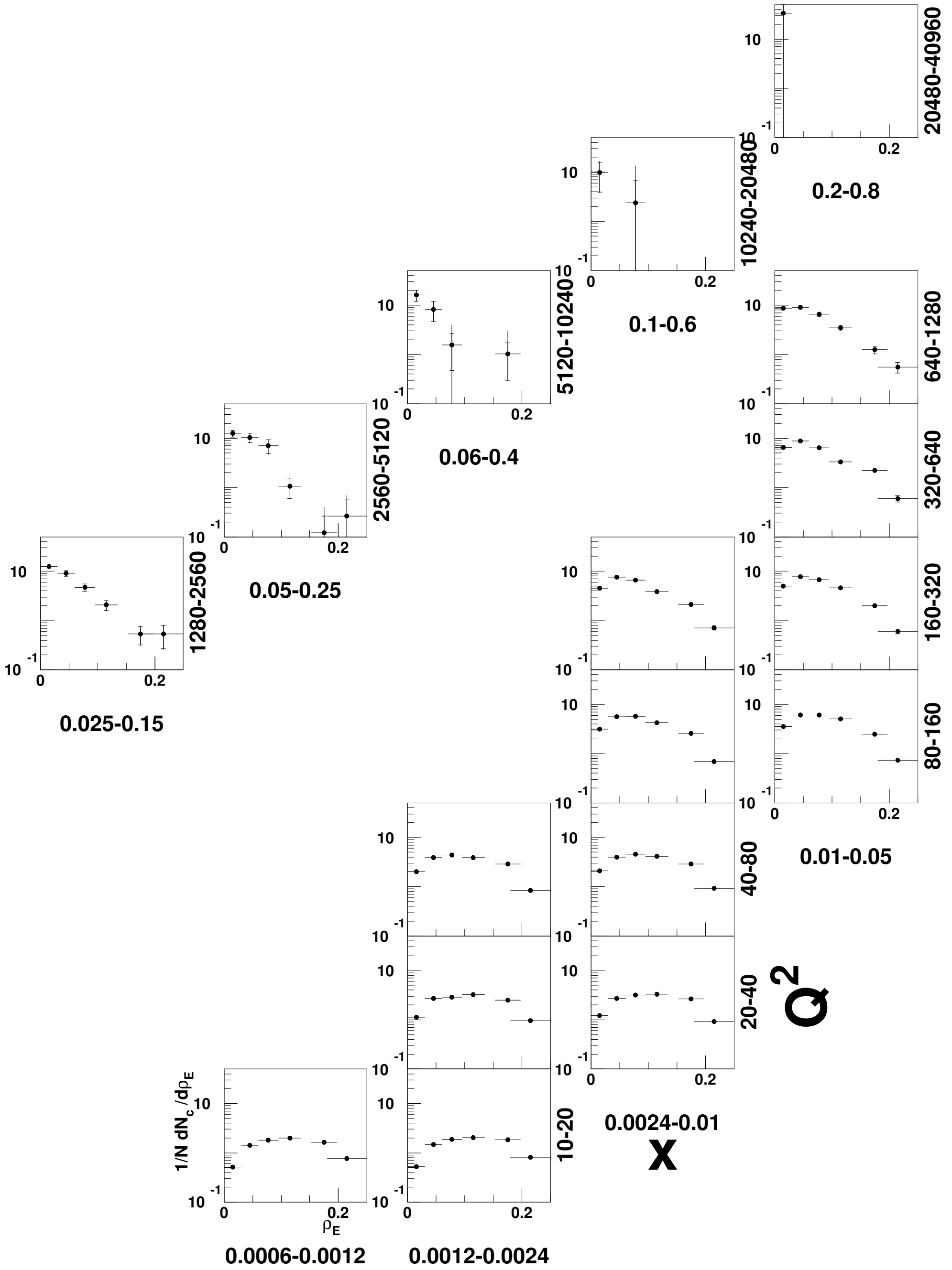

Figure 7.8: Corrected jet mass distribution for 1995 data with systematic errors included. The inner error bars are statistical only with the outer as systematic and statistical combined in quadrature.

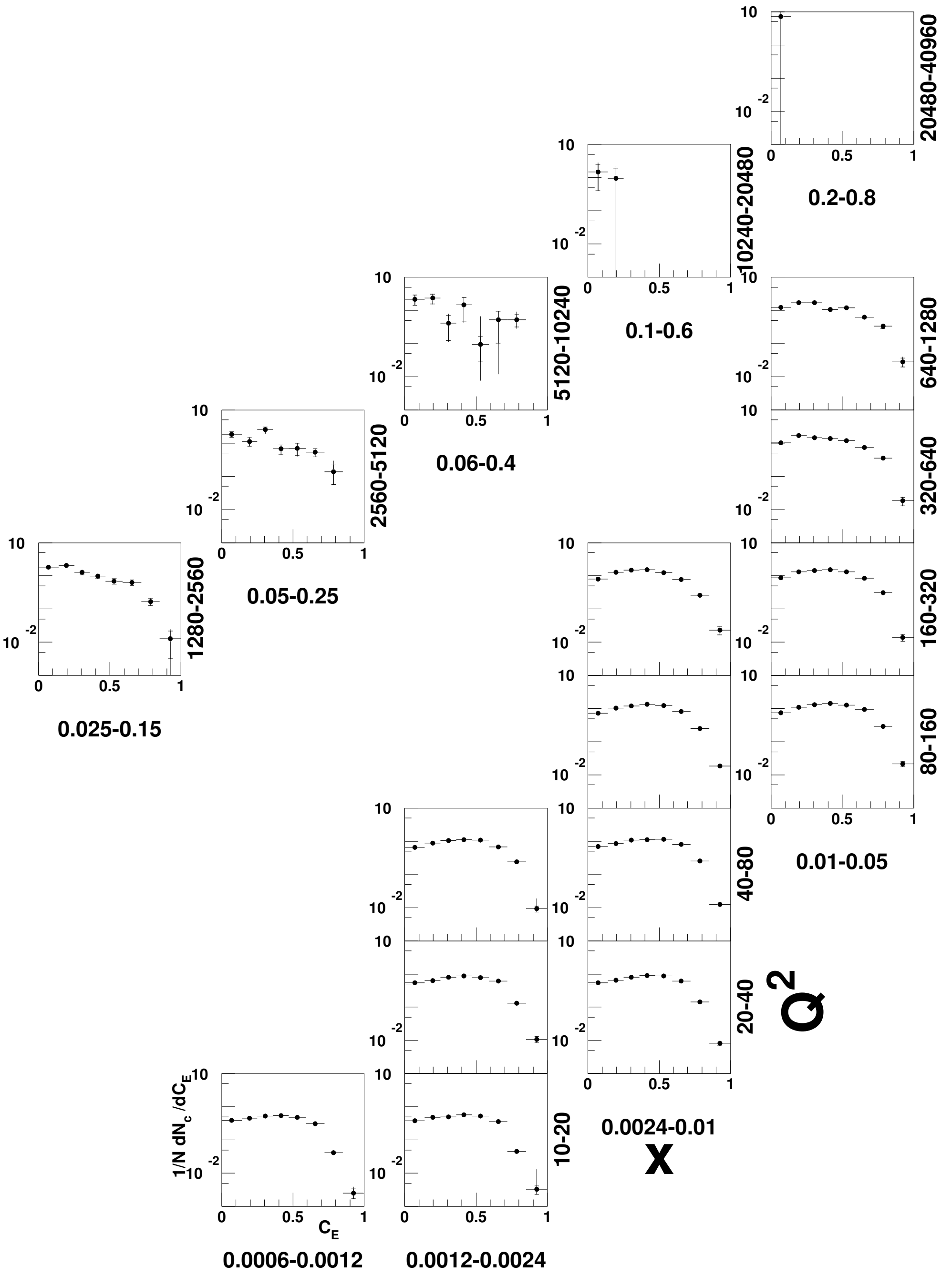

Figure 7.9: Corrected C parameter distribution for 1995 data with systematic errors included. The inner error bars are statistical only with the outer as systematic and statistical combined in quadrature.

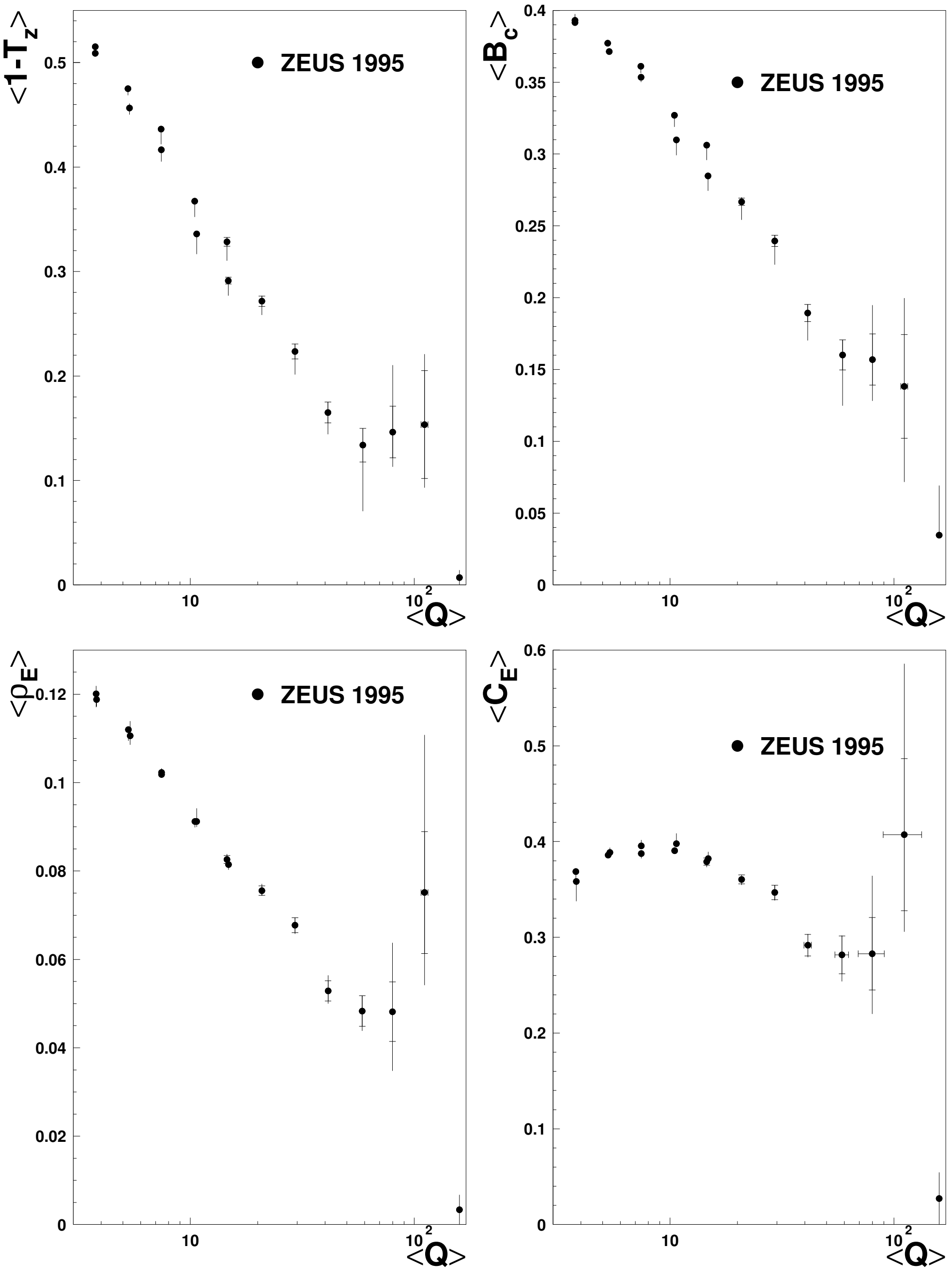

Figure 7.10: Corrected mean thrust distribution for 1995 data with systematic errors included. The inner error bars are statistical only with the outer as systematic and statistical combined in quadrature.

combined in quadrature with the systematic errors. For the mean distribution the dominant systematic error is that of the MC hadronisation model dependence.

7.4 Combined Results

To obtain result with the greatest statistical significance it is desirable to combine the two corrected data samples of 1995 and 1996+97. As has been presented in Section 7.1 the two corrected data samples show good agreement. As the systematic checks for each sample are the same, within statistical errors, the systematic distributions for each of the samples can be combined with the following equation:

$$F = \frac{\frac{F(95)}{\sigma^2_{F(95)}} + \frac{F(96+97)}{\sigma^2_{F(96+97)}}}{\frac{1}{\sigma^2_{F(95)}} + \frac{1}{\sigma^2_{F(96+97)}}} \tag{7.1}$$

Where F can be either a mean or differential distribution point and σ_F the error on that point. The systematic shifts for the combined data can then be evaluated. The combined mean distributions will be the data sets that are used for the power correction fits presented in the next chapter.

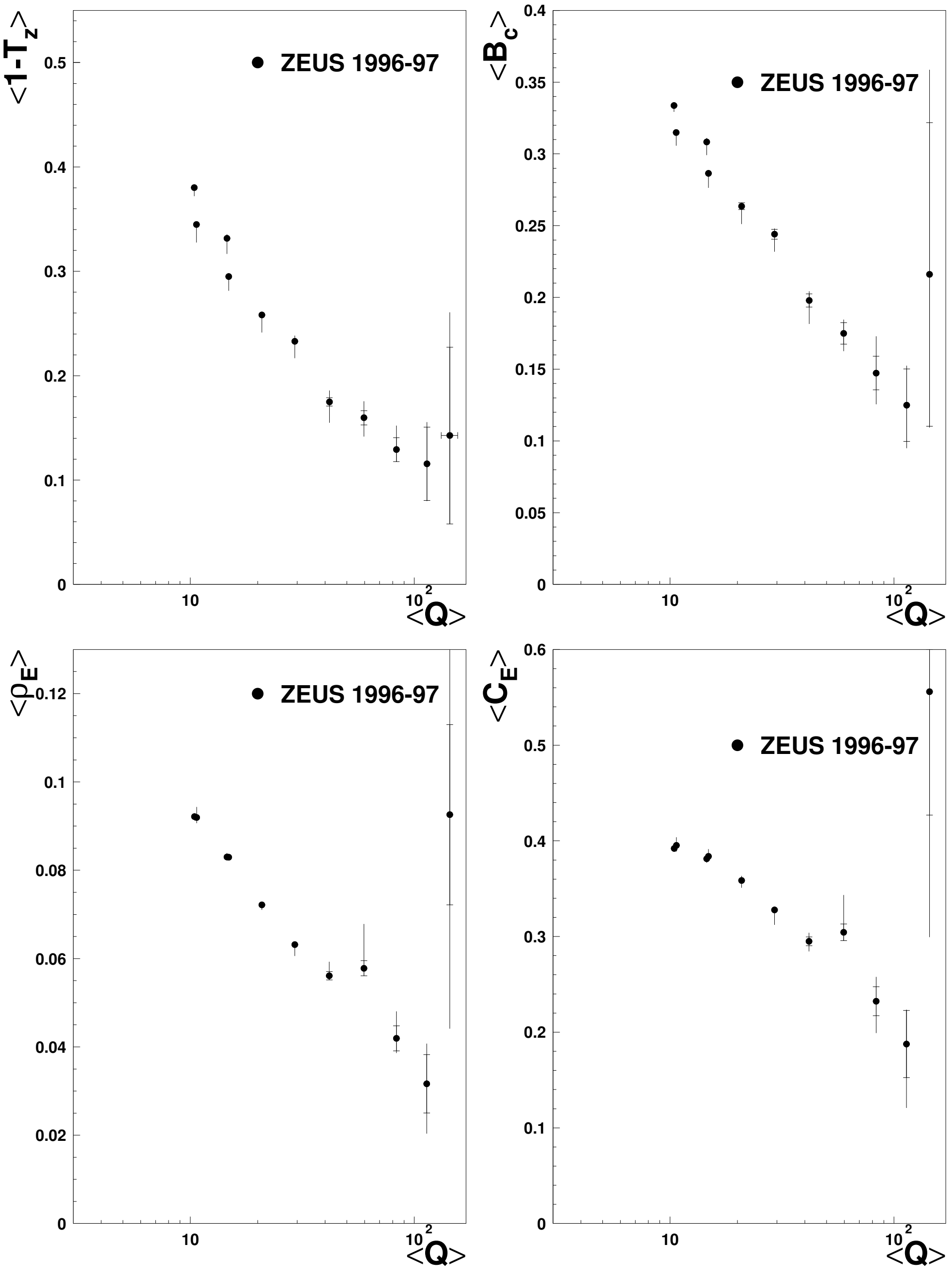

Figure 7.11: Corrected mean thrust distribution for 1996-97 data with systematic errors included. The inner error bars are statistical only with the outer as systematic and statistical combined in quadrature.

Chapter 8

Power Correction fits

Power correction fits to the mean event shape variable distributions for T_z, B_c, ρ_E and C_E for the combined 1995, 1996 and 1997 data samples are presented in this chapter. Systematic variations of the data and the fitting method are evaluated and included in the presentation of results for $\overline{\alpha_0}$ and $\alpha_s(M_Z)$. Results are presented as a function of the minimum $\langle Q \rangle$ of the data included in the fit.

8.1 Power Fit Results

The general form for the mean event shape distribution as a function of mean Q, given in Equation 2.26, is fitted to the data. The fit is accomplished by the variation of two free parameters, specifically $\Lambda^{[4]}_{\overline{\rm MS}}$ and $\overline{\alpha_0}$. The NLO prediction is calculated using the relevant parameterisation presented in Section 6.4 and the value of $\Lambda^{[4]}_{\overline{\rm MS}}$ is converted to the associated value of $\alpha_s(Q)$ for the calculation of the power correction term.

The fits were performed using data with Q^2 >80 GeV^2, the value of μ_I was defined to be 2 GeV and the number of active flavours was fixed at 3. In

Sys.	$\overline{\alpha_0}$ (2 GeV)	$\Lambda^{[4]}_{\overline{\rm MS}}$(GeV)	χ^2/NDF
Central	0.455 ± 0.011	0.425 ± 0.029	154/9
$E - P_z$	0.475(+0.020)	0.359(−0.066)	157/9
$\eta < 2.0$	0.448(−0.007)	0.441(+0.016)	151/9
HERWIG	0.449(−0.006)	0.540(+0.115)	430/9
$P_T > 0.1$	0.462(+0.007)	0.413(−0.012)	186/9
RHL Tracks	0.454(−0.001)	0.447(+0.022)	277/9
$y_e < 0.8$	0.460(+0.005)	0.411(−0.014)	140/9
$y_{JB} > 0.05$	0.491(+0.036)	0.337(−0.088)	253/9
Combined	$0.455 \pm 0.011^{+0.042}_{-0.009}$	$0.425 \pm 0.029^{+0.118}_{-0.112}$	

Table 8.1: Fitted values of $\overline{\alpha_0}$ and $\Lambda^{[4]}_{\overline{\rm MS}}$ for the combined 1995-1997 mean T_z distribution.

Table 8.1 to 8.4 the results for each event shape is shown along with the fitted values for each of the experimental systematic checks. The results for the central analyses are presented with the statistical errors while the systematic results are presented with the systematic shift from the central values given in brackets. The combined results for the statistical and experimental systematic errors are shown for each event shape as the last entry in the table.

If the logarithmic term (see Equation 2.28) for jet broadening is included, $p = 1$, the minimisation does not converge on a value of $\Lambda^{[4]}_{\overline{\rm MS}}$ within the range of validity, which is taken to be 0.1 to 0.9. Thus, the suggested logarithmic term (i.e. $p = 1$) is not supported by the data. This confirms an earlier H1 result and a re-evaluation of the theoretical form is underway. The fit was recalculated for a power correction term with $p = 0$ with the results shown

Sys.	$\overline{\alpha_0}$ (2 GeV)	$\Lambda^{[4]}_{\overline{\mathrm{MS}}}$(GeV)	χ^2/NDF
Central	0.383 ± 0.003	0.211 ± 0.012	222/9
$E - P_z$	0.382(−0.001)	0.209(−0.002)	195/9
$\eta < 2.0$	0.382(−0.001)	0.208(−0.003)	235/9
HERWIG	0.418(+0.035)	0.330(+0.119)	227/9
$P_T > 0.1$	0.383(+0.000)	0.211(+0.000)	186/9
RHL Tracks	0.380(−0.003)	0.199(−0.012)	261/9
$y_e < 0.8$	0.381(−0.002)	0.203(−0.008)	226/9
$y_{JB} > 0.05$	0.387(+0.004)	0.214(+0.003)	253/9
Combined	$0.383 \pm 0.003^{+0.035}_{-0.004}$	$0.211 \pm 0.012^{+0.118}_{-0.015}$	

Table 8.2: Fitted values of $\overline{\alpha_0}$ and $\Lambda^{[4]}_{\overline{\mathrm{MS}}}$ for the combined 1995-1997 mean B_c distribution with no $\log(Q/Q_0)$ term.

Sys.	$\overline{\alpha_0}$ (2 GeV)	$\Lambda^{[4]}_{\overline{\mathrm{MS}}}$(GeV)	χ^2/NDF
Central	0.535 ± 0.001	0.637 ± 0.013	63/9
$E - P_z$	0.534(−0.001)	0.629(−0.008)	44/9
$\eta < 2.0$	0.535(+0.000)	0.630(−0.007)	55/9
HERWIG	0.535(+0.000)	0.626(−0.011)	23/9
$P_T > 0.1$	0.536(+0.001)	0.640(+0.003)	57/9
RHL Tracks	0.539(+0.004)	0.605(−0.032)	38/9
$y_e < 0.8$	0.535(+0.000)	0.635(−0.002)	41/9
$y_{JB} > 0.05$	0.532(−0.003)	0.648(+0.011)	135/9
Combined	$0.535 \pm 0.001^{+0.004}_{-0.003}$	$0.637 \pm 0.013^{+0.011}_{-0.036}$	

Table 8.3: Fitted values of $\overline{\alpha_0}$ and $\Lambda^{[4]}_{\overline{\mathrm{MS}}}$ for the combined 1995-1997 mean ρ_E distribution.

Sys.	$\overline{\alpha_0}$ (2 GeV)	$\Lambda^{[4]}_{\overline{\rm MS}}$(GeV)	χ^2/NDF
Central	0.356 ± 0.001	0.381 ± 0.006	82/9
$E - P_z$	0.356(+0.000)	0.378(−0.003)	68/9
$\eta < 2.0$	0.356(+0.000)	0.378(−0.003)	85/9
HERWIG	0.354(−0.002)	0.380(−0.001)	105/9
$P_T > 0.1$	0.356(+0.000)	0.383(+0.002)	76/9
RHL Tracks	0.359(+0.003)	0.390(+0.009)	61/9
$y_e < 0.8$	0.356(+0.000)	0.381(+0.000)	68/9
$y_{JB} > 0.05$	0.355(−0.001)	0.376(−0.005)	186/9
Combined	$0.356 \pm 0.001^{+0.003}_{-0.002}$	$0.381 \pm 0.006^{+0.009}_{-0.007}$	

Table 8.4: Fitted values of $\overline{\alpha_0}$ and $\Lambda^{[4]}_{\overline{\rm MS}}$ for the combined 1995-1997 mean C_E distribution.

in Table 8.2.

The results for the mean thrust distributions indicate that the dominant systematic for both $\overline{\alpha_0}$ and α_s is the change of MC generator to HERWIG. This is followed closely, but in the opposite direction, by the change in y_{JB}. The fitted value for $\overline{\alpha_0}$(2 GeV)$= 0.455 \pm 0.011^{+0.042}_{-0.009}$(stat $\oplus$ sys) is certainly close to the theoretically predicted value of 0.5.

Converting from $\Lambda^{[4]}_{\overline{\rm MS}}$ to the strong coupling constant one obtains $\alpha_s(M_Z) = 0.124^{+0.001+0.005}_{-0.002-0.007}$(stat $\oplus$ sys) which, within combined statistical and systematic errors, is in agreement with the world average. The major error on the measurement of both values come from the experimental systematic uncertainties.

For the mean jet broadening distributions, without the inclusion of the logarithmic term, the result for both variables are dominated by the HER-

WIG systematic shift. The fitted value for $\overline{\alpha_0}(2\ \text{GeV}) = 0.383 \pm 0.003^{+0.035}_{-0.004}(\text{stat} \oplus \text{sys})$ disagrees with the result from the thrust analysis. The result for the strong coupling constant are $\alpha_s(M_Z) = 0.110^{+0.001+0.008}_{-0.001-0.001}(\text{stat} \oplus \text{sys})$, which is in agreement with the world average but in disagreement around the 2σ level with the result from thrust.

The mean jet mass result for $\overline{\alpha_0}$ is dominated by the systematic error introduced by the non-vertex fitted track systematic. The final result is $\overline{\alpha_0}(2\ \text{GeV}) = 0.535 \pm 0.001^{+0.004}_{-0.003}(\text{stat} \oplus \text{sys})$, which disagrees with the results from thrust and jet broadening but agrees with the theoretical prediction with it's 20% uncertainty. The measurement of the strong coupling constant, $\alpha_s(M_Z) = 0.133^{+0.001+0.001}_{-0.001-0.001}(\text{stat} \oplus \text{sys})$, is dominated by the uncertainties coming from the non-vertex fitted tracks, HERWIG and y_{JB} systematic shifts. The result for the strong coupling constant is in disagreement with both the world average and the results for thrust and jet broadening.

Finally, the C parameter result for $\overline{\alpha_0}$ has smaller systematic shifts than the other event shapes but is still dominated by the non-vertex fitted tracks systematics. The results for $\overline{\alpha_0}(2\ \text{GeV}) = 0.356 \pm 0.001^{+0.003}_{-0.002}(\text{stat} \oplus \text{sys})$ is in disagreement with all the other event shape results. The situation with the strong coupling constant is similar, here too the systematic shifts are smaller than those of the other event shapes. The result of $\alpha_s(M_Z) = 0.121 \pm 0.001^{0.001}_{0.001}(\text{stat} \oplus \text{sys})$ is only in agreement with that for thrust and also the world average.

The χ^2 per degree of freedom for all the fits are quite poor, ranging from 7 for the ρ_E fit up to 25 for the B_c fit. These high values result from the inaccurate reproduction of the x dependence of the NLO mean event shapes. That is to say the only x dependence for the mean event shape distributions comes from the NLO prediction. Thus, if this incorrectly reproduced the x

dependence seen in the data then there is no additional degree of freedom in the power correction contribution to compensate for this. The power correction terms may have some x dependence and future theoretical work in this area may produce some prescription for this to be incorporated.

Figure 8.1 shows the distribution of the fitted values for the strong coupling constant $\alpha_s(M_Z)$ and the universal hadronisation constant $\overline{\alpha_0}(2\ \mathrm{GeV})$ for each of the event shapes. In addition to the ZEUS 1995-97 results, the recent H1 [53] results are shown for comparison along with the world average for the strong coupling constant and the theoretical prediction for $\overline{\alpha_0}$. The results show a disagreement with not only the world average but also each other. One would hope that the same data sample would produce values within reasonable agreement for the same theoretical fits. However, the theoretical work involved with these power correction terms are pushing the limits of the understanding of QCD.

To assess the importance of experimental systematic errors a more appropriate fitting procedure should include the statistical and systematic errors rather than just the statistical errors as before. If one adds the statistical and systematic errors in quadrature and uses these asymmetric errors in the fitting procedure it will give a more reasonable χ^2 fit and one can check if the central values of the fits are being significantly pulled.

Table 8.5 shows the results for the fitted values of $\overline{\alpha_0}$, $\Lambda^{[4]}_{\overline{\mathrm{MS}}}$ and subsequently $\alpha_s(M_Z)$. The results for thrust and jet broadening are quite different to those obtained from the first fit which demonstrated the importance of the experimental systematic errors for these variables. However, for ρ_E and C_E the results for jet mass and the C parameter are quite similar. For all the event shapes a lower χ^2 per degree of freedom is found, ranging from just above half to just under three. For all the event shape fits the correlations

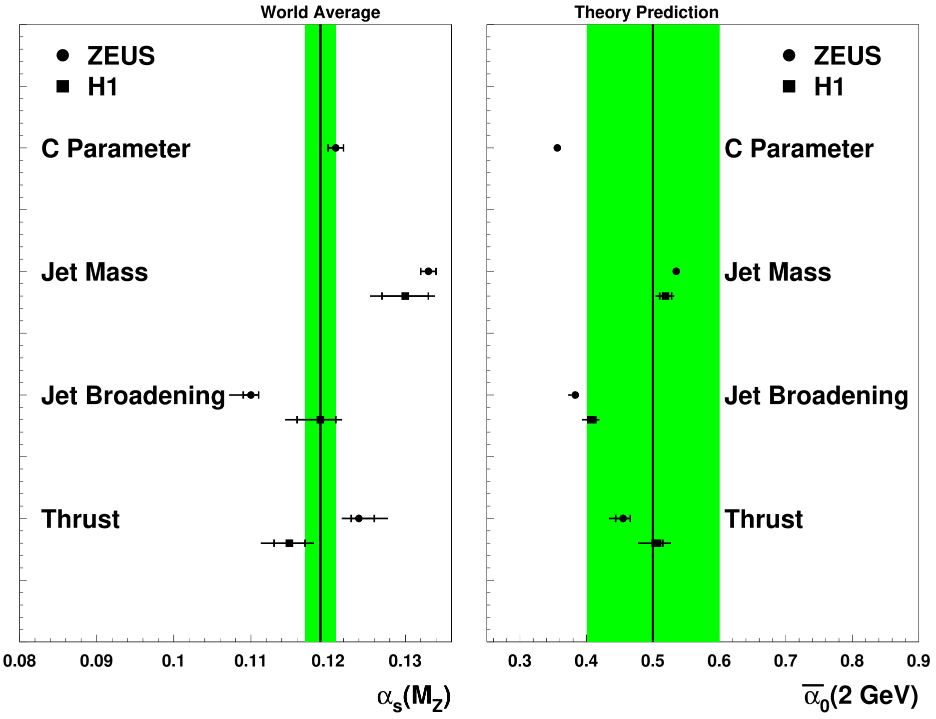

Figure 8.1: Fitted values of $\alpha_s(M_Z)$ and $\overline{\alpha_0}(2\text{ GeV})$ for each of the event shapes shown with the H1 results and the world average and theoretical prediction.

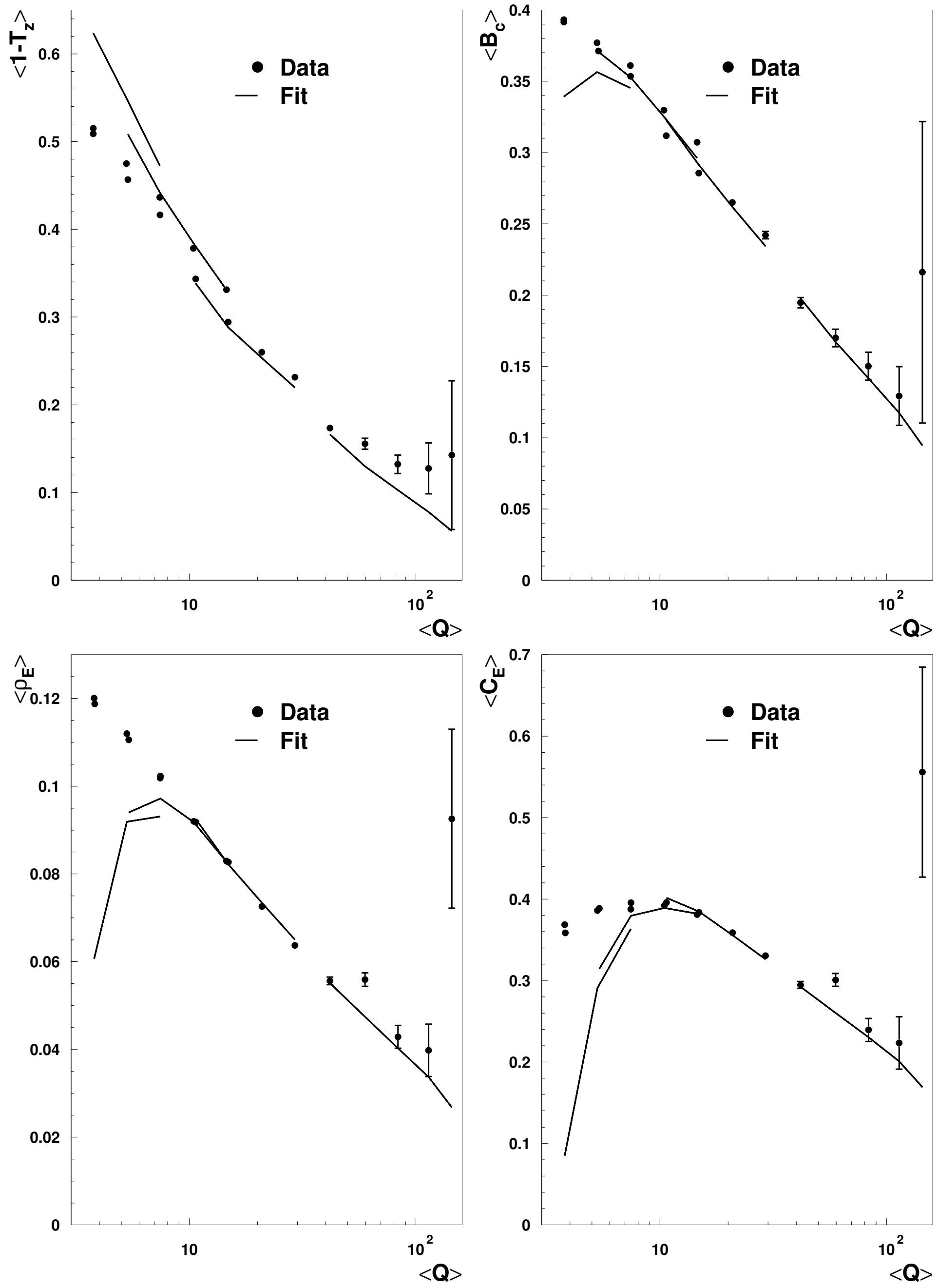

Figure 8.2: Mean event shape distributions (points) with the power corrected NLO prediction (lines) using the fitted values of $\Lambda^{[4]}_{\overline{\mathrm{MS}}}$ and $\overline{\alpha_0}$ shown in Tables 8.1 to 8.4.

Event Shape	$\overline{\alpha_0}$ (2 GeV)	$\Lambda^{[4]}_{\overline{\rm MS}}$	$\alpha_s(M_Z)$	χ^2/NDF
T_Z	0.407 ± 0.027	0.628 ± 0.083	$0.133^{+0.003}_{-0.004}$	10/9
B_c	0.416 ± 0.009	0.324 ± 0.071	$0.118^{+0.004}_{-0.005}$	9/9
ρ_E	0.536 ± 0.001	0.628 ± 0.035	$0.133^{+0.001}_{-0.001}$	5/9
C_E	0.358 ± 0.002	0.398 ± 0.015	$0.122^{+0.001}_{-0.001}$	25/9

Table 8.5: Fitted values of $\overline{\alpha_0}$ and $\Lambda^{[4]}_{\overline{\rm MS}}$ for the combined 1995-97 mean event shapes using the statistical and systematic errors combined in quadrature.

between $\Lambda^{[4]}_{\overline{\rm MS}}$ and $\overline{\alpha_0}$ for the central fits are very large, of the order 0.98.

The inclusion of the fit uncertainties associated with the NLO contribution (see Section 6.4) has not been treated fully. A naïve inclusion of these errors show an additional uncertainty of 1-2% and 8-10% for the fitted values of $\overline{\alpha_0}$ and $\Lambda^{[4]}_{\overline{\rm MS}}$ respectively.

For a comprehensive study of the power correction fits, variation of the renormalisation scale need to be investigated. This investigation also needs to be performed for the NLO MC predictions and an additional parameterisation of the mean event shape results as a function of the renormalisation scale μ obtained. The factorisation scheme dependence for the NLO MC also needs to be investigated. Re-running the NLO MC code is prohibitively time consuming, however, work involving extension to the code which allow the event shapes to be calculated for various renormalisation scales concurrently is underway.

Chapter 9

Conclusion And Further Work

Event shape distributions for thrust, jet broadening, jet mass and the C parameter have been measured using vertex originating charged tracks over a large kinematic range. Differential and mean distributions have been presented for the range $0.0006 \leq x \leq 0.8$ and $10 \leq Q^2 \leq 40960$ GeV^2. The experimental precision of this data, for both mean and differential distributions, is very small (i.e. less than 1-5 %).

The effect of a selection criteria based on the total energy in the current region of the Breit frame has been presented and an energy cut of 3% is shown to be appropriate for a charged track based analysis. The effect of this total energy cut on the NLO prediction has also been presented, it has been shown that a cut of 3% is sufficient when using the NLO prediction in conjunction with power corrections which is then fitted to data which uses charged tracks and a 3% energy cut.

The mean event shape distributions for the combined 1995-97 data, a total luminosity of 43.92 pb^{-1}, have been used to fit theoretical predictions of the distributions as a function of $\Lambda^{[4]}_{\mathrm{QCD}}$ and $\overline{\alpha_0}$. These predictions are based on the premise of an effective strong coupling constant which is active below a certain scale. The first moment of this effective coupling is one of the fitted variables, $\overline{\alpha_0}$, and should be a universal parameter of both shape variable and process.

The results for these mean event shape fits have been promising. The idea of the parameter $\overline{\alpha_0}$ being universal for all event shapes is supported by the fitted results, considering the 20% theoretical error cited by the authors of this work. Additional problems have been encountered with the jet broadening shape variable where the inclusion of the logarithmic term is not supported by the data. The fitted values of $\alpha_s(M_Z)$ show some agreement, specifically thrust and the C parameter, with the world average. The individual results are not self consistent but residual theoretical uncertainties arising from renormalisation and factorisation scale dependence are still to be evaluated.

Further work based on the power correction fits include determination of uncertainties due to both the renormalisation scale and factorisation scheme dependence. Work involving the tuning of the event shapes x dependence is also desirable and may be achieved by the inclusion of a PDF based on the ZEUS 1995-97 data. Further work on the theoretical side, most notably the inclusion of an x dependence and the calculation of further loop corrections, are desirable.

The differential distributions have also been presented with reasonable errors over a large range in Q^2. There remains the possibility of fitting resummed differential event shape distributions to this data over a restricted range of the event shape to obtain a result for α_s. The fit would be confined to a region far from the collinear divergences. This remains an untapped area of interest.

The experimental side of the measurement could be extended to include information from the ZEUS calorimeter. This would not only include neutral particles in the measurement but also increase the measurable range in η. The reducing resolution on high momentum tracks will also be compensated by the increasing energy resolution of the calorimeter. An analysis using information from both the tracking detectors and the calorimeter would therefore produce interesting results.

The event shapes presented in this thesis represent a reasonably orthogonal set for investigation. Measurement of other variables, such as total energy in the current region, are possible but still require the theoretical calculation of the power correction terms. Further work on the problems concerning jet broadening are also needed.

Bibliography

[1] HERA, *A Proposal for a Large Electron-Proton Colliding Beam Facility at DESY*, DESY HERA 81-10.

[2] ZEUS Collab.s; J.Breitweg *et al.*, *The ZEUS Detector, Status Report 1993*, DESY (1993).

[3] H1 Collab., I.Abt *et al.*, Nucl. Instr. and Methods A386 (1997) 310.

[4] H1 Collab., I.Abt *et al.*, Nucl. Instr. and Methods A386 (1997) 348.

[5] HERMES Collab., K.Coulter *et al.*, DESY-PRC 90/01 (1990).

[6] HERMES Collab., K.Coulter *et al.*, DESY-PRC 93/06 (1993).

[7] HERA-B Collab., H.Albrecht *et al.*, *An Experiment to Study CP Violation in the B System Using an Internal Target at the HERA Proton Ring*, Letter of Intent, DESY-PRC 92/04 (1992).

[8] ZEUS Collab.; J.Breitweg *et al.*, *A Microvertex Detector For ZEUS*, DESY-PRC 97/01 (1997).

[9] J.Milewski, C.Youngman and A.Kotanski, *The ZEUS Message Passing System*, Submitted to the 1994 CHEP Conference.

[10] J.K.Ousterhout, *Tcl and the Tk Toolkit*, Addison-Wesley, Massachusetts. (1994).

[11] B.W.Kernighan & D.M.Ritchie, *The C Programming Language*, Prentice Hall,New Jersey. (1988).

[12] A.Flavell, S.Topp-Jorgensen & R.Waugh, *CTD RC: The run control task for the central tracking detector of the ZEUS detector*, ZEUS 97-024.

[13] D.Kisielewaska *et al.*, *Fast Luminosity Monitoring at HERA*, DESY - HERA Report 85-25.

[14] H.Bethe and W.Heitler, Proc. Roy. Soc., **A146** (1934) 83.

[15] G.F.Hartner *et al.*, *VCTRAK (3.06/20) : Offline Output Information*, ZEUS Note 96-013.

[16] R.Sinkus, *A novel approach to error function minimisation for feed-forward neural networks*, Nucl. Inst. Methods **A 361** 290, (1995).

[17] TASSO Collab., *Evidence for planaer events in* e^+e^- *annihilation at high energies*, Phys. Lett. **B 86** (1979) 243.

[18] ZEUS Collab., J.Breitweg *et al.*, DESY Report 98-121, Submitted to The European Physical Journal, (1998).

[19] K.Fabricius, G.Kramer, G.Schierholz and I.Schmitt, Z. Phys. C11 (1981) 315.

[20] G.Kramer and B.Lampe, Fortschr. Phys. 37 (1989) 161.

[21] S.Catani and M.H.Seymour, *The Dipole Formalism for the Calculation of QCD Jet Cross Sections at Next-to-Leading Order*, CERN-TH/96-28, hep-ph/9602277, (1996).

[22] S.Catani and M.H.Seymour, *A General Algorithm for Calculating Jet Cross Sections in NLO QCD*, CERN-TH/96-29, hep-ph/9605323, (1996).

[23] S.Catani and M.H.Seymour, *NLO Calculations in QCD : A General Algorithm*, CERN-TH/96-181, hep-ph/96007318, (1996).

[24] S.Catani and M.H.Seymour, *QCD Jet Calculations in DIS Based on the Subtraction Method and Dipole Formalism*, CERN-TH/96-239, hep-ph/9609237, (1996).

[25] S.Catani and M.H.Seymour, *NLO QCD calculations in DIS at HERA Based on the Dipole Formalism*, CERN-TH/96-240, hep-ph/9609521, (1996).

[26] S.Catani and M.H.Seymour, *Jet Cross Sections at Next-to-Leading Order*, CERN-TH/96-342, hep-ph/9612236, (1996).

[27] M.H.Seymour, *DISENT Program Manual*, Version 1.0.1, (1997).

[28] H. Plothow-Besch, *PDFLIB User Manual (Version 7.09)*, W5051 PDFLIB.

[29] J.C.Collins, *Renormalisation*, Cambridge University Press, (1984).

[30] Particle Data Group, *Review of Particle Physics*, Volume 3, Number 1-4, The European Physical Journal, (1998).

[31] ZEUS Collab., *Measurement of* α_s *from Jet Rates in Deep Inelastic Scattering*, *Phys. Lett.* **B** 363 (1995) 201.

[32] P.A. Movilla Fernández, O.Biebel, S.Bethke, S.Kluth, P.Pfeifenschneider and the JADE Collab., *A Study of Event Shapes and Determination of*

α_s *using data of* e^+e^- *Annihilation at* $\sqrt{s} = 22$ *and* 44 *GeV*, PITHA 97/27, (1997).

[33] DELPHI Collab., *Measurement of Event Shape and Inclusive Distributions at* $\sqrt{s} = 130$ *and* 136 *GeV*, CERN-PPE/96-130, (1996).

[34] M.Dasgupta and B.R.Webber, *Power Corrections to Event Shapes in Deep Inelastic Scattering*, hep-ph/9704297, (1997).

[35] B.R.Webber, *Proceedings of the XXVII International Symposium on Multi-particle Dynamics*, Frascati, hep-ph/9712236, (1997).

[36] Yu.L.Dokshitzer, A.Lucenti, G.Marchesini and G.P.Salam, *Universality of* $1/Q$ *corrections to jet-shape observables rescued*, *Nucl. Phys.* **B 511** (1998) 396.

[37] ZEUS Collab., *Observation of scaling violations in scaled momentum distributions at HERA*, Phys. Lett. **B 414**, (1997) 428.

[38] L. Lönnblad, *Ariadne Version 4.08 program and manual*, *Comp. Phys. Comm.*, **71** (1992) 15.

[39] G.Ingelman, A.De Roeck & R.Klanner, *Future Physics at HERA Workshop Proceedings*, Volume 1, (1996).

[40] G.Ingelman, LEPTO version 6.1, in *Physics at HERA*, edited by W.Buchmüller, G.Ingelman, Volume 3, DESY (1991) 1366.

[41] H-U. Bengtsson and T.Sjöstrand, *Comp. Phys. Comm.* **46** (1987) 43.

[42] T.Sjöstrand, *Comp. Phys. Comm.* **82** (1994) 74.

[43] T.Sjöstrand, *PYTHIA 5.7 and JETSET 7.4 physics and manual*, CERN-TH.7112/93, Dec. 1993, (revised Aug. 1994).

[44] T.Sjöstrand, *Comp. Phys. Comm.* **39** (1986) 347.

[45] R.Brun *et al.*, *GEANT 3*, CERN DD/EE/84-1 (1987).

[46] K.Hamacher and M.Weierstall, *The Next Round of Hadronic Generator Tuning Heavily Based on Identified Particle Data*, CERN PrePrint hep-ex/9511011, (1995).

[47] G.Marchesini, B.R.Webber, G.Abbiendi, I.G Knowles, M.H Seymour and L.Stanco, *HERWIG Version 5.1*, *Comp. Phys. Comm.*, **67** (1992) 465.

[48] H1 Collab., I.Abt *et al.*, *Z. Phys.* C63 (1994) 377.

[49] ZEUS Collab., M.Derrick *et al.*, *Z. Phys.* C67 (1995) 93.

[50] H1 Collab. S.Aid *et al.*, *Phys. Lett.* B356 (1995) 118.

[51] ZEUS Collab., M.Derrick *et al.*, *Z. Phys.* C70 (1996) 1.

[52] CTEQ Collab., MSUHEP-60426, CTEQ-604.

[53] H1 Collab., *Measurement of event shape variables in deep inelastic scattering ep scattering*, DESY 97-098, (1997).